Metastable Solid and Liquid Helium-4

Jules Grucker

Laboratoire Kastler Brossel
Physique quantique et applications

SORBONNE UNIVERSITÉ

Habilitation à Diriger les Recherches

SORBONNE UNIVERSITÉ

Laboratoire Kastler Brossel

École doctorale : "Physique en Île-de-France"

Metastable Solid and Liquid Helium-4

by

Jules Grucker

defended on November 30, 2018

Committee :

M^{me}.	Martine BEN AMAR	
M.	Pierre-Jean NACHER	
M.	Etienne ROLLEY	Referee
M.	Ladislav SKRBEK	Referee
M.	Pierre-Etienne WOLF	Referee

Contents

Introduction

This manuscript presents the experiments done in the group "Quantum solids and fluids" of Laboratoire Kastler Brossel in Paris since I joined the group in 2009. This group was created in 2003 by Philippe Jacquier and Jacques Dupont-Roc joined him in 2004[1].

We are interested in the metastable phases of condensed ^{4}He.

The fascinating phase diagram of ^{4}He at low temperatures is shown in the figure below. Several features in this diagram are unique compared to that of all other simple elements. The most striking one is that there is no triple point (liquid-gas-solid coexistence point) in the phase diagram of ^{4}He meaning that it is possible to cool a liquid-gas mixture of ^{4}He all the way down to $T \to 0$ K. Below $T_\lambda = 2.17$ K, liquid ^{4}He is in its famous superfluid state which is understood as a mixture of two fluids: a superfluid part with zero entropy and viscosity and a normal fluid which carries the heat content.

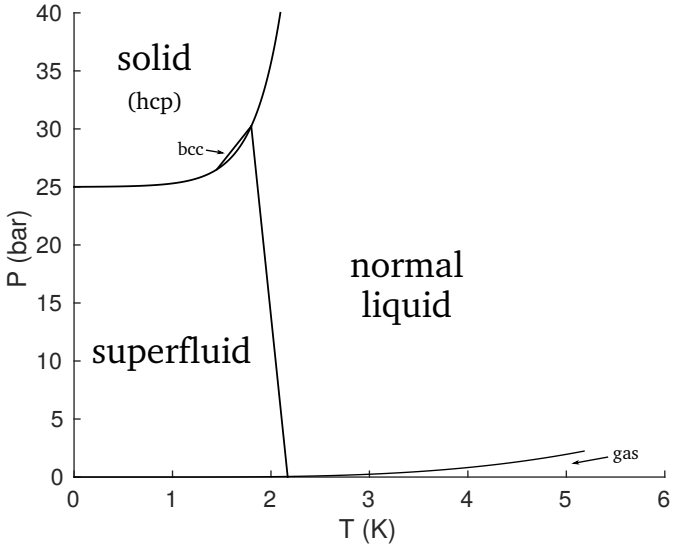

Pressure temperature phase diagram of ^{4}He at low temperatures

Our group performs acoustic experiments which enable us to bring solid ^{4}He

[1] Jacques Dupont-Roc is retired since 2011

in the superfluid domain of the phase diagram realizing metastable solid ^{4}He and to bring liquid ^{4}He in the negative pressure domain of the phase diagram realizing metastable liquid ^{4}He. The possibility of having metastable liquids or solids is due to the fact that the solid/liquid and liquid/gas transitions are first order phase transitions. The density of the two phases involved in the transition is discontinuous at the transition. The interface between the lower and higher density phases has a given energy per unit area (the surface tension in the case of a liquid/gas mixture). Consequently, there is an energy cost associated with the creation of a nucleus of one of the phase in the other. This energy barrier makes metastable states possible. Usually, the nucleation of nucleii of the stable phase within the metastable one occurs on "defects" such as impurities or walls of the container. In this case the nucleation is said to be heterogeneous. When on the contrary, the nucleation is not triggered by defects, it is said to be homogeneous.

The case of liquid ^{4}He is of special interest for the study of homogeneous cavitation (the creation of vapor bubbles within a metastable liquid) because liquid ^{4}He is an extremely pure liquid. Indeed, at liquid helium temperatures, almost every impurity is frozen and sticks to the walls or falls at the bottom of the container. The only impurities in liquid ^{4}He are helium-3 atoms and their density is very low, typically 0.1 ppm.

The first part of the first chapter of the manuscript deals with experiments aiming at measuring the density at which liquid helium ^{4}He homogeneously cavitates at around 1 K. As I shall shortly expose, similar experiments were done in the 90's but have measured the cavitation *pressure* (not density) of liquid ^{4}He. When compared to those earlier measurements, our density measurement raises interesting questions about the equation of state of metastable liquid ^{4}He. The second part of Chapter 1 will be dedicated to experiments measuring the lifetimes of cavitation bubbles in liquid ^{4}He. We discovered a dramatic transition of the lifetime depending whether the liquid is superfluid or not.

Our experimental set-up was in fact initially built to produce and study metastable solid ^{4}He. The main reason that our group started this experiment is that metastable solid ^{4}He is a candidate for a potential and yet not discovered very exciting new state of matter called a "supersolid". Chapter 2 is devoted to the description of these experiments and presents our success in realizing metastable hcp solid ^{4}He using analogous acoustic techniques as in the liquid case. An additional difficulty arises in the case of the hcp solid ^{4}He due to the anisotropy of sound wave velocities. I will also discuss the observation of an unexpected destabilization of the metastable solid.

The last chapter of the manuscript deals with the near future of the experiment. To try to better understand the observed destabilization of both liquid and solid metastable ^{4}He, the Equation of State of the metastable states must

be measured experimentally. My research project is to set up an experiment of Stimulated Brillouin Scattering which will enable us to locally measure the speed of sound in the metastable states and hence deduce these Equations of State.

Chapter I

Metastable Liquid Helium-4

In this chapter, I shall discuss the experiments done in our group during the PhD of Qu An[1] between 2013-2017 where we studied the acoustically induced homogeneous cavitation of liquid ^{4}He.

I.1 Overview

I.1.1 Principle of the experiment

In the early 90's, Nissen *et al.* from Portland State University have been the first to use a clever acoustic technique to realize metastable states of liquid ^{4}He[2].

The principle of the method is summarized in figure I.1. A hemispherical piezo electric transducer creates a focused pressure/density wave within the liquid. The crucial idea of this configuration is that it can realize important pressure/density swings far from any interface (walls of the container and of the

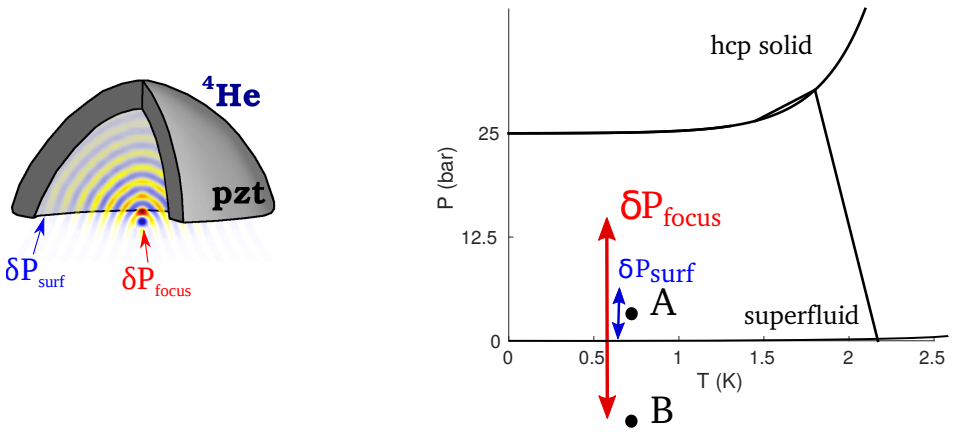

Fig.I.1: Principle of the acoustic method to realize metastable state of liquid ^{4}He. A focused acoustic wave brings the liquid surrounding the acoustic focus into the negative pressure domain of the phase diagram. Heterogeneous nucleation of vapor bubbles is avoided because the sound amplitude is small near the inner surface of the piezo electric transducer (PZT)

transducer) and in a small volume (the acoustic focus) of the bulk of the liquid. These two points strongly reduce the chance of generating heterogeneous nucleation events and hence make possible a deep exploration of the metastable state up to a point where homogeneous cavitation (nucleation of vapor bubbles) is observed. The initial pressure of the liquid (point A of the figure) is chosen a little above the liquid/gas coexistence pressure. This ensures that the low acoustic wave amplitude near the inner surface of the transducer will not trigger any heterogeneous nucleation of vapor bubbles which may strongly disturb the wave propagation. During propagation, the amplitude of the focused wave increases until it eventually reaches a large value at the acoustic focus, large enough to locally put the liquid in a metastable state, where the pressure is negative (point B of the figure).

We have used the same technique to produce metastable states of liquid ^{4}He.

A scheme of our optical cryostat is shown on figure I.2a. This cryostat was built by Ph. Jacquier, J. Dupont and M. Melich during the PhD of M. Melich (2004-2008) much before I joined the team. It is based on a suspended evaporator which can contain 250 cm^3 of liquid ^{4}He and pumped by a high flux Roots pump. There is no liquid nitrogen reservoir to avoid vibrations generated by its boiling. In order to reduce heat transfer, the evaporator is surrounded by four protection layers including two radiation insulation layers filled with many aluminized mylar sheets and two vacuum enclosures. The experimental cell (figure I.2b but not sketched in figure I.2a) is connected at the bottom of the evaporator and can be cooled down to 0.9 K and its temperature regulated between 0.9 K and 4.2 K.

A liquid helium bath of 29 liters is feeding the evaporator through a 0.2 mm capillary tube. The overall autonomy of this cryostat is about 60 hours. There are four circular optical ports on each layer. Their size and position permit us to observe the experimental cell in two orthogonal directions with a large open angle of 25°.

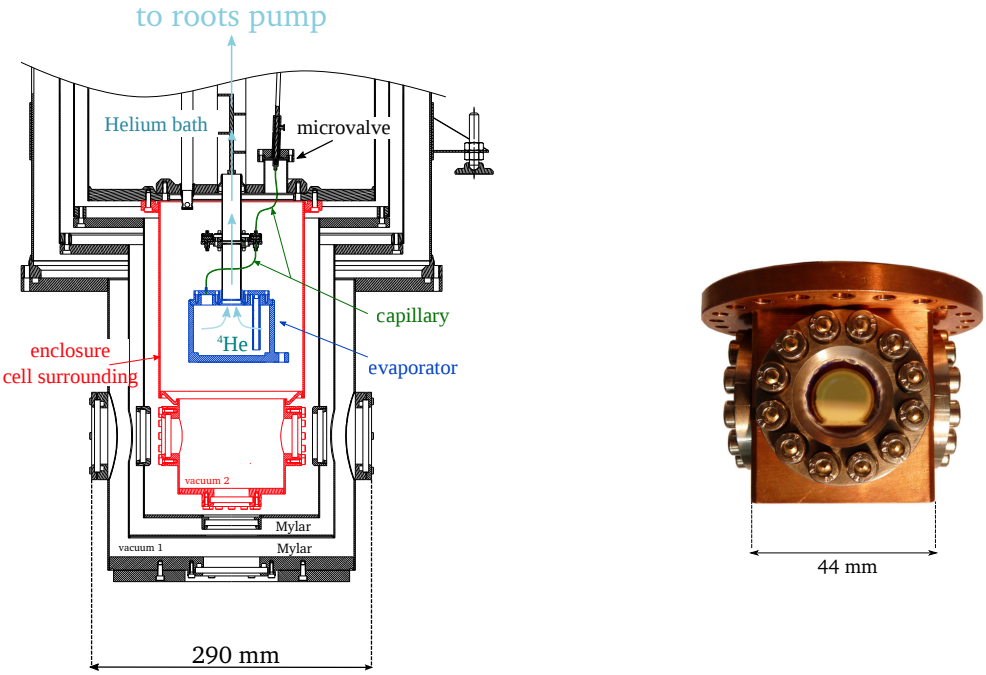

(a) (b)

Fig.I.2: a) Scheme of our optical cryostat. The suspended evaporator can be cooled down to 0.9 K and its temperature regulated between 0.9 K and 4.2 K. There are two vacuum enclosures (vacuum 1 and vacuum 2) and two layers of fold aluminized mylar. b) Picture of the experimental cell which is connected to the bottom of the evaporator.

Figure I.3a is a picture of the hemispherical acoustic piezo electric transducer (PZT) we use to produce focused acoustic wave within liquid ^{4}He. This kind of transducers can be directly bought from piezo electric manufacturers. The inner diameter of our PZT is $d_{in} = 12$ mm and its thickness is 2 mm. The resonant frequency of the first thickness vibration mode is about 1.15 MHz. It is poled and silver-coated on inner and outer surfaces. Figure I.3b is a picture of the PZT in the cell experimental cell partially filled with liquid helium.

I.1.2 Motivations

As mentioned in the introduction, the study of metastable liquid helium ^{4}He is of special interest because of the extreme purity of this quantum liquid.

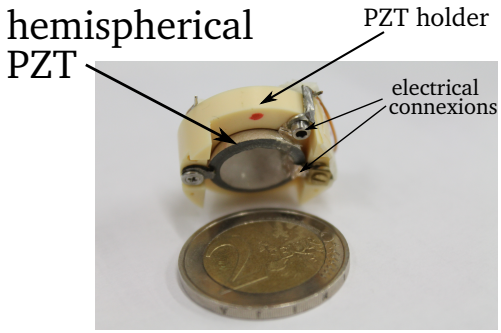

(a)

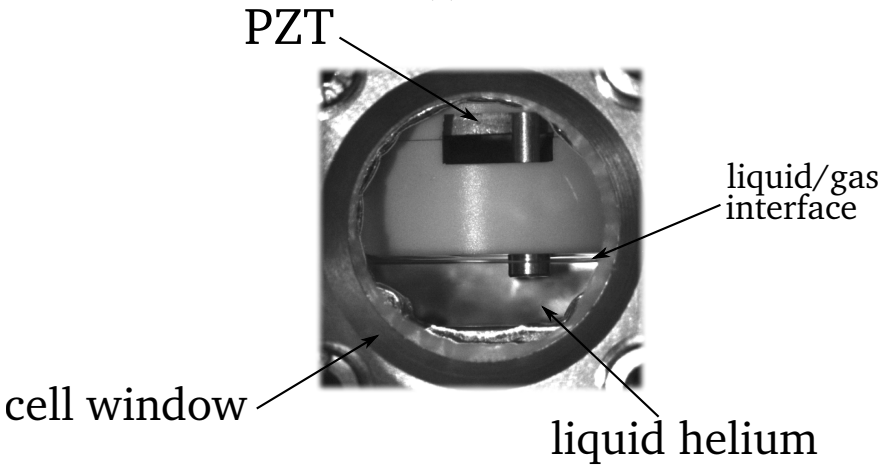

(b)

Fig.I.3: a) Picture of the piezo electric transducer used to produce focused acoustic wave in liquid ^{4}He. b) The PZT in the cell experimental partially filled with liquid helium.

It is then an almost ideal liquid to study homogeneous cavitation and test homogeneous nucleation theory. That is why Nissen *et al.* developed this focused acoustic method for liquid ^{4}He. The quantity Nissen *et al.* were measuring was the pressure at which cavitation occurs inside the liquid (which they call the tensile strength). They had a relative indirect method to estimate this pressure based on the estimation of the acoustically induced pressure at acoustic focus knowing the geometry and the acoustic power of the emitter. They also used the diffraction of a laser beam passing through the acoustic focus to estimate the local pressure and hence the cavitation pressure. Slightly after Nissen proposed the focused acoustic method, H. Maris at Brown University and then F. Caupin and S. Balibar at Laboratoire de Physique Statistique of École Normale Supérieure have also used the technique mostly because they were interested in showing how standard nucleation theory should fail at low enough temperature due to quantum effects (a good review of theoretical and experimental works on cavitation in liquid helium is found in [3]). These groups also estimate in their

experiments the pressure at which cavitation occurs using a different method than *Nissen et al.*

As I shall expose in the forthcoming section I.2, we have designed an apparatus capable of measuring the local density variations of liquid helium induced by the acoustic wave. This enables us to measure the density (and not the pressure) at which cavitation occurs. Provided an equation of state of metastable liquid helium-4, our density measurement can be compared to previous cavitation pressure measurements.

I.2 Local density measurements resolved in time

During the PhD of F. Souris [4], the team has developed a time resolved interferometric imaging technique to measure the local optical phase shift induced by the acoustic wave inside liquid/solid helium. For a sample state rotationally invariant around an axis, one can extract a density map from such a phase shift map. The principle of this measurement is shown on figure I.4.

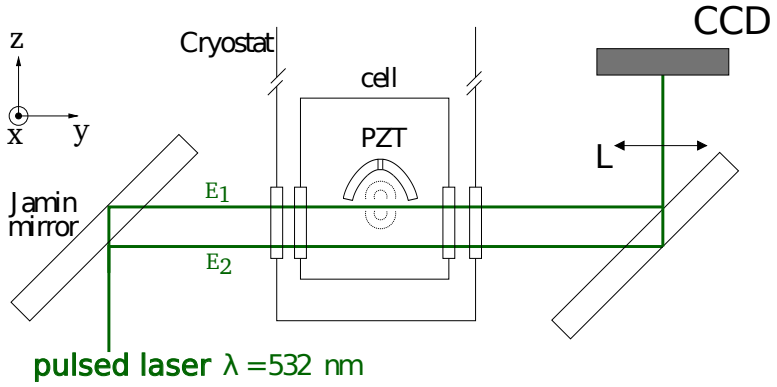

Fig.I.4: A Jamin interferometer is used to measure the optical phase shift induced by the acoustic wave on the optical beam E_1. The optical beam E_2 is not affected by the acoustic wave. The time width of the pulsed laser is 8 ns which is significantly smaller than the ~ 1 μs period of the sound wave. Consequently an "instantaneous" image of the acoustic field is taken by the CCD camera.

The sound pulse to monitor has a period of typically 1 μs (1 MHz excitation). A pulsed laser beam of pulse width 8 ns is used to image this sound pulse. As 8 ns $\ll$ 1 μs, the images recorded by the CCD camera are to be considered as "snapshots" of the acoustic field.

The laser beam is separated into two secondary beams E_1 and E_2 by a thick glass plate. The back surface of this Jamin mirror is an almost perfectly reflecting mirror producing E_1. The beam E_2 originates from the vitreous reflection on the other uncoated surface. The two beams E_1 and E_2 are recombined on an

identical Jamin mirror. The beam E_1 goes through the acoustically perturbed region whereas E_2 goes through an unperturbed region. Hence E_1 experiences a phase shit $\delta\phi$ due to the local variations of the refractive index imposed by the local density modulation by the sound wave. A lens (L on figure I.4) makes the image of the acoustical focal plane onto a CCD camera. The measurement of the light intensity after interference on the CCD camera enables us to measure $\delta\phi$ for each pixel of the camera. In that way we obtain phase maps $\delta\phi(x, z)$ (see axis definition on figure I.4). The spatial resolution is about 20 μm. The detailed method of our phase maps measurements using multiphase interferometric acquisitions can be found in [5]. This article is attached to the manuscript in the appendix "Joined articles" III.3.2.

We assume the phase $\delta\phi$ to be related to the refraction index by a simple integration along the y-axis parallel to the beam direction in the sample (see figure I.5).

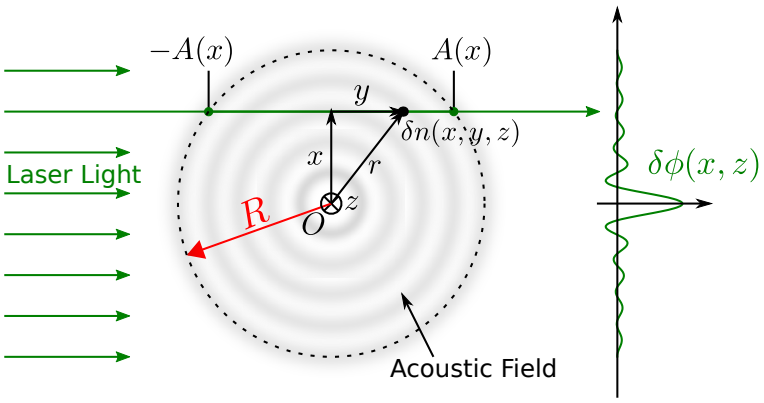

Fig.I.5: Measured phase $\delta\phi$ results from the integration of the optical phase shift over the beam path in the cell. The dashed circle with radius R is the limit of the sound field.

More precisely, for each pixel (x, z), one takes into account the difference $\delta n(x, z, y)$ between the perturbed refractive index $n(x, z, y)$ seen by the signal beam E_1 at point (x, y, z) and the unperturbed refractive index n_0 seen by the reference beam E_2. In our case the sound field is rotationally invariant around the hemisphere axis z so that δn is a function of z and $r = \sqrt{x^2 + y^2}$ only. As the sound field is limited to $r < R$ (see figure I.5), $\delta n(x, z) = 0$ for $x < A(-x)$ and $x > A(x)$ and the phase map $\delta\phi(x, z)$ is given by:

$$\begin{aligned}\delta\phi(x,z) &= \frac{2\pi}{\lambda}\int_{-A(x)}^{A(x)} \mathrm{d}y\ \delta n(\sqrt{x^2+y^2},z)\\ &= \frac{2\pi}{\lambda}\int_{-\infty}^{+\infty} \mathrm{d}y\ \delta n(\sqrt{x^2+y^2},z)\\ &= 2\frac{2\pi}{\lambda}\int_{0}^{+\infty} \mathrm{d}y\ \delta n(\sqrt{x^2+y^2},z)\\ &= 2\frac{2\pi}{\lambda}\int_{x}^{+\infty} \mathrm{d}r\ \frac{r\ \delta n(r,z)}{\sqrt{r^2-x^2}}\end{aligned} \tag{I.1}$$

which is, apart from a factor $\frac{2\pi}{\lambda}$, the Abel transform of $\delta n(r,z)$. Equation (I.1) can be inverted leading to :

$$\delta n(r,z) = -\frac{1}{\pi}\frac{\lambda}{2\pi}\int_{r}^{+\infty} \mathrm{d}x \frac{\partial(\delta\phi(x,z))}{\partial x}\frac{1}{\sqrt{x^2-r^2}} \tag{I.2}$$

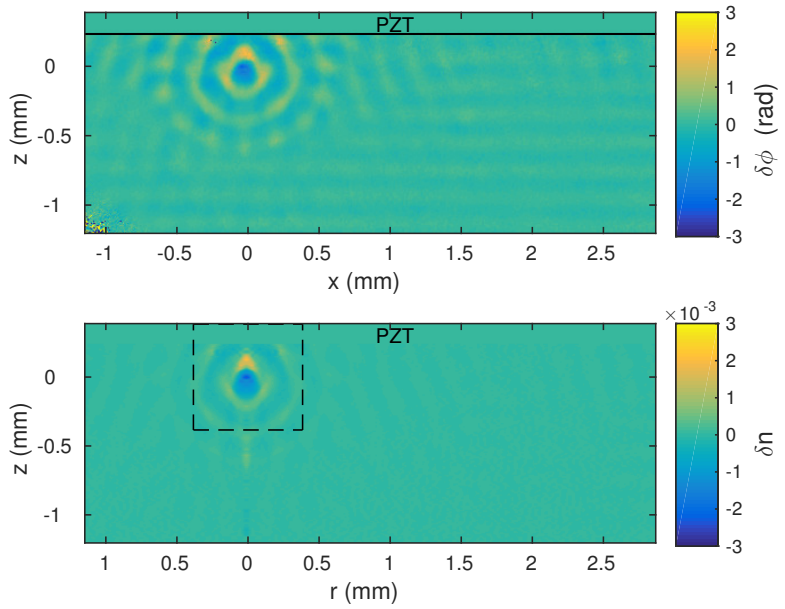

Fig.I.6: Experimental data showing an acoustic wave focused in liquid ^{4}He at about 1 K recorded at a given time of propagation t_0. Top panel: instantaneous phase map $\delta\phi(x,z)$ measured by the apparatus sketched in figure I.4. Bottom panel: corresponding refractive index variations $\delta n(r,z)$ after computations of the inverse Abel transform of $\delta\phi(x,z)$ (formula (I.2)). The dashed line limits the area considered in figure I.7 to show the time evolution $\delta n(r,z,t)$ of this particular set of data.

As we measure the function $\delta\phi(x,z)$ using the interferometric technique shortly described above, we are able to compute the integral of equation (I.2) for

different values of r (at constant z) and determine that way the $\delta n(r, z)$ function. The integral is calculated numerically using the algorithm proposed by Deutsch and Beniamy[6]. A typical example of data is shown in figure I.6.

The data of figure I.6 are recorded at a given time of propagation t_0. By varying the delay between the excitation of the transducer creating the wave and the laser pulse, we can record a movie of the wave propagation within the liquid. An example of such a refractive index variation movie is shown in figure I.7. For the sake of clarity, the sampling time interval shown on the figure is 200 ns but the sampling time is in fact 50 ns as in most of our experiments.

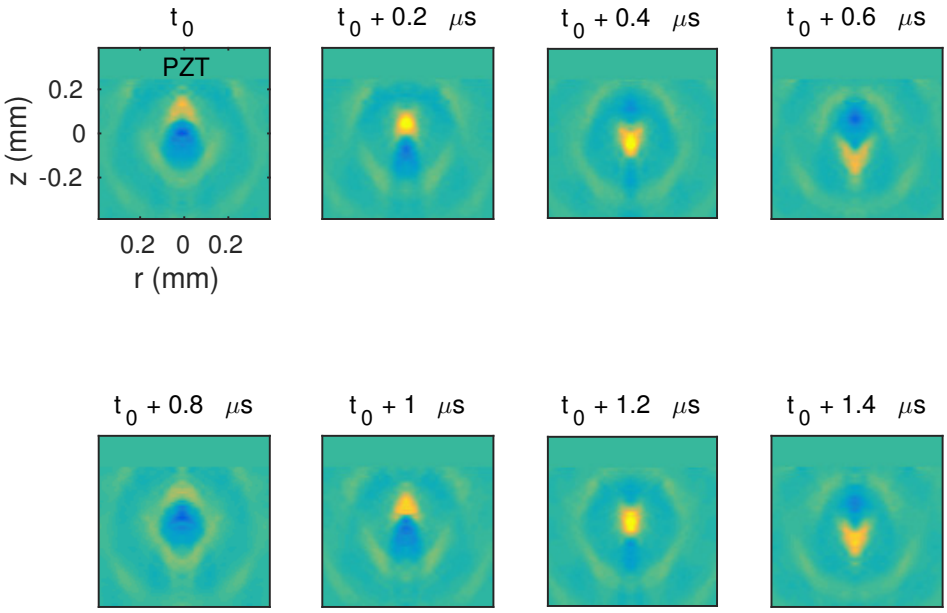

Fig.I.7: Time evolution $\delta n(r, z, t)$ as a wave propagates in liquid ^{4}He at about 1 K. The first image corresponds to the zoom (dashed line) of figure I.6 taken at a reference time t_0. As time goes on, one can clearly see the propagation of the wave which period is about 1 μs. The color scale is the same as in figure I.6.

These movies are the final output of our measurements. Some useful quantitative data can be extracted from them: radial refractive index profiles at a given time like the one shown on figure I.8a or the refractive index temporal evolution at a given point of space like the one shown in figure I.8b.

The method described here is a local density measurement resolved in time of liquid (solid) helium being perturbed by an acoustic wave. Indeed, from the

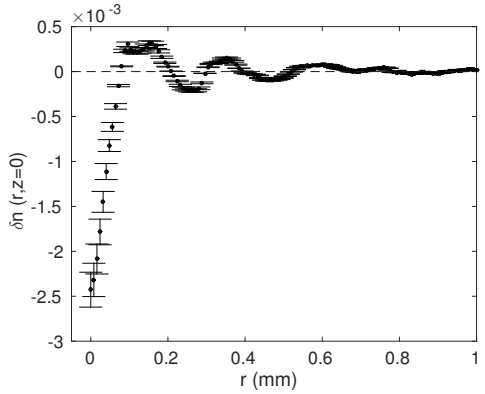

(a) Radial profile of refractive index variations $\delta n(r)$ of the data shown in figure I.6 at fixed $z = 0$ and fixed time t_0. The typical incertitude on δn is about 5 %.

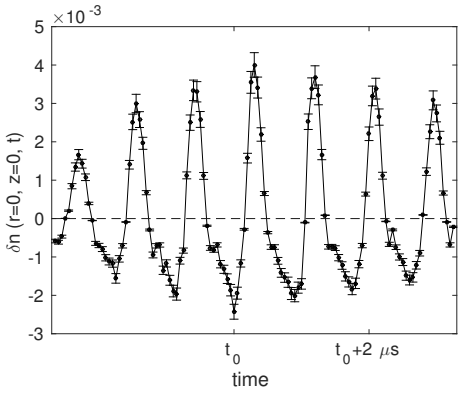

(b) Refractive index variation temporal evolution $\delta n(t)$ at acoustic focus ($r = 0, z = 0$) for the set of data containing the one of figure I.6.

Fig.I.8

refractive index variation maps $\delta n(r, z, t)$, the local density $\rho(r, z, t)$ is simply obtained by assuming the small polarizability limit ($n - 1 \ll 1$) of the Clausius–Mossotti relation $\dfrac{\delta n}{n_0 - 1} = \dfrac{\delta \rho}{\rho_0}$ which readily gives:

$$\rho(r, z, t) = \rho_0 + \delta\rho(r, z, t) = \rho_0 + \rho_0 \frac{\delta n(r, z, t)}{n_0 - 1}$$

Before applying this method to liquid (or solid) ^{4}He, it has been tested in water. The group of Frédéric Caupin which was at that time working in the same building as us, has developed an alternative method to measure the local refractive index variations induced by acoustic waves propagating in water. They use a so called fiber-optic probe hydrophone which is sketched on figure I.9b. A laser beam is coupled to 2×2 fiber optic coupler. Port 2 of the coupler is positioned at the acoustic focus of an hemispherical PZT emitter immersed in water. Port 4 is connected to a photodiode. Port 3 is not used. The light intensity recorded on port 4 gives a direct measurement of the time evolution of the water refractive index modulations $\delta n_{focus}(t)$ induced by the acoustic wave at acoustic focus as detailed in reference[7]. These can be directly compared to the ones deduced by our method.

We asked F. Caupin and his PhD student of the time A. Arvengas to come to our lab and perform this measurement in a transparent water tank we had designed for this occasion. For a given excitation of the PZT, the hydrophone measurement was performed and then our interferometric - Abel inverse measurement was performed. The results of both measurements made in the exact same experimental conditions are shown in figure I.9b. The comparison between both measurements is excellent as there is less than 5% deviation between the

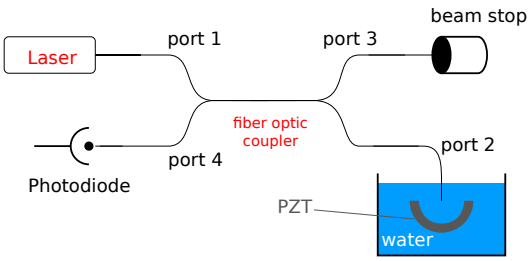

(a) Scheme of the fiber optic hydrophone apparatus. The light intensity recorded on port 4 gives a direct measurement of the time evolution of the water refractive index modulations $\delta n_{focus}(t)$ induced by the acoustic wave at acoustic focus.

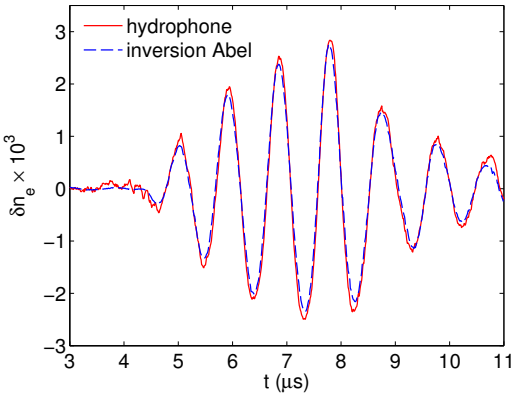

(b) Refractive index variation temporal evolution $\delta n_{focus}(t)$ at acoustic focus induced by an acoustic wave focusing in a water. Red Curve : hydrophone measurement. Blue dash Curve : Our interferometric method based on Abel inverse of phase map profiles

Fig.I.9

two curves and validates that the interferometric measurement is reliable.

I.3 Cavitation density measurement

I.3.1 Experimental results

The following section is a summary of the article "Cavitation density of superfluid helium-4 around 1 K"[8] published in Phys. Rev. B in 2015. It deals with our measurement of the cavitation density of ^{4}He at $T = 0.96$ K.

The basic idea of measuring the density at which cavitation occurs in liquid ^{4}He is the following. We send into the liquid an acoustic wave of amplitude large enough for cavitation of the liquid to occur. We measure the local density within the wave and find its minimum. The minimum density of the liquid when (or just before) cavitation occurs is the cavitation density.

"Cavitation" is observed on the images taken by the CDD camera. At $T = 1$ K and saturated vapor pressure, if cavitation occurs, a cavitation bubble expands to a macroscopic size ($\sim$ 300 μm) within $\sim$ 1 ms (this time is much larger than the sound pulse duration which is about 10 μs). In figure I.10, a typical signal of a cavitation event is shown.

From such signals, we can easily determine for which amplitude of the sound wave cavitation occurs. More precisely, we can determine the probability Σ to produce a cavitation event as a function of V the driving voltage of the PZT.

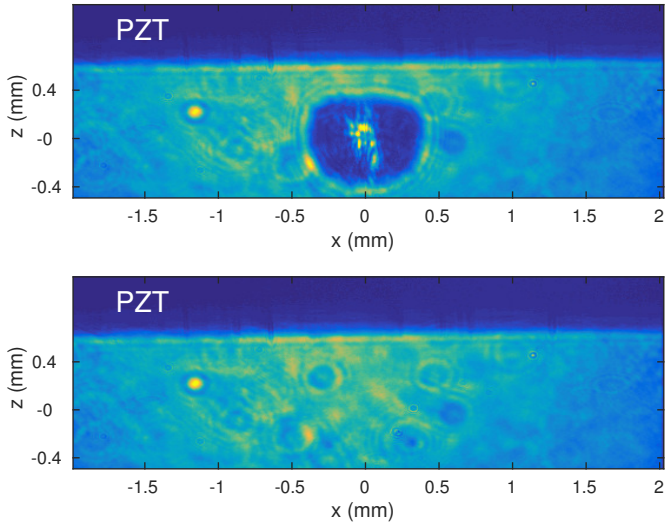

Fig.I.10: Detection of a cavitation bubble in ^{4}He at $T \sim 1$ K. Images are taken ~ 1 ms after the sound pulse (duration ~ 10 μs) has reached acoustic focus. Top panel: the acoustic wave has triggered the creation of a bubble, cavitation has occurred. Bottom panel: no cavitation.

The cavitation process is a random process because of the thermal fluctuations. According to F.Caupin *et al.*[9], its probability is described by the "asymmetric S-curve formula":

$$\Sigma(V) = 1 - \exp[-\ln 2 \exp(\xi(V/V_c - 1))] \tag{I.3}$$

where V is the excitation voltage, ξ a dimensionless parameter and V_c the cavitation voltage. The cavitation voltage is thus the value of the driving voltage corresponding to a bubble probability of 1/2. In order to determine V_c, we proceed as follows. For a given static pressure of the cell P_0, the bubble probability is determined for 5 different excitation voltages. Each voltage point corresponds to 1000 trials (1000 sound pulses) and the probability is then simply given by the number of positive events (creation of bubble) divided by the number of trials. As it can be seen in Fig.I.11a, the relative width of the curves is about 1% of V_c. These curves are indeed very sharp and for an excitation voltage V_{max} of about 2% below V_c, the probability $\Sigma(V_{max})$ is about 10^{-3}. This point is important to stress as our optical method needs smooth spatially phase variation in order to compute the local refractive index via eq.(I.2). Consequently, the density maps can not be easily measured at V_c because many images are blurred by bubbles. We then decide to measure density maps up to V_{max}.

For the driving voltage of the transducer $V = V_{max}$, we can then measure refractive index variation movies $\delta n(r, z, t)$ like the ones of figure I.7. From a straightforward analysis of these data, the minimum δn_{min} of $\delta n(r, z, t)$ in space

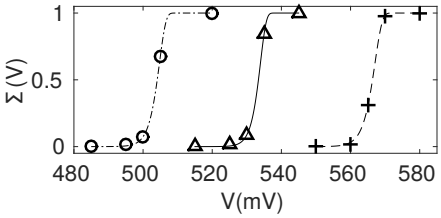

(a) Cavitation probability as a function of the transducer driving voltage V at 0.96 K for three different static pressures P_0 : circles, 0.15 bars; triangles, 0.65 bars; crosses, 1.26 bars. The corresponding lines are fits according to Eq.(I.3). The relative width of the curves is about 1% of their central values V_c.

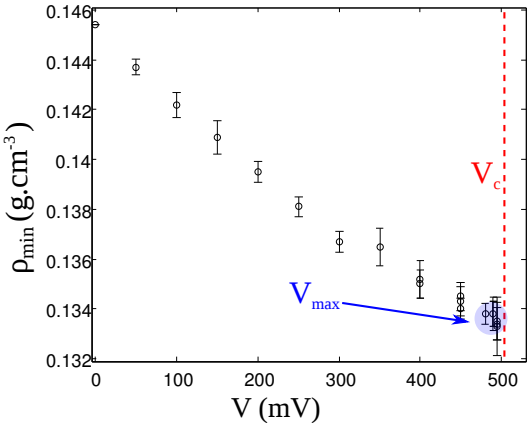

(b) Experimental measurements of minimum densities ρ_{min} for different driving voltages V at $T = 0.96$ K and a static pressure of the cell $P_0 = 0.15$ bars. The dashed line represents the cavitation voltage V_c at which the probability of having a bubble is 1/2. For $V = V_{max}$, the probability of having a bubble is about 10^{-3} and the density measurement is therefore possible to perform.

Fig.I.11

and time is found. We then determine the cavitation density by making the approximation:

$$\begin{aligned} \rho_{cav} &= \rho_{min}(V_c) \\ &\approx \rho_{min}(V_{max}) \\ &\approx \rho_0 + \rho_0 \frac{\delta n_{min}}{n_0 - 1} \end{aligned} \tag{I.4}$$

The validity of this approximation may be seen on figure I.11b on which the space-time minimum density is plotted as a function of the excitation voltage. It is clearly seen that assuming a local linear dependence of ρ_{min} on V, and taking into account the error bars[1], one can safely consider that ρ_{cav} is $\rho_{min}(V_{max})$.

In order to improve the accuracy in determining ρ_{cav}, a lot of measurements of the local density just below the cavitation are made. Another aspect to be checked is to know whether, at a given temperature (here 0.96 K), ρ_{cav} depends on the static pressure of the cell. Why this question is important will be explained

[1]The error bar on each measurement is about 5% which is the typical deviation between the results given by our inverse Abel technique and the optical hydrophone technique in the refractive index measurement of a sound pulse propagating in water (see end of section I.2)

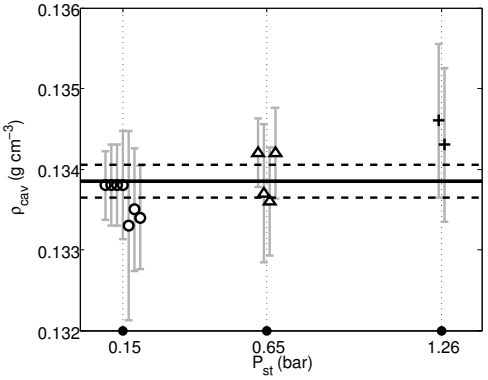

(a) Cavitation density as a function of static pressure at T = 0.96 K. For more clarity, the different measurements are shifted from their actual P st values (black circles). The horizontal continuous line represents the average cavitation density and the dashed lines its uncertainty

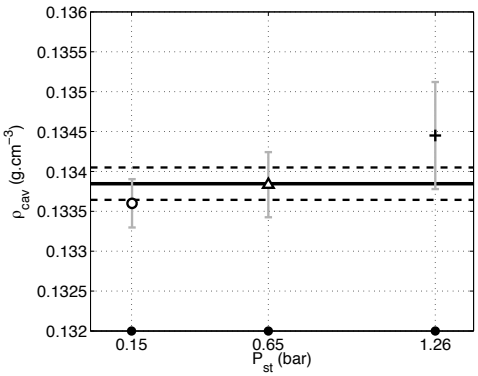

(b) Same as a) but data points for each static pressure are averaged. If ρ_{cav} depends on the static pressure, this dependence is weak, of the order of $\sim$ 0.6 %/bar.

Fig.I.12

in the next section I.3.2. On figures I.12a and I.12b, the cavitation pressure measured as explained before is plotted versus the static pressure. Within the error bars, it might be considered as constant as shown on figure I.12a. When data corresponding to each static pressure are averaged, the graph of figure I.12b is obtained. If some dependence of the cavitation density on the static pressure is to be found, it is then very weak, on the order of ~ 0.6 %/bar.

In the hypothesis of independence of the cavitation density to the the static pressure, the mean of the data points of figure I.12a and the corresponding error bar can be computed. According to our measurements, the cavitation density of liquid ^{4}He at $T \sim 1$ K, is

$$\rho_{cav}(0.96\,\mathrm{K}) = 0.1338 \pm 0.0002\,\mathrm{g/cm}^3 \tag{I.5}$$

I.3.2 Discussion

The value given by (I.5) turns out to be quite interesting when compared with previous works. As I already mentioned at the beginning of this chapter, other groups measured the cavitation pressures of liquid ^{4}He instead of cavitation densities.

The equation of state (EOS) of liquid helium in its metastable state (density and pressure below the boiling curve values) is needed to convert the ρ_{cav} to a corresponding P_{cav}. Although such an equation of state has never been measured

experimentally, some have been proposed. Maris has pointed out that, in the stable phase at $T = 0.1\ K$, the sound velocity versus pressure can be fit very well by the law $c^3 = b(P - P_c)$ with c the sound velocity, P the pressure, P_c the spinodal pressure and b a constant [10]. He proposed that this relationship holds in the metastable state (negative pressure). Bauer *et al.* have performed Path-integral Monte Carlo simulations of liquid helium in the metastable state at finite temperature and found the same dependence of sound velocity on pressure[11]. Dalfovo *et al.* have calculated the EOS of metastable liquid helium at $T = 0\ K$ using density-functional approach[12], and Boronat *et al.* using a quadratic diffusion Monte Carlo method to achieve a similar EOS[13]. The EOSs at $0\ K$ agree within a few percent. Moreover, using the density-functional theory of Dalfovo *et al.*, Maris and Edwards have shown that in the temperature range $0 < T < 1\ K$, the EOS is nearly independent of temperature[14].

So in order to compare our cavitation density result to cavitation pressure results of other experiments, we use the theoretical EOS for metastable liquid helium at $T = 0\ K$ and assume it holds for $T = 0.96\ K$. By doing so, the value of our measurement of the cavitation density at 0.96 K (eq (I.5)) can be converted to a cavitation pressure:

$$P_{cav}(0.96\,\mathrm{K}) = -5.1 \pm 0.1\ \mathrm{bar}$$

This result is surprising. Indeed, at temperatures ∼1 K, in addition to our experiment, there are to my knowledge only two experiments which studied the cavitation of liquid helium. These are the ones of Maris and Balibar[2]. Xiong and Maris [15] found the cavitation pressure at $1\ K$ is ~ -3 bar. The incertitude mentioned in this paper is about ±10%. The cavitation pressure measurement is rather indirect as it comes from a calculation of the pressure at acoustic focus knowing the displacement of the emitter. Non-linear effects were not taken into account in their calculation. So the uncertainty is likely to be underestimated. Actually, when I questioned Maris about his -3 bar result, he told me that "the estimate of the pressure swing was not "very reliable"".

Caupin *et al.*[9] studied the dependence of cavitation voltage V_c to the static pressure P_{stat}. They claim that this method enables them to set an upper limit for the actual cavitation pressure. The idea of their measurement reads as follows. They imagine a situation where it could be possible to have the liquid in the cell at a negative static pressure. In that case, when the static pressure of the cell corresponds to the cavitation pressure ($P_{stat} = P_{cav}$), cavitation spontaneously occurs without any help from the acoustic wave. In other words, in this scenario $V_c = 0$ for $P_{sat} = P_{cav}$. If the sound wave propagation were a purely linear process, the pressure variation induced by the wave ΔP at acoustic focus would be proportional to the amplitude of the driving voltage and to the static density

[2]Nissen measured the tensile strength of liquid ^{4}He only between 4 K and 1.5 K[2]

ρ_0 of the liquid. The dependence of ΔP on ρ_0 comes from the fact that in the linear regime, $\Delta P_{focus} = \rho_0 c u$ where u is the local particle velocity and c is the local speed of sound. Since u is proportional to V, in the linear regime, the relation

$$\Delta P_{focus} = \alpha \rho_0 V$$

(α is a constant) is expected to hold. Based on this linear relation, Caupin *et al.* decided to measure the product $\rho_0 V_c$ as function of the static pressure in the cell. The idea being that if the focusing of the sound wave was a strictly linear process, the curve $P_{stat} = f(\rho_0 V_c)$ would look like the dashed line of figure I.13a. They argue that non linearities in the sound propagation from the emitter surface to the acoustic focus would make the real curve curvature to be concave[16](solid line on figure I.13a). If so, the local linear extrapolation (red solid curve on the figure) of the measured experimental data points ($P_{stat} > 0$, $\rho_0 V_c$) to the value $V_c = 0$ must give an upper bound of the cavitation pressure (P_{max} on the figure).

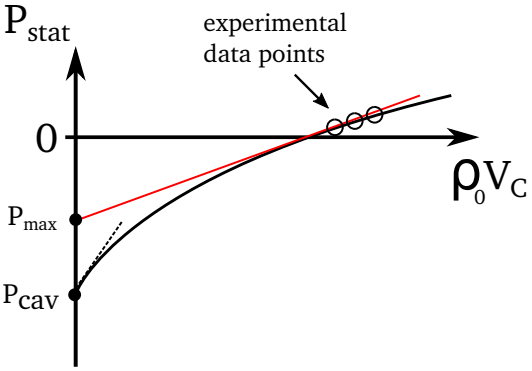

(a) Principle of Caupin *et al.*'s method to estimate the cavitation pressure by measuring the product $\rho_0 V_c$ (ρ_0 is the static density and V_c the cavitation voltage as defined in text). The linear extrapolation (red curve) of the experimental data points (black circles) to $V_c = 0$ give an upper bound P_{max} of the real cavitation pressure P_{cav}. The meaning of solid and dashed black lines are detailed in the text.

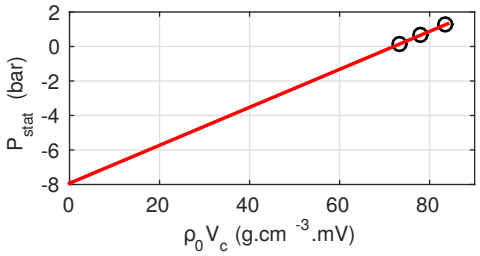

(b) Applying Caupin *et al.*'s method, we found at $T = 0.96$ K an upper bound of the cavitation pressure $P_{max} = -8$ bar. Error bars are smaller than the data point sizes.

Fig.I.13

Applying this method, Caupin *et al.* found:

$$P_{cav_{Caupin}}(0.9\text{K}) < -7.7 \text{ bar}$$

We have reproduced their experiment and found a very similar result: $P_{cav_{extrapol}}(0.96\text{K}) < -8$ bar as it can be seen on figure I.13b.

The cavitation pressure -5.1 bar estimated from the cavitation density measurement via the use of the theoretical EOS of metastable liquid helium is clearly not compatible with the one estimated by the extrapolation method of Caupin *et al.*.

This is an important result. One way to solve the disagreement between these two different measured values for the cavitation pressure of liquid helium at $T \sim 1$ K would be to show that the theoretical EOS is not accurate and that a better one would reconcile the two measurements. For that, it appears necessary to measure experimentally the equation of state of metastable liquid helium. Of course, the theoretical EOS could be correct and then the difference between the two measurements must lie somewhere else. For instance, the curve P_{stat} versus $\rho_0 V_c$ (solid line of figure I.13a) could be more complicated than assumed. I'll discuss in the last chapter of the manuscript how I plan to measure experimentally the EOS of metastable liquid helium.

I.4 Lifetime of cavitation bubbles

I'd like now to discuss another property of acoustically driven cavitation bubbles. Indeed, while doing the cavitation density measurements, we realized that the typical lifetime we observed for our cavitation bubbles was strongly dependent on whether liquid ^{4}He was superfluid or not. The following section is a summary of our article "Dramatic effect of superfluidity on the collapse of ^{4}He vapor bubbles"[17] published in *Phys. Rev. B* in 2016.

I.4.1 Experimental set-up

By lifetime of the bubble, we mean the time interval during which the bubble is created, grows, collapses, and eventually disappears. To measure this lifetime, we use the experimental set-up sketched in figure I.14. The main difference with the set-up used for the density measurement (figure I.4) is the replacement of the Jamin mirror by a regular mirror. No interferometric measurement is made here. We simply take images of the bubbles at different times after their creation.

If we had a fast enough camera, the bubble lifetime measurement would be pretty straightforward. We would simply illuminate the acoustic focus with continuous laser and record single bubble evolution and determine their lifetime. Unfortunately, we don't have such a fast (and expensive) camera.

So, the method we use is the following. Our pulsed laser (8 ns pulse width) enables us to take snapshots of the acoustic focus plane (see section I.2) at a given time t where $t = 0$ is the time at which the transducer is excited. t is tuned simply by changing the delay between the laser pulse and the electric

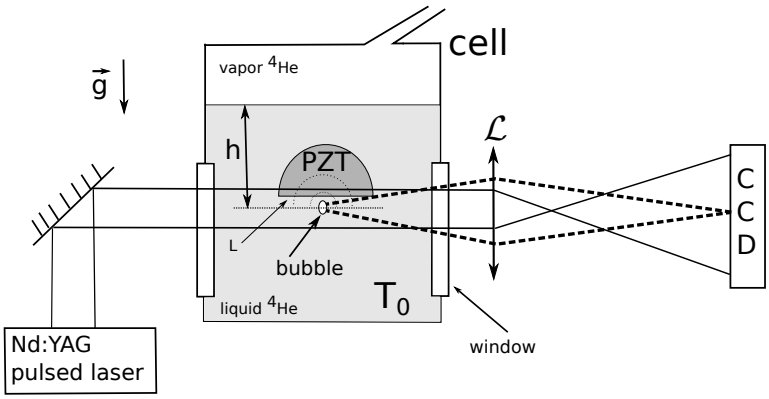

Fig.I.14: Experimental set up used to measure the lifetime of cavitation bubbles in liquid ^{4}He between 0.9 and 4 K. A (single) beam of a pulsed laser is used to shine the area where an acoustic cavitation is produced. A lens $\mathcal{L}$ images the acoustic focus plane (where the bubble is created) onto a CCD camera. L is the thickness removed from the originally hemispherical transducer which enables us to image the acoustic focus. h is the distance between the acoustic focus and the vapor/liquid interface surface along the gravity line $\vec{g}$.

generator feeding the transducer. We first set $t = t_p$ short compared to the typical lifetime of the bubbles τ (typically superior to 1 ms as we shall see later). For $t_p < \tau$, we determine the cavitation voltage V_c (see section I.3). Then we set the driving voltage of the transducer to a value V_1 of typically $V_1 = 1.02\, V_c$ so that the probability of cavitation (at short times) is 1 (see figure I.11a). Keeping V_1 constant, we change t and measure the probability $p(t)$ of still having a bubble at time t. We determine $p(t)$ by recording N images of the acoustic focal plane at time t and by counting the number of images $N_b(t)$ containing a bubble. One readily gets $p(t) = N_b(t)/N$. It is important here to stress that this temporal evolution is a statistical one. We don't measure with this technique the lifetime of single bubbles but rather the mean lifetime of a collection of different bubbles created in the same experimental conditions.

I.4.2 Experimental results at $T_0 < T_\lambda$

We will show soon after that in this temperature range, the typical lifetime τ is about 1.5 ms. This is much larger than the sound pulse duration (~ 10 μs). Hence, at the end of the sound pulse, the bubble does not have its maximum radius. It is small and begins an expansion motion. Then it reaches its maximum radius R_0 and finally collapses at time $t = \tau$. During this time, buoyancy can be neglected as, noting g the earth gravity, the maximum displacement the bubble

can do[3] is $g\tau^2 = 20$ μm which is very small compared to the size of the field of view ($\sim$ 1 mm). Figure I.15 a) shows a typical set of images of collapsing bubbles at $T_0 = 0.87$ K ($< T_\lambda$) recorded at different times t. One can see that the center of mass of the bubbles is not moving with time, whereas the radius is decreasing with time : the bubble is collapsing where it was created. This point is very important as we don't miscount $N_b(t)$ simply by loosing bubbles escaping the field of view.

The lifetime τ of a cavitation bubble is expected to depend on several parameters, and notably on the maximum radius R_0 it can reach[18]. For the bubbles we produce, we have measured that the distribution of R_0 is roughly gaussian around a mean value of 300 μm with a standard deviation of about 10%. Hence τ is a random variable distributed around a mean value.

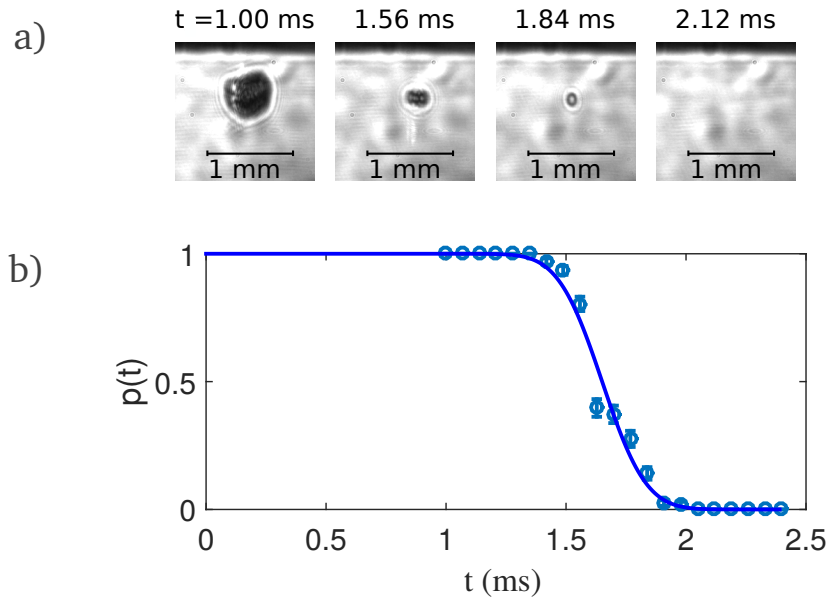

Fig.I.15: Determining the lifetime of cavitation bubbles: data for $T_0 = 0.87$ K. a) Images of typical bubbles at different times t (see text). The upper rectangular black area is the shadow of the PZT. b) Probability of existence of a bubble at time t. The solid line is a fit assuming that the lifetime of the bubble is gaussian distributed. For these data, the mean value $< \tau > = 1.65$ ms with a standard deviation $\xi = 0.10$ ms.

Let $s(t)$ be the probability density function of τ, then the quantity $p(t)$ is given by $p(t) = 1 - F(t)$ where $F(t) = \int_0^t s(t')dt'$ is the partition function of $s(t)$. If one assumes that $s(t)$ is gaussian, then experimental data should be fitted by the function $p(t) = \frac{1}{2}(1 - \mathrm{erf}(\frac{t-\langle\tau\rangle}{\xi}))$ where erf is the error function, $\langle\tau\rangle$ the mean lifetime of the bubble and ξ its standard deviation. Indeed Figure

[3] not $1/2g\tau^2$ because the effective inertial mass of a bubble is one half that of the displaced liquid.

I.15b) shows that such a fit reproduces the data pretty well and enables us to determine the bubble mean lifetime. We have performed these experiments at several temperatures below the λ-point. The results are shown on the left part of Figure I.17. In this temperature range, the lifetime of bubbles is roughly independent of T_0 and its value is 1.5 ± 0.2 ms.

I.4.3 Experimental results at $T_0 > T_\lambda$

The bubble lifetime at $T_0 > T_\lambda$ is much longer. Although bubbles are always created at the very focus of the acoustic wave, we have seen that, at later times, they become randomly distributed over the field of view as one can see on figure I.16. At a given time, there is a chance for a bubble to escape the imaged region and become undetected. Then the quantity $N_b(t)/N$ no more represents the probability of existence at time t. The only statement we can make is that the lifetime of bubbles in these experiments is bounded by a lower value corresponding to the highest value of t where $N_b(t) \neq 0$.

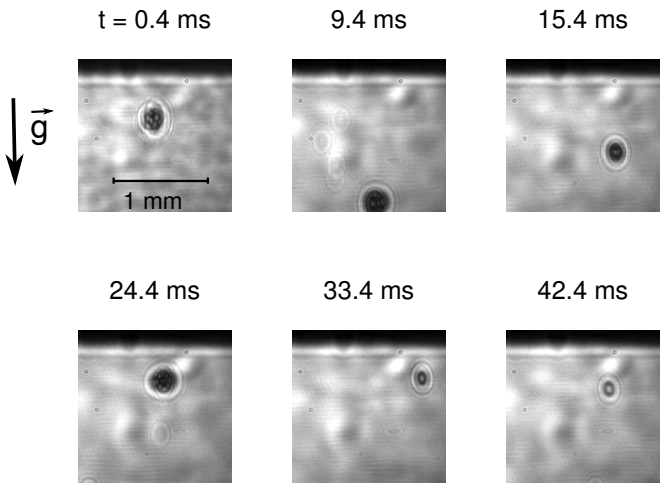

Fig.I.16: Cavitation bubbles at $T_0 = 2.19$ K.

This difference is especially remarkable when looking at the bubble lifetime as a function of temperature as shown in figure I.17. The lifetime being in log scale on the figure, one can see that it undergoes a dramatic transition while crossing the λ point.

I.4.4 Discussion

What can make such a difference between the lifetime of bubbles produced in the superfluid and in the normal fluid? According to many authors (see for

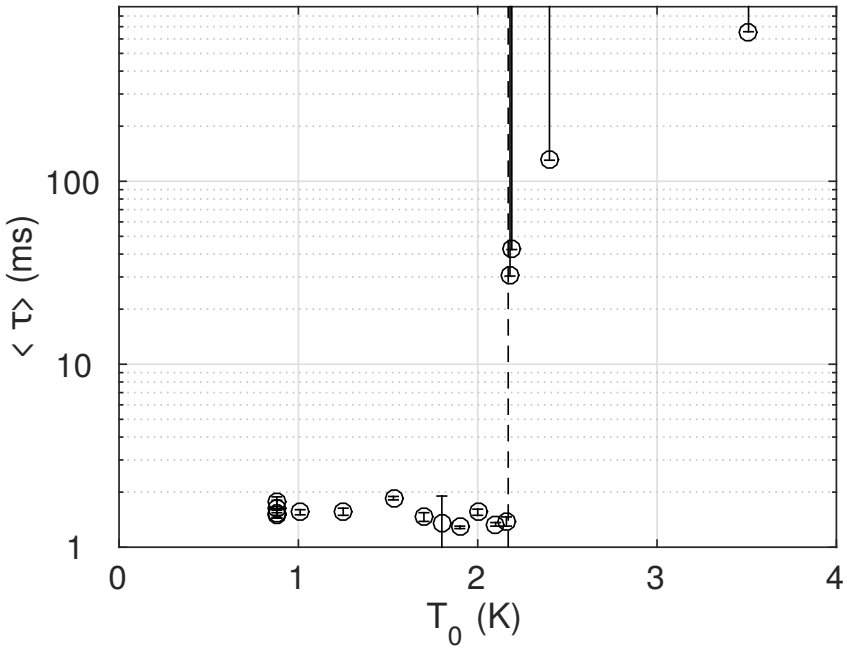

Fig.I.17: Lifetime of bubbles in liquid helium as a function of temperature. The vertical dashed line marks the superfluid transition temperature ($T_\lambda = 2.17$ K). Above T_λ, we can only estimate the lower bound of the lifetime.

instance [19]), the dynamics of the bubble radius is governed by the so called Rayleigh-Plesset equation :

$$R\ddot{R} + \frac{3}{2}\dot{R}^2 = \frac{1}{\rho}(p_v(T) - P_0 - 2\sigma/R - 4\mu\dot{R}/R) \tag{I.6}$$

where R is the bubble radius, dots represent time derivatives, ρ is the liquid density, σ the surface tension of the liquid/vapor interface, μ the liquid viscosity, $p_v(T)$ is the vapor pressure of the liquid/vapor mixture at the temperature T of the gas inside the bubble, and P_0 is the static pressure far from the bubble interface. In our configuration, we have $P_0 = p_v(T_0) + \rho g h$, where h is the distance between the bubble center and the liquid/vapor equilibrium coexistence plane (see Fig.I.14). The main difficulty in solving eq. (I.6) is to model the time dependence of T.

The dynamics of the bubble collapse is thus governed by the way heat from the condensation of the gas is extracted away form the surface of radius R.

In the superfluid case, heat is very efficiently transported by the propagation of a second sound wave [20]. If any temperature gradients appear on a length scale of about R_0, they will vanish in a typical time R_0/v_s where $v_s = 20$ m/s is the speed of second sound. As $R_0/v_s \approx 50\ \mu\text{s} \ll 1.5$ ms, we assume that in the superfluid, growth and collapse of the cavitation bubbles are isothermal

processes. Setting $T = T_0$ in equation (I.6), the problem becomes a purely mechanical one and the equation is pretty easy to solve at least numerically. We decided to compute only the collapse time evolution (and not growth and collapse) because initial conditions are much better known in that case. Indeed, experimentally, we can measure $R(0)$ at the beginning of the collapse using our recorded images (see figure I.15 a)) and we can certainly assume that $\dot{R}(0) = 0$. We then assume that growth and collapse are symmetric with respect to time. On figure I.18 a), we plot the mean radius of the bubble as a function of time determined by our movie reconstruction method and compare it to the solution of eq. (I.6).

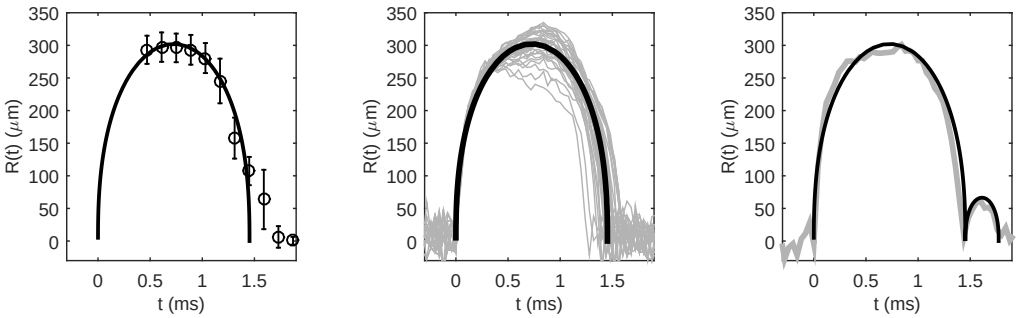

Fig.I.18: Bubble radius as a function of time at $T_0 \sim 1$ K. On all figures, black solid line is the solution of the Rayleigh-Plesset equation (eq.(I.6)) in the approximation $T = T_0$. a) Data points from the movie reconstruction method (see text and figI.14). b) Signals collected with a fast photodiode. c) Another photodiode measurement : after the bubble has collapsed, a second bubble is created.

Apart from one point (point n° 9), one sees that the Rayleigh-Plesset theory with $T = T_0$ reproduces the data well. To further validate these results, we have recorded the light scattered by collapsing bubbles using a fast photodiode. We then were able to follow the time evolution of a single bubble and not of a statistical ensemble. The photodiode was placed at the focal length of lens $\mathcal{L}$ of figure I.14. When no bubble is present, the voltage of the photodiode V_0 is maximum and corresponds to the total laser beam intensity of section S_0. A bubble of cross section $\pi R^2(t)$ will scatter light off of the photodiode so that the voltage $V(t)$ will decrease as $V(t) = V_0(1 - \pi R^2(t)/S_0)$. $V_0 - V(t)$ gives a measurement of $R^2(t)$. Knowing that $R_{max} = 300$ μm from the CCD images, we can calibrate the voltage of the photodiode to obtain a real measurement of the bubble radius as a function of time. These photodiode measurements are shown on figures I.18 b) and I.18 c). On figure I.18 c), we see that after a cavitation bubble has collapsed, a rebound bubble can be created. This rebound can also be explained by the Rayleigh theory. The probability of such a rebound is about

70 %. This explains the deviation of point n° 9 in I.18 a) and its larger variance. In Figure I.18 b), only bubbles without a rebound are shown : the Rayleigh solution fits well the results. Our conclusion is that for $T_0 < T_\lambda$, the cavitation dynamics is purely mechanical (heat effects may be neglected), a conclusion supported by the fact that the bubble lifetime is independent of temperature.

For $T_0 > T_\lambda$, the bubble lifetime is higher by at least 1 or 2 orders of magnitude than in the superfluid state.

In the normal state, heat is transported by thermal diffusion. A gradient of temperature appears so that the pressure inside the bubble is equal, but for the Laplace term, to the external pressure. This dramatically slows down the collapse of the bubble. To have an order of magnitude of the time of the collapse in this case, one can consider the Fourier heat diffusion law in spherical symmetry $\vec{j} = -\kappa\vec{\nabla}T$ where $\vec{j}$ is the heat flux density (expressed in W/m^2) and κ the thermal heat conductivity expressed in W/m/K. Assuming that the temperature gradient is extended from the radius of the bubble to infinity, the Fourier law gives $\kappa(T - T_\infty) = \frac{\dot{Q}}{4\pi R}$ where T is the temperature of the liquid at the bubble surface, T_∞ the temperature of the cell, $\dot{Q} \approx \frac{Q_{out}}{\tau}$ the heat flux escaping the bubble, Q_{out} is the latent heat of condensation which must be evacuated off the bubble while collapsing and τ is lifetime of the bubble. We set $Q_{out} = n(T)L$ with $n(T)$ the number mole of gas in the bubble at temperature T and L the molar latent heat of condensation. The temperature T might be estimated by assuming that $P_v(T) - P_v(T_\infty) \approx \rho g h$, in the limit $\rho g h \ll P_v(T)$ one can linearize the vapor pressure versus temperature curve so that $(T - T_\infty) = P_v(T) - P_v(T_\infty)/\alpha$ where α expressed in Pa/K and is given by the Clapeyron relation $\alpha = \frac{LP_v(T)}{RT^2}$. Finally, an order of magnitude of the lifetime of the bubble in the normal state is given by $\tau = \dfrac{P_v^2(T)L^2R^2}{R_g^2T^3\kappa\rho g h}$ with R_g the gas constant. Plugging in the numbers for liquid helium at 2.18 K[4] and $h = 1.4$ cm as determined from the lifetime of bubbles in the superfluid case, we find a lifetime in the normal state as high as $\tau \sim 56$ s. Whether this order of magnitude corresponds to reality cannot be checked experimentally because of the buoyancy of the bubbles. Indeed, the expected change in height is given by $\frac{2R_0^2\rho g t}{9\mu}$ which is about 500 m for $t = 50$ s. However it is clear that heat transport is the mechanism that governs the dramatic transition in the bubble lifetime at T_λ.

During this study, we discovered an interesting property of metastable liquid ^{4}He. The lifetime of cavitation bubbles undergoes a severe transition while crossing the λ point. In the superfluid state, the bubble lifetime is found to be consistent with the Rayleigh model in which heat effects are ignored. On the contrary, in the normal state of the liquid, one has to take into account the

[4]these are $P_v(2.18\,\text{K}) = 5000$ Pa, $L = 91$ J/mol, $\kappa = 23$ mW/m/K, $\rho = 146$ kg/m^3

diffusion of the latent heat of condensation which dramatically slows down the bubble collapse. It is interesting to note that the group of Ambarish Ghosh in Bangalore (India) have also reported very different lifetimes of exploding electron bubbles in liquid ^{4}He on both sides of the λ transition[21]. The group of Ladislav Skrbek in Prague (Czech Republic) has imaged heterogeneous cavitation bubbles induced by a vibrating quartz fork and also finds important differences between the lifetime of the bubbles in the normal fluid and in the superfluid[22].

Chapter II

Metastable Solid Helium-4

II.1 Principle of the experiment and motivations

When I joined in 2009 the group of Prof. Jacquier, my project was to produce and study Metastable Solid ^{4}He. The work presented here was mostly done during the PhD of F. Souris[4] between 2009 and 2013. The first motivation was that Metastable Solid ^{4}He has never been studied. Solid helium below its melting pressure was also appealing because it could be a way to achieve "supersolidity".

II.1.1 Supersolidity

In 1969, Andreev and Lifshitz [23], and independently Chester [24], developed a model describing what is now known as the ALC scenario to supersolidity. This "scenario" predicted that vacancies are free to move inside the crystal, and thus form a perfect gas. If the energy for creating a vacancy were low enough, their

density might be high enough that they form a Bose Einstein Condensate and the gas of vacancies would become superfluid. If vacancies behave like a superfluid gas inside the crystal, the crystal itself, while remaining crystalline, with well defined lattice planes, should be superfluid and could flow without dissipation. This paradoxical behavior was coined as supersolidity. However, until 2004, nobody had ever obtained experimental evidence for this supersolidity.

An experiment by Kim and Chan in 2004 [25, 26] has reactivated the domain. They discovered an inertia anomaly in solid helium that they interpreted as appearance of a supersolid state. The measured effect was the drop in the period of a torsional oscillator filled with solid helium when temperature is lowered below $T_c \sim 200$ mK. Many other torsional oscillator experiments have then been achieved in order to measure this so called Non Classical Rotational Inertia (NCRI, see for instance [27, 28, 29, 30]) and have confirmed the effect with however a spread in the estimated supersolid fraction ranging from 0.01% to 20% depending on the crystal quality.

However, in 2007, Day and Beamish have shown that an increase of the shear modulus occurs below temperatures close to T_c, probably due to dislocations getting blocked on ^{3}He impurities at low temperature [31].

This was a very important result because it could question the supersolid interpretation of the torsional oscillator period drop. Indeed the resonant period $\tau(T)$ of a torsional oscillator at temperature T is given by:

$$\tau = 2\pi\sqrt{\frac{I(T)}{K(T)}}$$

where $I(T)$ and $K(T)$ are respectively the moment of inertia and the torsion constant of the torsional oscillator which both depend on the temperature of the sample. A reduction of τ as the temperature is lowered may be due to a decrease in I or an increase of K or a combination of both effects. K depends on the elastic properties of the torsional oscillator and hence on the elastic properties of the solid helium contained in it. The increase of the shear modulus of solid ^{4}He below T_c can stiffen the torsional oscillator and then increase the torque constant K.

A lot of theoretical works have been done to try to investigate the two effects, including works considering the superfluidity of dislocation networks within the crystal. Many experiments have tried to separate signals potentially due to elastic and supersolid causes[32]. In a paper in 2012, Beamsih, Balibar and co-workers made a careful inventory of all existing torsional experiments and analyzed how important was the elastic effects contribution to the still called NCRI signals[33]. Their analysis showed that in 2/3 of the torsional oscillator experiments, the measured signal could be totally explained by elastic properties of solid ^{4}He. The same year, the same Chan that had initiated all the excitement about a possible superfluidity of solid ^{4}He with his 2004 experiment[25, 26],

has published the paper "Absence of Supersolidity in Solid Helium in Porous Vycor Glass"[34] where he was repeating his 2004 experiment but with a torsional oscillator designed to minimize the elastic effects of solid ^{4}He. No drop in the period of the torsional oscillator was measured. Nowadays, there is a general agreement that no convincing supersolid signal has been observed in solid ^{4}He[1].

During this quest of supersolidity, the initial ALC scenario of supersolidity was mostly abandoned by the community. Mainly because Monte Carlo simulations [38] and measurements [39] have already shown that the activation energy of a vacancy in hcp solid ^{4}He was about $Q = 10$ K so that the thermal population of vacancies at T_c is governed by an exponential law $e^{\frac{-Q}{T_c}}$ resulting in a number density far too small for obtaining Bose Einstein Condensation. Indeed, assuming the very simple model of a perfect gas of vacancies in solid ^{4}He, the Bose Einstein Condensation condition is given by :

$$n_v \lambda_{dB}^3 = 2.612 \tag{II.1}$$

where n_v is the vacancy density (in m^{-3}) and $\lambda_{dB} = \sqrt{\frac{2\pi\hbar^2}{m_v k_B T}}$ is the de Broglie wavelength of a vacancy of effective mass m_v.

The crucial idea of our experiment is to find if the condition II.1 can be fulfilled by lowering the vacancy activation energy Q and thus increasing n_v at constant temperature. This is a different approach to the supersolidity search where other investigators were looking for the supersolid by decreasing temperature.

The activation energy of a vacancy measured by Fraass *et al.*[39] decreases as the molar volume increases as seen in figure II.1.

The absence of solid below above a molar volume of about 21 cm^3/mol limits the decrease of the activation energy of vacancies. A naive, but tempting, linear extrapolation suggests that, if the molar volume could be extended to $\sim$ 22 cm^3/mol, the vacancy energy would become extremely small, and might even be low enough for equation (II.1) to be fulfilled at temperature of about 1 K.

In order to check if it is possible to reduce the activation energy of vacancies, our group started an experiment aiming at producing and studying solid ^{4}He at molar volume above 21 cm^3/mol.

[1] I must mention that at least two kind of experiments with solid ^{4}He are still under debate about a possible supersolid signature, these are (i) mass flow experiments initially proposed and performed by Hallock[35, 36] and (ii) the recent multiple mode torsional oscillator where Reppy and co-workers argue that they can strictly distinguish between NCRI and elastic effects[37]

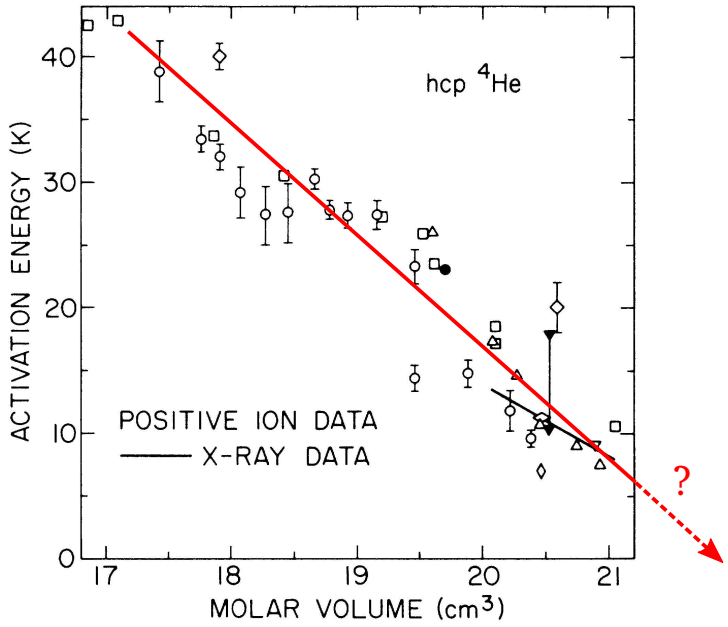

Fig.II.1: X-ray measurements of activation energy of vacancies in hcp solid ^{4}He as a function of molar volume[39]. It decreases fairly linearly down to its value $\sim$ 10 K at $V_m \sim 21$ cm^3/mol corresponding to the melting pressure ($\sim$ 25 bar and almost independent of temperature between 0 and 1.4 K, see figure II.2) . It is tempting to extrapolate this tendency to higher values of the molar volume.

II.1.2 Metastable solid ^{4}He

This molar volume (21 cm^3/mol) defines the melting line of solid ^{4}He between 0 and 1.4 K, where the melting pressure (25 bar) is almost independent of temperature (see figure II.2).

As for the liquid case (chapter I), metastable solid helium-4 can be obtained using a focused acoustic wave. The principle of the method adapted to solid case is recalled on figure II.2. An appropriate piezo electric transducer creates a focused pressure/density wave within the solid. The initial pressure of the solid (point A in the figure) is chosen a little above the melting pressure. This ensures that the wave amplitude is low enough at the inner surface of the transducer for the surface-pressure never becoming lower than the melting pressure (or the crystal would locally melt). During propagation, the amplitude of the focused acoustic wave becomes large enough to create hcp metastable solid ^{4}He.

Compared to the liquid case, a difficulty arises from the anisotropy of the sound propagation in hexagonal close-packed (hcp) solid helium-4.

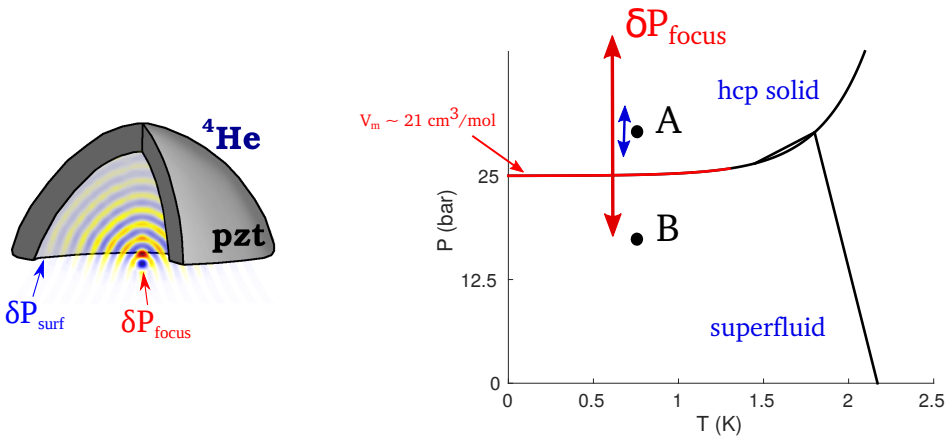

Fig.II.2: Pressure temperature phase diagram of ^{4}He at low temperatures. An appropriate piezo electric transducer creates a focused pressure/density wave within the solid. The pressure variations at the surface of the transducer are small enough not to cross the melting line and melt the crystal locally. As the wave propagates, the density variations increase and the crystal can explore a part of the phase diagram where ^{4}He is liquid at thermal equilibrium. A crystal of ^{4}He at point B is in a metastable state.

II.1.3 Sound velocity anisotropy in hcp solid helium

The hcp structure is shown on figure II.3a.

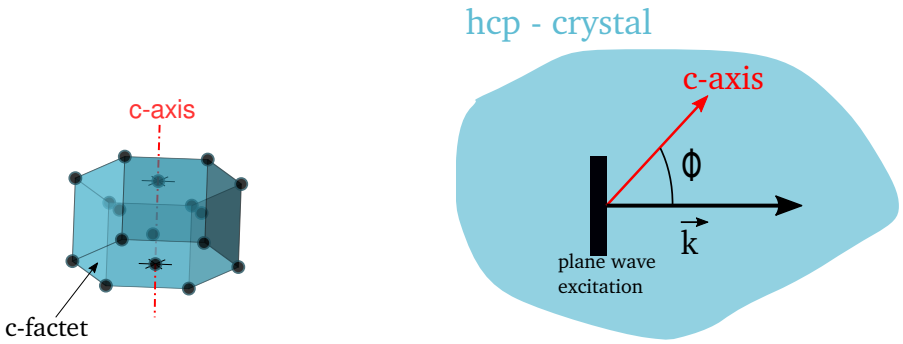

(a) (b)

Fig.II.3: a) Hcp crystal structure. The crystal is invariant over 120° rotation around its so called "c-axis". b) Anisotropy of sound velocities in a hcp crystal. In a hcp crystal, when one excites an elastic plane wave of wave vector $\vec{k}$, its phase velocity depends on the angle ϕ between the c-axis and the vector $\vec{k}$.

In a hcp crystal, sound velocity is not isotropic. A pressure/density wave front

originating from a point source is not a sphere but has an ovoid shape extended along the radial symmetry axis of the crystal ("c-axis"). Hence hemispherical transducers do not produce focused sound waves in that case. Actually, the propagation of elastic waves in an anisotropic solid is not a trivial problem. Musgrave has developed relatively simple equations for the case of hcp structure in order to find the wave surfaces from the five elastic constants needed to describe a hcp crystal[40]. He shows that only three modes of elastic waves can propagate, a pure transverse wave (shear wave) often labeled T_1, a quasi-transverse mode labeled T_2 and a quasi-longitudinal wave labeled L. In the following, we will mostly consider this L-wave.

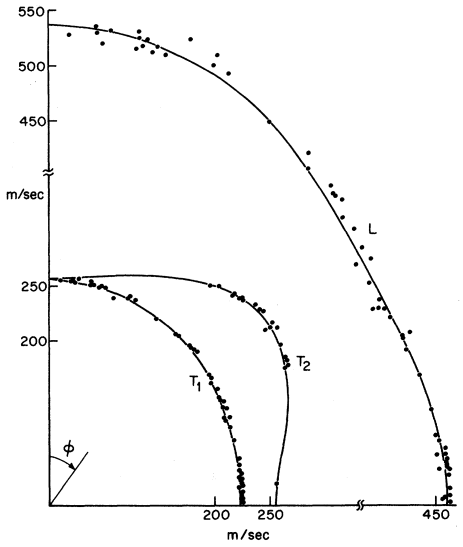

(a) Crepeau *et al.* [41] phase velocity surface measurements in hcp solid ^{4}He (see text). ϕ is the angle between the c-axis of the crystal and a plane wave excitation of wave vector $\vec{k}$. Three acoustic modes can propagate in a hcp solid, a pure transverse one T_1, a quasi transverse one T_2 and a quasi longitudinal one L. This latter one is maximizing the molar volume variations for a given excitation amplitude

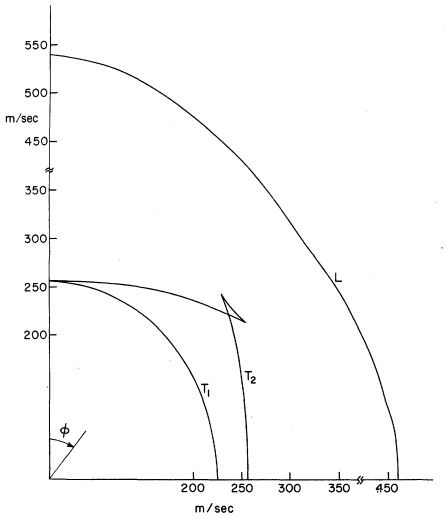

(b) Crepeau *et al.* [41] wave surface computation from the velocity surface measurements of the side figure. In order to efficiently focus an acoustic in hcp solid ^{4}He, one must design a piezo electric transducer whose shape matches the L-mode wave surface. Axes are given velocities but can be turned to lengths by multiplying both by the same arbitrary time.

Fig.II.4

Crepeau *et al.* have measured sound velocities in hcp solid ^{4}He crystals of known orientation[41]. From these measurements, they can deduce the surface velocities in hcp solid ^{4}He. The meaning of these surfaces is the following. Consider a hcp crystal with its c-axis in given direction. Because of the radial

symmetry of the hcp structure, the sound velocities are isotropic in the plane perpendicular to the c-axis. Let ϕ be the angle between the c-axis and the wave vector $\vec{k}$ of a plane wave excitation (see figure II.3b). Because of the anisotropy of the crystal, the *phase* velocity of the wave (that is the velocity of the sound pulse in the direction $\vec{k}$) depends on the angle ϕ. This dependence of the value of the phase velocity v on the angle ϕ is called the velocity surface of a mode of the acoustic wave. The results of Crepeau *et al.* for surface velocities measurements in hcp solid ^{4}He are shown on figure II.4a. From this velocity surface, the wave surface can be computed. The wave surface is the aspect of the wave front after an excitation from a point source. Musgrave gives relatively simple formulas for computing the wave surface from the velocity surface. Crepeau *et al.* have used these formulas to give the wave surface of elastic waves in hcp solid ^{4}He which is shown on figure II.4b.

So, in order to efficiently focus an acoustic wave in hcp solid ^{4}He, one must design a piezo electric transducer whose shape matches these wave surfaces. The quasi-longitudinal mode L is the mode we are interested in because it is the mode which gives the greatest variation of the density for a given displacement of the transducer[4].

The difficulty was actually to achieve a piezo electric transducer of this precise shape. This was not exactly an easy task...

II.1.3.1 Well shaped Piezo Electric Transducer

Indeed, the plan was initially to have it done by a piezo electric transducer manufacturer, namely Morgan ceramics at the time, now CeramTec. It turned out after almost one year of e-mail exchange with them that they were not able to produce the shape we asked at least for small quantities.

The shape of the desired emitter is sketched on figure II.5a.

It matches the L-mode wave surface of hcp solid helium shown on figure II.4b. Two details are important to note: (i) there is a 1 mm hole at the top of the transducer[2] and (ii) the lower 1 mm of the half wave surface was cut away in order that the origin (the acoustic focus) can be in direct view without being screened by the emitter rim. Hence the interferometric density measurement method discussed in chapter I can be applied.

Finally, the decision was taken by the team to have the transducer done in the mechanical workshop of the lab. In order to allow driving at high power, lead zirconate titanate ceramic (PZT) was chosen for the transducer material. We started from cylinders 20 mm in diameter and 20 mm in length. To machine ceramics, diamond tools and high-speed rotation are required. A standard CNC lathe from the mechanical workshop was used. The fixed cutting tool of the lathe

[2]this hole ensures that a mono-crystal can be grown around the all emitter without creating any liquid pocket in the inner volume of the transducer and also avoids any pressure gradient between the crystal inside and outside the transducer

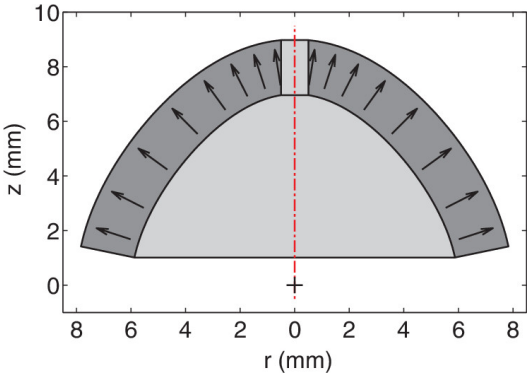

(a) Shape of the transducer profile shown as a radial cut. The inner surface of the transducer matches the wave surface of a hcp helium crystal whose c-axis is along the z direction. The local polarization axis of the transducer is represented by the black arrows.

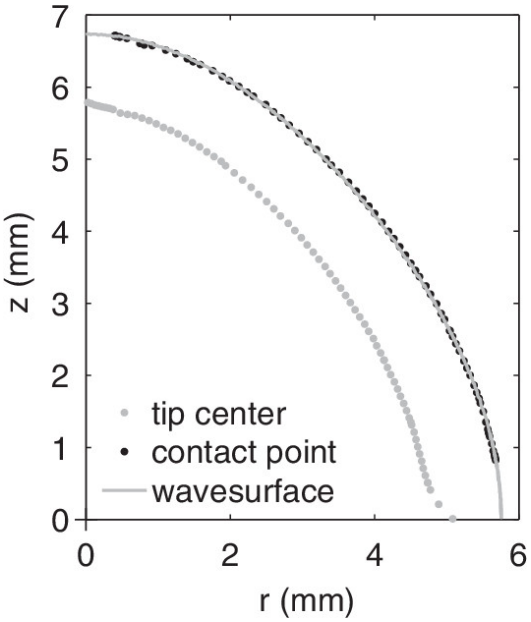

(b) Experimental profile measured using a dial test indicator compared with the designed one. The gray dots represent the trajectory of the ball tip center (ball radius 1 mm). The contact points with the inner surface deduced from them are represented by the black dots. The gray line is the fitted theoretical wave surface with $r(z = 0) = 5.83$ mm.

Fig.II.5

was replaced by pneumatic hand tool die grinder with speed tunable from 3000 to 17 000 rpm by changing air pressure from 0.25 to 4 bar. A series of grinding steps detailed in [42] has been realized to machine the transducer. Its shape has been checked using a dial test indicator mounted on a dual axis translation stage (see figure II.5b).

As seen in figure II.5b, the realization of the appropriately shaped transducer in our lab was a success[3]. It was of course very important for us for starting our experiment on metastable solid ^{4}He, but it was also important for other reasons.

Indeed, at the time we were realizing the transducer, they were a lot of discussions in the lab council (which I was part of) of how to integrate the technical agents (mechanics, electronics, management etc...) supporting the research to the output of the research work. Especially, the academic career evolution of technical agents suffers a lot from any clear visibility of their work. Researchers and technical agents agreed that a way to make things better was to try to

[3]The shaped transducer was then sent to Morgan Ceramics for heat treatment and poling.

publish research/technical papers in scientific journals with technical agents as authors. It turned out that the realization of a piezo electric device capable of focusing an acoustic in a hcp crystal had not been published so far. This was a nice opportunity to publish a scientific article of a collaboration of our team with Arnaud Lelcerc of the mechanical workshop, who actually machined the transducer and Jean Michel Isaac, the head of the mechanical workshop who discussed with us (mostly with mechanical talented Jacques Dupont-Roc) of the way to do it and Nabil Garroum of the engineering bureau, who simulated the electrical expected properties of the transducer. The paper with our names and their names was indeed published in Review of scientific instruments in 2014. This article is joined to the manuscript in the joined paper section.

II.2 Experimental results

Since the time we had succeeded in fabricating a piezo electric transducer with the appropriated shape, and when the interferometric technique for measuring density variation induced by the acoustic wave was developed, all the ingredients for producing metastable solid ^{4}He were available.

II.2.1 Crystal preparation

The only last remaining question was how to prepare the crystal so that (i) it is a mono-crystal, (ii) its c-axis is collinear to the transducer symmetry axis and (iii) it is initially at a pressure slightly above the melting pressure (point A of figure II.2). The two first conditions were assumed in the design of the transducer and the last one is to avoid surface melting as explained earlier (section II.1.2).

A sketch of the experimental cell is shown on figure II.12a where the PZT axis is fixed and vertical. In order to obtain acoustic focalization, the crystal in the cell must be oriented so that its c-facet is horizontal. A seed of hcp crystal is produced onto the so called "nucleator"[43]. This device is an electric capacitor which can generate locally an intense electric field of about 200 MV/m by applying a voltage difference of about 1 kV. Because of electrostriction, the local pressure in this area of intense electric field is slightly higher ($\sim$ 100 mbar) than anywhere else in the cell. When the static pressure inside the cell filled with liquid is just below the melting pressure, crystal appears at the surface of the nucleator as shown on figure II.12b.

Because of gravity, the seed will eventually fall down at the bottom of the cell hopefully with its c-axis collinear to the PZT axis. This crucial point is checked by imaging the crystal in two perpendicular directions. One direction of imaging is shown on figure II.6c. If the c-facet is not horizontal as it is the case on figure II.6c, the crystal is melt and a new seed is produced until the orientation of the c-facet is the desired one. When that's the case, the crystal is grown using a

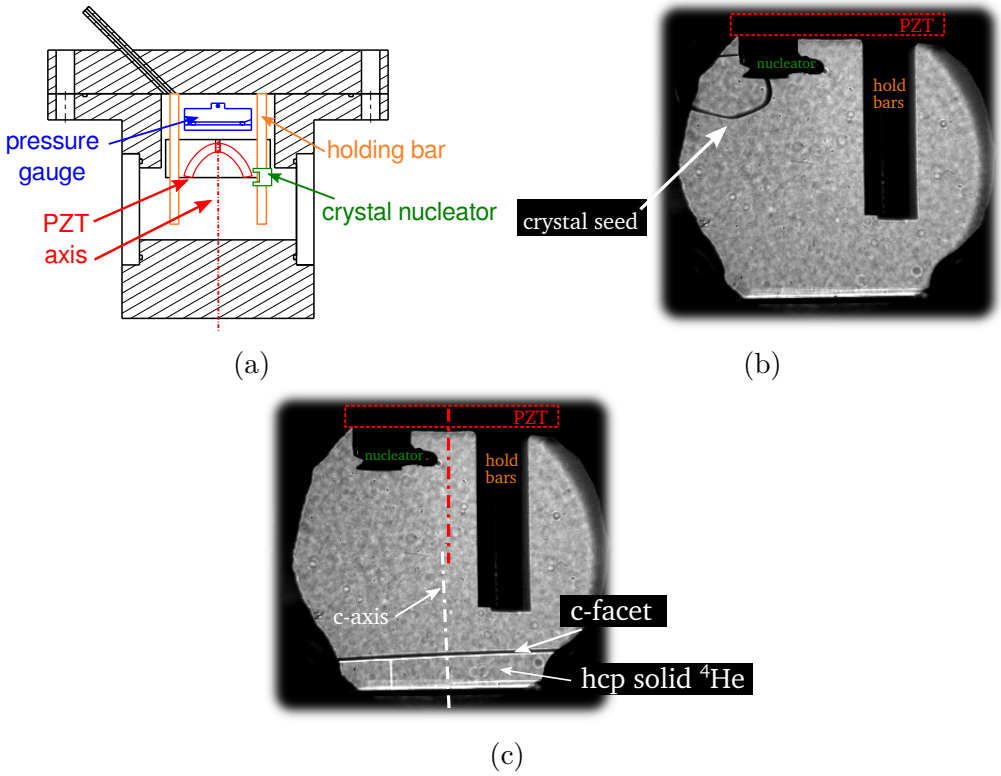

Fig.II.6: a) Sketch of the experimental cell. b) Nucleation of a crystal seed on the nucleator (see text). c) Optical check of the alignment between the PZT axis and the c-axis of the crystal. The crystal is not well oriented. A new one must be produced.

procedure I shall briefly describe now.

The aim is to obtain a single crystal filling the entire cell (meaning that the PZT is entirely immersed in the crystal) at a pressure above the melting pressure (point A(T_0, P_0) of figure II.2 and II.7). It must be mentioned that the orientation checking procedure discussed before must be done at temperature below the roughening temperature of the c-facet $T_{\texttt{rough}} = 1.3$ K. Indeed, above this temperature, the c-facet is not visible[44].

Filling the cell with the crystal and pressurizing it from point β to A at constant temperature T_0 would be harmful for crystal quality. Indeed, because helium is a very compressible solid, material would have to be brought into the cell including into the PZT cup. This would result in plastic deformation of the crystal, possibly breaking it into several differently oriented pieces. Pressure gradients could also be created. Instead we follow the procedure shown in Fig. II.7. The cell with the crystal seed in equilibrium with the liquid (point β of the figure where the orientation c-axis is checked) is warmed up along the coexistence line to point δ. There the meting pressure is greater than the melting pressure at T_0. This warming along the melting line is done slowly enough to keep a quasi-static

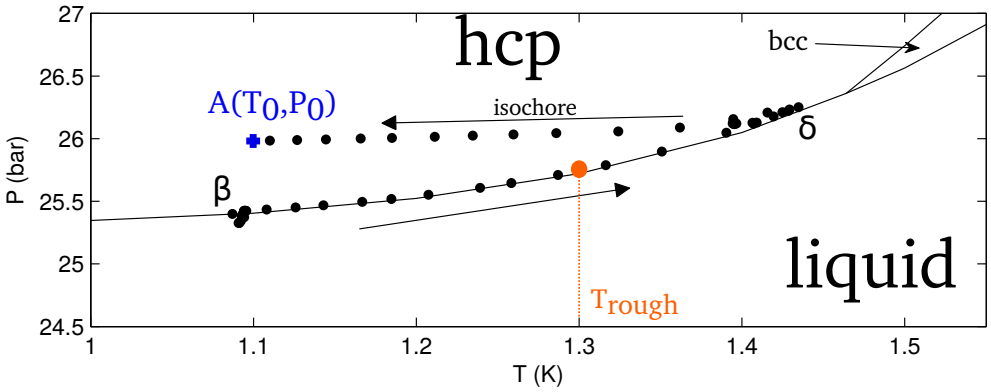

Fig.II.7: Experimental path in helium-4 phase diagram to obtain a crystal at point $A(T_0, P_0)$. β: nucleation of an oriented crystal seed. $\beta \rightarrow \delta$: warming of the crystal seed in equilibrium with the liquid up to $T_\delta \sim 1.4$ K. δ: growth of the crystal until the whole cell is filled. $\delta \rightarrow A$: isochoric cooling. Solid dots are experimental data provided by the cell thermometer and inner pressure gauge shown in figure II.12a

equilibrium between the pressure in the filling line and the melting pressure at the cell temperature. The crystal is then grown at point δ until the cell is filled and the filling capillary is blocked by the solid phase. Eventually, the whole cell is slowly cooled at constant volume down to (T_0, P_0) in a little more than two hours. This slow isochoric cooling is expected to avoid crystal breaking, as well as temperature and pressure gradients.

II.2.2 Metastable solid helium-4 does exist

From now on, the experiment on metastable hcp solid ^{4}He is ready to be run. A four-oscillation resonant RF pulse (frequency$\sim$ 1 MHz resonant with the thickness oscillation mode) is applied to the PZT and generates a convergent pressure wave train in the crystal. A movie of the propagation of the wave within the solid is taken using the local density measurements resolved in time technique described in the previous chapter I.2. I remind that the measured quantity is a map of optical phase shifts induced by the acoustic wave from which the local optical refractive index variations can be computed using an inverse Abel transform. Such phase and refractive index maps obtained in hcp solid ^{4}He at 1 K are shown on figure II.8. The refractive index map shows that indeed, the PZT design is satisfactory as the acoustic wave is correctly focusing.

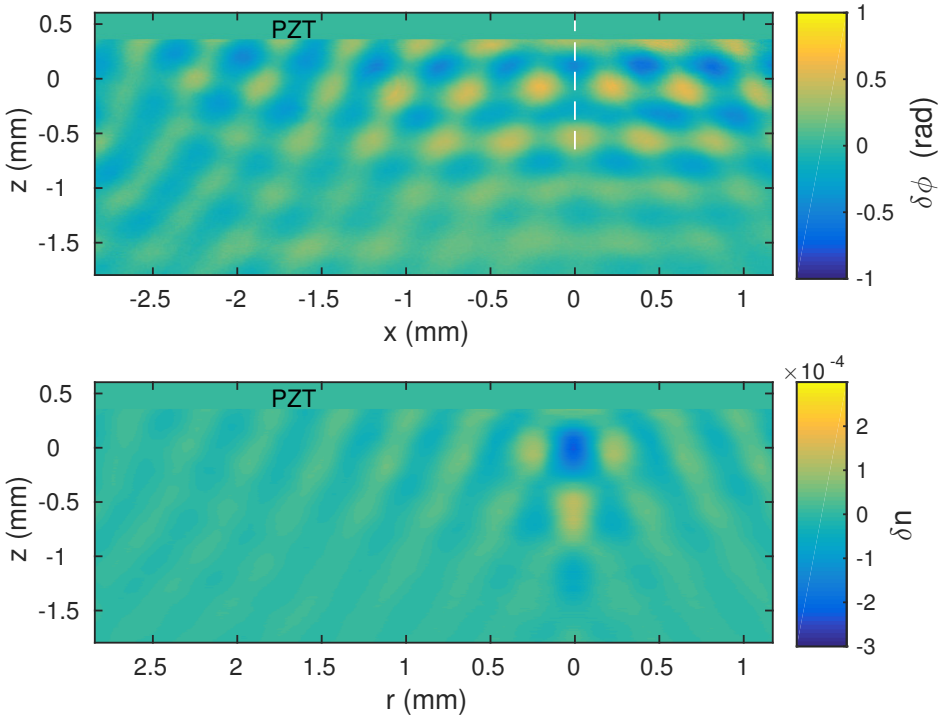

Fig.II.8: Experimental data showing an acoustic wave focused in solid ^{4}He at about 1 K recorded at a given time of propagation t_0. Top panel: instantaneous phase map $\delta\phi(x,z)$. Bottom panel: corresponding refractive index variations $\delta n(r,z)$ after computations of the inverse Abel transform. The shaped PZT satisfactorily focuses the acoustic wave.

Then, one can compute the time evolution of the local refractive index at acoustic focus as shown on figure II.9. On this graph, time $t = 0$ corresponds to the beginning of the electric excitation of the PZT. The time of flight of the density wave from the surface of the transducer to the acoustic focus is about 12.5 μs. On this peculiar example, the crystal was initially set at the point $A(T_0 = 1.13\text{ K}, P_0 = 26.36\text{ bar})$ and the melting pressure is $P_m(T_0) = 25.49$ bar.

Grilly [45] has measured that the quasi isotropic compressibility of hcp solid ^{4}He is relatively independent of pressure for pressures between 25 and 27 bar on the melting curve. In this domain, it varies less than 2% and the bulk modulus (inverse of the compressibility) is $\chi = 269$ bar. So, for solid helium in its stable phase between 25 and 27 bar, it is possible to translate density changes (and hence refractive index changes) into pressure variations.

Setting $\delta P_0 = P_m(T_0) - P_0$ (< 0), we have :

$$\delta P_0 = \chi \frac{\delta\rho_m}{\rho_0} = \chi \frac{\delta n_m}{n_0 - 1} \tag{II.2}$$

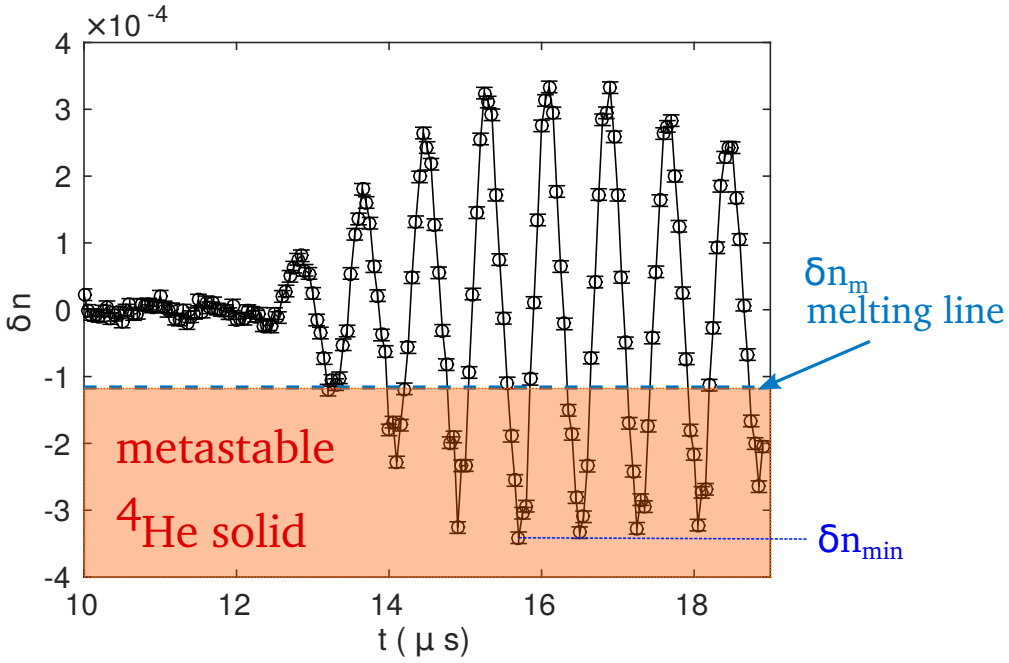

Fig.II.9: Time evolution of the refractive index variations at acoustic focus induced by a converging elastic wave in solid hcp ^{4}He at 1.1 K. The crystal is initially set at a pressure that corresponds to a density higher than that of the melting curve (point A of figure II.2). The corresponding optical refractive index variations between point A and the melting curve is given by δn_m (see text). During the negative swing of the acoustic wave, the local density is below the static melting line, meaning that hcp solid ^{4}He is in a metastable state. δn_{min} is the maximum of the negative refractive index variations whose value depends on the driving voltage of the piezo transducer.

where $\delta\rho_m$ is the density variation between the density in $A(T_0, P_0)$ and the point $(T_0, P_m(T_0))$ on the melting curve so that δn_m is the optical refractive index variation needed to reach the melting line point $(T_0, P_m(T_0))$ starting from point $A(T_0, P_0)$.

Hence δn_m is easily calculated from P_0, $P_m(T_0)$ and $n_0 = 1.036$ the static optical refractive index[46] of hcp solid solid ^{4}He and can be represented on figure II.9.

This figure summarizes one of the most important results of the PhD of Fabien Souris. It shows that indeed, during the negative swing of the acoustic wave, the local density is clearly below the static melting line, that is that we have indeed produced and observed metastable hcp solid ^{4}He.

From this graph, one can also compute the incursion in the metastable domain in term of molar volume. As it can be seen on the figure, the maximum variation of δ_n obtained on this peculiar set of data is about $-3 \cdot 10^{-4}$ so that $\frac{\delta_n}{n_0 - 1} \sim$

$-1 \cdot 10^{-2}$.

Hence, the initial molar volume of the sample $\sim$ 21 cm^3/mol has been increased by 1 %. To reach the aimed value of 22 cm^3/mol, a five times longer excursion would be necessary. When increasing the variation of the molar volume simply by increasing the acoustic excitation, we encountered an unexpected instability.

II.2.3 Unexpected instability

When the driving voltage V_{PZT} of the PZT exceeds a threshold value, it was observed that crystal breaks in the vicinity of acoustic focus. An extended defect with a different density appears near the focal point. Such a defect is shown on figure II.10 which are raw interferometric images.

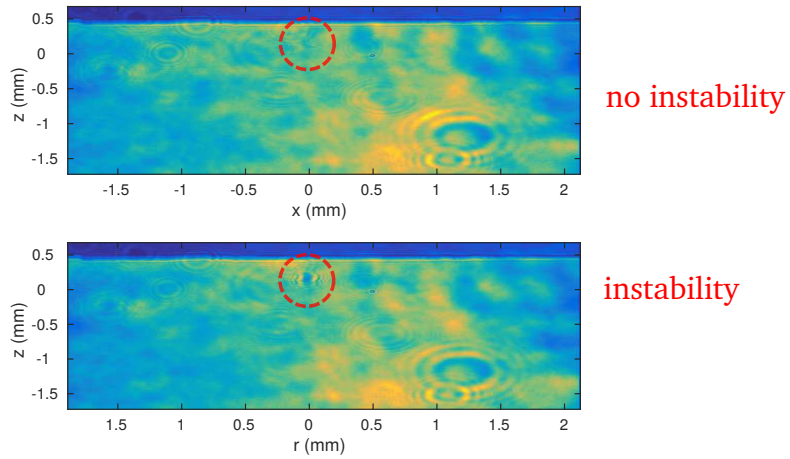

Fig.II.10: When the driving voltage of the piezo electric transducer is increased above a certain value, an unexpected instability appears as an extended defect with a different density near the acoustic focal point as shown in the bottom panel (raw interferometric image). The top panel is a raw interferometric image of the acoustic focal point without any defect.

Once defects are created in the crystal, they disappear in a few seconds after the sound pulse. However, subsequent sound pulses damage the crystal beginning from the initial defect, up to a point where the acoustic propagation is completely perturbed.

If one wants to estimate the pressure at which this instability occurs, one can assume for a while that equation (II.2) holds in the metastable domain. Slightly depending on the experiment and on the temperature, we found that the pressure at which the instability occurs lies between 3 and 4 bar below the melting line. Maris has proposed a EOS of metastable solid ^{4}He [47] in which he proposed that the stability limit of a perfect hcp solid ^{4}He crystal should lie at absolute

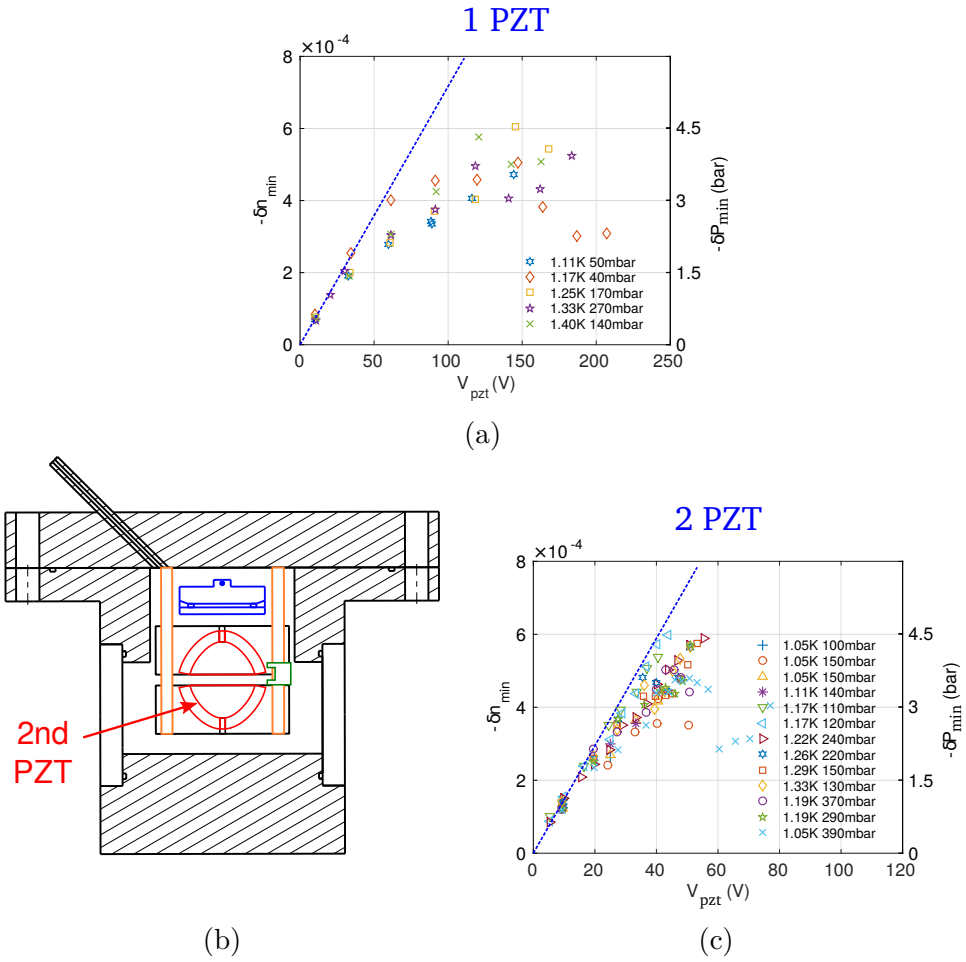

Fig.II.11: a) Measurement of the maximal optical refractive index variations at acoustic focus ($-\delta_{min}$ see figureII.9) as a function of the driving voltage V_{PZT} in the case where the acoustic wave is created by a single PZT. b) Sketch of the experimental cell containing 2 confocal PZT's. c) Same as a) in the case of an acoustic wave created by 2 PZT's.

pressure of -10 bar, that is 35 bar below the melting line. Numerical simulations by Pollet et *al.* claimed that the gap between the energy cost of vacancy and interstitial creations should close and destabilize the solid at pressure around 0 bar, that is 25 bar below the melting line. Clearly, our pressure extrapolation of the instability is not in agreement with these numbers.

When one looks at the maximum of the negative refractive index variations $-\delta n_{min}$ as a function of the driving voltage V_{PZT}, one realizes that they don't scale linearly with V_{PZT} as shown on figure II.11a. On this figure, no data points are seen for $-\delta_{n_{min}} > 6 \cdot 10^{-4}$. This is precisely the region where the instability appears and the destruction of the crystal prevents any refractive index measurements. We wondered then if these non linearities in the sound

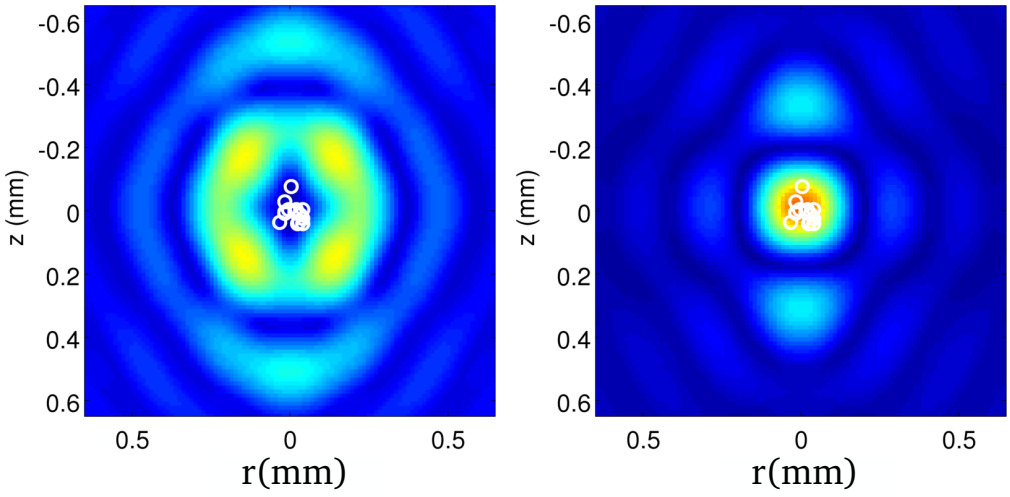

(a) (b)

Fig.II.12: a) Simulated map of maximum shear constrains induced by the acoustic wave created by the 2 confocal PZT configuration. b) Simulated map of maximum molar volume variations created by the 2 confocal PZT configuration. In both cases, white circles are the measured locations of the instabilities in the 2 PZT's case.

propagation were linked to the apparition of the instability. The experimental way we found to address this question was to improve the symmetry of the sound wave in putting a second transducer facing the first in such a way that their foci coincide. Hence a given $\delta_{n_{min}}$ can be achieved with weaker V_{PZT}. A diagram of the cell with two PZT's is given on figure II.11b. The results of experiments with 2 facing PZT's are presented on II.11c. Indeed, the non linearities are reduced but the crystal destabilizes in the same range of optical index variations ($\sim -6 \cdot 10^{-4}$). The conclusion is then that the destabilization threshold we observe is not linked to the non linearities of the sound propagation in solid ^{4}He but probably to some more intrinsic property of solid ^{4}He.

During his PhD, Fabien Souris has done a remarkable work on simulating the propagation of the sound wave in the crystal[4]. From these simulations, he was able to compute maps of maximum shear constrains and of maximum molar volume variations. We can draw on these simulated maps the measured coordinates of the initial defect of the instabilities. The results of this study in the case of two facing PZT's is shown on figure II.12.

One can clearly see that the location of the initial defect corresponds to the acoustic focus where the density variations are important and shear constrains vanish. The conclusion is that this instability is density induced and can be linked to some limits of the metastability which solid ^{4}He can eventually reach.

II.2.3.1 Time of birth of the instability

It remained however experimentally unproven that the instability started temporally in the metastable domain, that is in the negative swings of the acoustic wave. This important information was not obtainable with the interferometric set-up of figure I.4 used to measure the density variations. Indeed, this set-up is based on CCD of 10 Hz bandwidth. The movie of the acoustic wave is resolved at the 50 ns scale because each image corresponds to different sound pulses sent into the crystal with an adjustable delay between the sound excitation and pulsed the imaging laser. To resolve in time at a microsecond scale the apparition of the instability within a single sound pulse, we have implemented a standard Schlieren imaging technique. This experiment was the transition experiment between the end of Fabien Souris' PhD and the beginning of Qu An's one.

Unlike the 10 Hz pulse laser used for interferometry, here we use a continuous quasi-parallel light beam that illuminates the region where the instability will occur. The set-up is sketched on figure II.13.

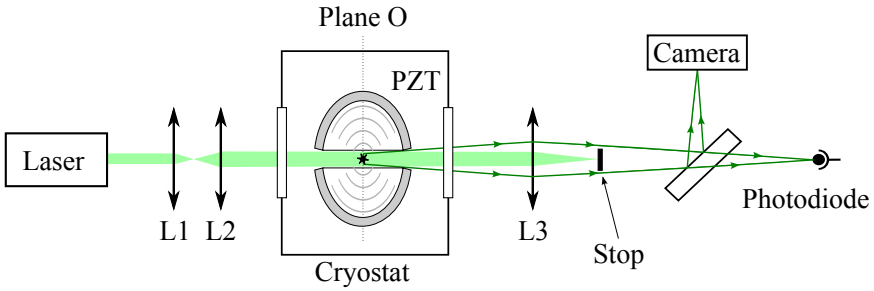

Fig.II.13: Experimental arrangement to monitor the light scattered by the damaged region (plane O) at a microsecond time scale. The beam of a CW laser, expanded by two lenses (L_1 and L_2), illuminates the region where the instability occurs. The unscattered light is focused by L_3 and absorbed by a beam stop, while the light scattered by the damage is collected by a fast photodiode. Using a semi-transparent plate, images of plane O can be simultaneously recorded on a standard CCD camera.

The detector of the present experiment is a fast photodiode ($\sim$ 5 MHz bandwidth). This photodiode is placed at the image plane of the acoustic focus through a corrected lens assembly. This lens focuses the unscattered light onto an opaque beam stop ensuring that it is blocked. On the contrary, the light scattered by the damage is detected.

A semi-transparent plate allows us to get simultaneously an image of the region of interest on a CCD camera. The experimental protocol is the following. First, a single crystal is nucleated and grown to fill the cell according to the technique described earlier (II.2.1) so that the piezo-emitters (PZT) are completely immersed in it. The crystal quality is controlled by checking the sound focusing using the pulsed interferometric method. This is done at a low enough driving

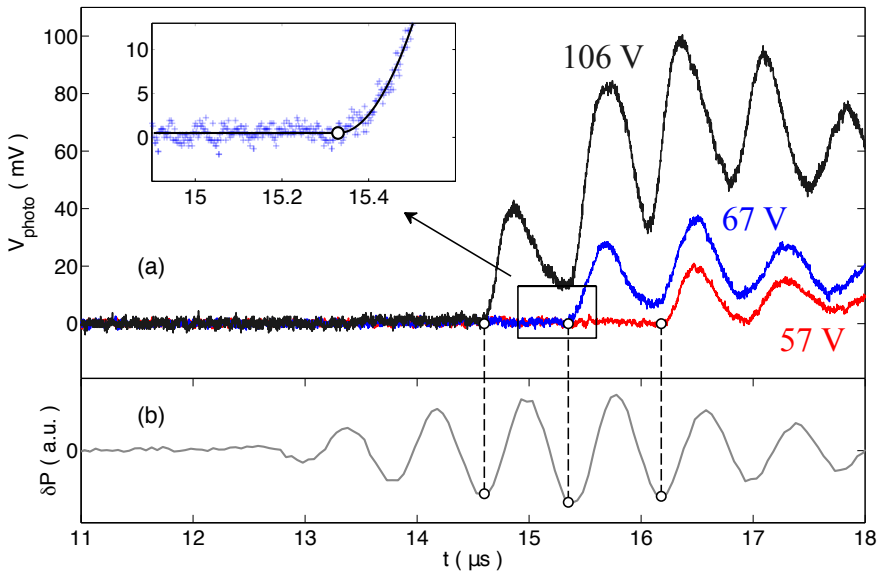

Fig.II.14: a) Photodiode voltage as function of time for 3 experiments creating solid ^{4}He instabilities at different PZT driving voltages. The sharp increase of the signal corresponds to the appearance of the instability. The open circles give the time of birth t_0. Inset: closer look at the creation time of the instability. b) Pressure variations at acoustic focus in arbitrary units for temporal reference.

voltage ($V_{PZT} \sim 40$ V) that the crystal remains undamaged. Typical maximal depressions achieved are 2 bar below the melting line. The position of the acoustic focus is then determined on the interferometric images. The CW laser beam used in the Schlieren imaging measurement is centered on the acoustic focus.

The photodiode output is recorded on a digital oscilloscope, triggered at $t = 0$ by the beginning of the radio frequency excitation. Figure II.14 displays several signal examples corresponding to different driving voltages of the PZT. A sharp increase of the scattered light signals the damage occurrence at t_0. The low panel of the figure is the recording of the optical index variations at acoustic focus performed with the interferometric method at low driving voltage V_{PZT}. The same trigger is used for this interferometric recording ($t = 0$ by the beginning of the radio frequency excitation) so that time scale of the top panel (schlieren with CW laser) is the same as the one of the bottom panel (instantaneous pressure at acoustic focus).

These measurements clearly show that the instabilities are always created on a depression swing of the sound wave, that is when the solid is exploring the metastable domain. This result gives strong support to the hypothesis that this instability corresponds to the nucleation of a 'bubble'of another phase, presumably the liquid one, inside the bulk of solid helium. It should also be noticed that as the driving voltage is increased, the time of creation of the instability

jumps from one negative swing to an earlier one. It is tempting to attribute this behavior to the existence of a pressure threshold triggering the instability: this threshold would be reached earlier in the acoustic wave as the wave amplitude is increased. However, for the seven experiments performed at the lowest driving voltage ($V_{PZT} = 57$ V), the instability systematically starts during the oscillation *after* the one of minimum pressure. If a threshold did exist, the 57 V instabilities would have nucleated at least one oscillation before the one observed. Even if we assume that there is only some probability of breaking during a certain swing, as soon as the amplitude is large enough, this result doesn't seem compatible with a simple threshold. Indeed, the two preceding oscillations have amplitudes equal or larger than the one where events are observed. Attributing equal probabilities for a nucleation event in each of these oscillations, the probability for 7 events lying in the last oscillation would be only $(1/3)^7 \simeq 4 \cdot 10^{-4}$. This suggests that fatigue effects could play a role in triggering the instability.

II.2.4 Discussion

Our team has succeeded in producing and observing metastable hcp solid ^{4}He. Figure II.15 is a summary of our experimental results concerning the destabilization of metastable solid helium.

The color circles represent the starting point of each acoustic experiment (point A of figure II.2). The bar with the same color in the metastable domain is an interval of the estimated pressure value at which the instability occurs. It can be seen on this figure that the destabilization pressure does not really depend on temperature between 1 and 1.4 K. This suggests that the important parameters to trigger this instability are pressure or density rather than temperature. However, this conclusion is based on pressure estimate assuming a constant bulk modulus of solid ^{4}He, and hence a linear dependence between density variations (optical refractive index variations) and pressure variations. Although this assumption is well justified for the stable solid between 25 and 27 bar, it could be really different in the metastable domain. A measurement of the equation of state in the metastable domain will help in understanding this instability. If, for instance, proliferation of vacancies is involved in triggering the instability, the compressibility of the solid should increase while approaching this instability. On the other hand, there is a priori no reason why the compressibility should be particularly affected if the instability is due to fatigue effects. It appears then that probing the compressibility of solid ^{4}He in the metastable domain is an important experiment to perform in order to better understand the unexpected instability reported here.

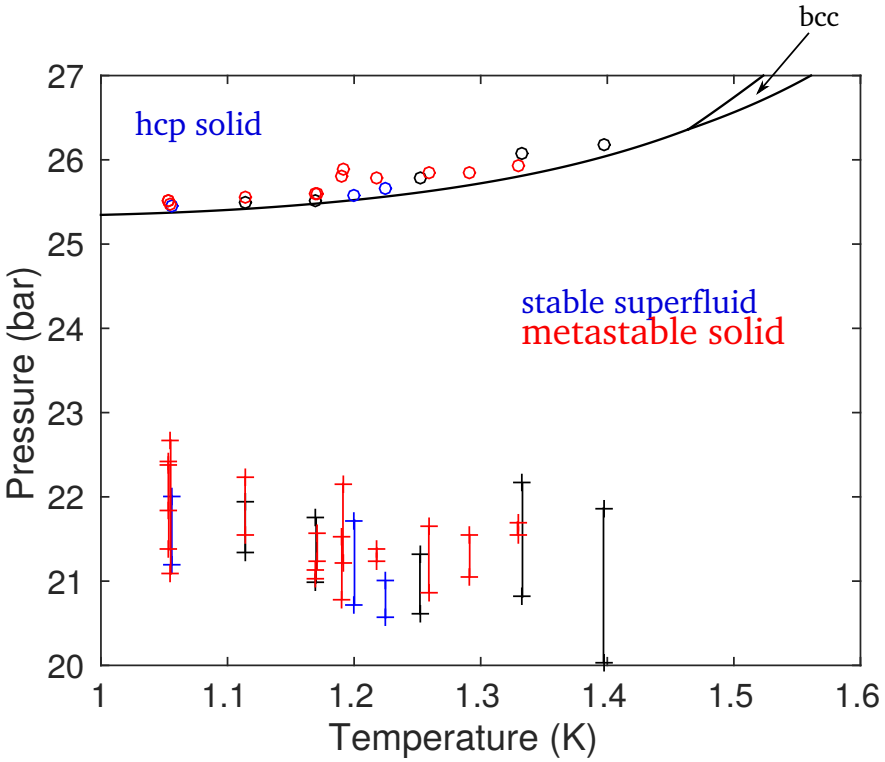

Fig.II.15: Phase diagram of ^{4}He summarizing our experimental results concerning the destabilization of metastable solid helium. The color circles represent the starting point of each acoustic experiment (point A of figure II.2) and the color corresponding bar in the metastable domain is an interval of the estimated pressure value at which the instability occurs.

Chapter III

Research project : equation of state of ^{4}He in metastable liquid or solid phases

III.1 Motivations

As explained in the two preceding chapters, our experiment enables us to create metastable states of liquid and solid ^{4}He using converging acoustic waves. The quantity we measure is the local density of the sample within the acoustic wave. We have seen that for sufficiently large acoustic excitation, both the metastable liquid and the metastable solid phases become unstable. The pressures at which these destabilizations occur are not directly measured. For that purpose, an equation of state (EOS) is needed. My research project is to set up an experiment to measure experimentally the equation of state of ^{4}He in metastable liquid or solid phases.

In the case of the destabilization of metastable liquid ^{4}He at 1 K, we have seen that our direct measurement of the cavitation density does not agree with previous estimates of the cavitation pressure if the conversion is made using a

theoretical EOS of the metastable phase. It is therefore important to check the validity of this calculated EOS experimentally.

In the case of metastable solid ^{4}He, we have seen that an unexpected instability is observed. It would be interesting to look if this instability is linked to an anomaly of the EOS of the metastable phase.

A way to determine experimentally the EOS is to measure simultaneously the density and the speed of sound c_s (at least for isotropic phases[1]). Indeed, the later one is given by :

$$c_s^2 = \left(\frac{\partial P}{\partial \rho}\right)_S \tag{III.1}$$

where P is the pressure, ρ the density and S the entropy. This equation tells us that measuring the speed of the sound of the medium gives a measurement of the slope of the $P(\rho)$ function. Hence, measuring the sound velocity as a function of the density gives the EOS by integration of equation (III.1). EOS of metastable states of water at negative pressures have been measured doing such speed of sound measurement[48].

III.2 Principle of the experiment

The difficulty in measuring the sound velocity in the metastable state is that the metastable region is narrow both in space and time. Indeed, the typical size of acoustic focus is about 200 μm and the time spent in the metastable domain is less than 500 ns. To fulfill these requirements, I plan to use stimulated Brillouin scattering of an intense laser beam precisely focused on the acoustic focus. Indeed, a pulsed width of about 10 ns ensures that the metastable state is well selected in time and focusing the laser on a waist of about 10 μm ensures the spatial selection (see figure III.1a).

III.2.1 Stimulated Brillouin Scattering

The basic idea of SBS is illustrated on figure III.1. When an intense laser $(\vec{E}_1, \omega_1)$ is focused into a transparent medium, it can create an acoustic grating (phonons at frequency Ω_B propagating at the local velocity of sound c_s of the medium) on which the incident laser can reflected in the backward direction $(\vec{E}_2, \omega_2)$. The reflected light is Doppler shifted and is at the frequency $\omega_2 = \omega_1 - \Omega_B$.

Assuming for now (we shall briefly justify this point later) that a phonon of wavevector $\vec{q}_B$ is created by the initial photon of wave vector $\vec{k}_1$, momentum conservation implies that:

[1] for hcp solid phase, the sound velocity should be measured parallel and perpendicular to the c-axis

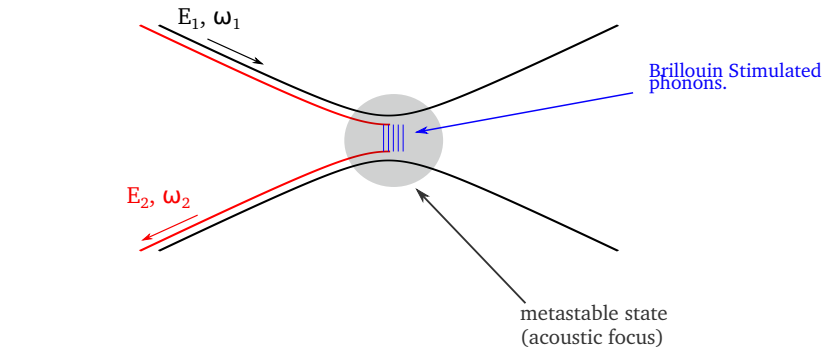

(a)

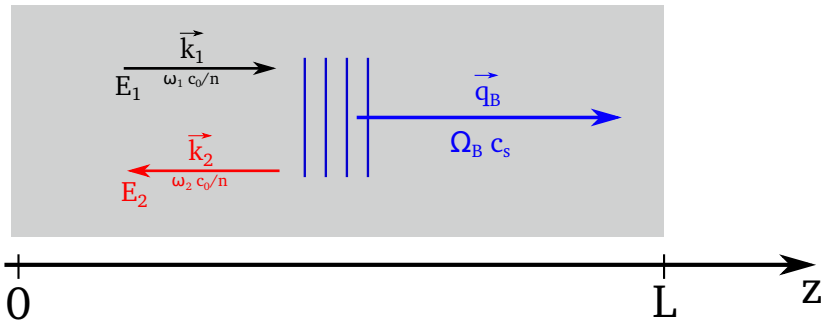

(b)

Fig.III.1: Stimulated Brillouin Scattering for local sound velocity measurements. a) An intense laser is focused on a size smaller than the acoustic focus creating metastable states of liquid or solid helium-4. The creation of stimulated acoustic phonons will be localized around optical focus hence a local measurement of the sound velocity is possible by measuring the frequency shift between the excitation laser E_1 and the reflected field E_2. b) Zoom around optical focus where the excitation laser, the induced acoustic phonons and the reflected field are to be considered as plane waves.

$$\vec{q}_B = \vec{k}_1 - \vec{k}_2 \approx 2\vec{k}_1 \tag{III.2}$$

where $\vec{k}_2$ is the wavevector of the reflected field. The dispersion relation of the acoustic phonon being $\Omega = c_S q_B$ and the one for the photons being $\omega = c_0 k/n$ with n the local optical refractive index of the medium and c_0 the speed of light in vacuum, equation (III.2) leads to

$$c_s = \frac{\omega_1 - \omega_2}{2\omega_1}\frac{c_0}{n} \tag{III.3}$$

If one is able to measure $\omega_1 - \omega_2$, one can deduce the value of c_s provided that ω_1 and n are known. My research project is based on eq. (III.3). To measure c_s one needs the refractive index index in the metastable region which is measured

by our optical interferometric setup and the frequency $\omega_1 - \omega_2$ which can be obtained by making the fields $\vec{E}_1$ and $\vec{E}_2$ beat on a fast enough photodiode.

As we will see, SBS is a non linear process involving an intensity threshold which we shall try to estimate for liquid and solid ^{4}He.

The physical mechanism behind SBS is electrostriction. In his book about nonlinear optics [49], Boyd defines electrostriction as being "the tendency of materials to become compressed in the presence of an electric field." The following equations actually come from this book and the Boyd treatment of SBS. Taking the notations of figure III.1b, Boyd shows by considering the propagation of an acoustic wave in the medium submitted to an electrostrictive pressure due the laser fields that the following equations must be fulfilled:

$$\frac{\mathrm{d}I_1}{\mathrm{d}z} = -gI_1I_2$$
$$\frac{\mathrm{d}I_2}{\mathrm{d}z} = -gI_1I_2$$

where I_1 and I_2 are the intensities of the light beams expressed in W/m^2 and g is the so called SBS gain factor expressed in m/W. The later one is given by:

$$g = g_0 \frac{(\Gamma_B/2)^2}{(\Omega_B - \Omega)^2 + (\Gamma_B/2)^2}$$

where Ω is the phonon frequency, $\Omega_B = \omega_1 - \omega_2$ is called the Brillouin frequency and Γ_B its line width due to the finite lifetime of the phonons ($\Gamma_B = \dfrac{1}{2\tau_p}$ if τ_p is the phonon lifetime).

The central line gain factor g_0 is given by the expression :

$$g_0 = \frac{\gamma_e^2 \omega_1^2}{n c_s c_0^3 \rho \Gamma_B}$$

where $\gamma_e = \rho \left(\dfrac{\partial \epsilon_r}{\partial \rho} \right)$ is the electrostriction constant which links the variations of the relative permittivity ϵ_r to the variations of the density ρ.

In the case of constant pump intensity (I_1=constant), equations III.2.1 are easy to solve and one finds $I_2(z) = I_2(L) \exp\left(gI_1(L-z)\right)$ and we see that I_2 which is propagating towards the $z < 0$ direction is growing exponentially. More clearly perhaps, an initial light field initially present at position $z = L$ will end up at $z = 0$ with an intensity $I_2(0) = I_2(L) \exp\left(gI_1L\right)$ while propagating over a SBS active length of size L. In fact, I_1 can not be constant and equations III.2.1 must be solved simultaneously. The most important feature of the solution of these coupled equations is that there is an intensity threshold for SBS. The reflectivity $R = I_2(0)/I_1(0)$ is plot as a function of $I_1(0)$ on figure III.2.

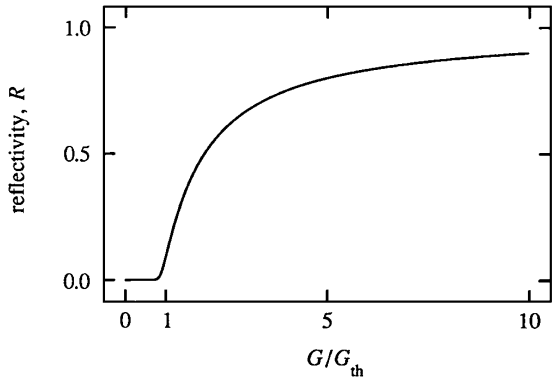

Fig.III.2: Threshold intensity in SBS. The curve is taken from the book of Boyd [49]. The parameter G is given by $G = gI_1(0)L$. G_{th} is the threshold value for triggering SBS and defines the threshold intensity if we set $G_{th} = gI_{th}L$. $R = I_2(0)/I_1(0)$ is the SBS reflectivity

Finally and most importantly for us, it can be shown that if SBS is initiated by a laser pulse of duration t (which can be short compared to the phonon lifetime $\frac{1}{\Gamma_B}$), the threshold intensity (at resonance $\Omega = \Omega_B$) for SBS is given by :

$$g_0 I_{th} L = \begin{cases} (G_{th}/2 + \Gamma_B t)^2/2\Gamma_B t & \text{if } \Gamma_B t < 12.5. \\ G_{th} & \text{if } \Gamma_B t > 12.5. \end{cases}$$

where G_{th} is a dimensionless number. The upper relation is known as the threshold condition for transient SBS and the lower relation is the threshold condition for the permanent SBS regime.

I shall now give numbers in order to estimate the SBS threshold in the case of liquid helium-4 at 1 K. First of all, the frequency of the phonons involved in the SBS process $f_B = \Omega_B/2\pi$ is given by $\Omega_B = c_S q_B/ = 2c_s k_1$ where we have assumed that $k_1 = k_2$. Taking the value $c_s = 238$ m/s[50] and an infra red excitation laser $\lambda_1 = 1064$ nm, we find that $f_B \sim 0.6$ GHz phonons are excited. 0.7 GHz phonon lifetime in liquid helium-4 at 1 K has been measured by Leiderer to be about $\Gamma^{-1}_{Leiderer}$ =50 ns[51]. Actually, this measurement was done by triggering SBS in liquid ^{4}He using a ruby laser ($\lambda_r = 694$ nm). According to Boyd, the Brillouin linewidth Γ_B is proportional to ω_1^2. Phonons in liquid helium-4 excited at $\lambda_1 = 1064$ nm are then expected to have a Brillouin linewidth of $\Gamma_B = (694/1064)^2 \times \Gamma_{Leiderer} \sim 8.5$ MHz. With that number, we find that for a typical Q-switch laser of about $t = 10$ ns, $\Gamma_B t \sim 0.1$ and that the transient expression for the SBS threshold intensity must be used.

To estimate the gain factor $g_0 = \dfrac{\gamma_e^2 \omega_1^2}{n c_s c_0^3 \rho \Gamma_B}$, one needs the electrostriction constant $\gamma_e = \rho \left(\dfrac{\partial \epsilon_r}{\partial \rho} \right)$. As $\epsilon_r = n^2$, we get $\gamma_e = \rho \left(\dfrac{\partial n^2}{\partial \rho} \right)$. In the limit $n \sim 1$

which is certainly a good approximation in the case of helium-4 (liquid solid or gas), the Lorentz-Lorenz relation might be written $n^2 = 1 + \frac{4\pi N_0 \alpha}{M}\rho$ with α being the polarizability per atom, $N_0\alpha$ the polarizability per mole and ρ the density of the liquid.

Hence

$$\gamma_e = \rho\left(\frac{\partial n^2}{\partial \rho}\right) = \frac{4\pi N_0 \alpha}{M}\rho$$

which we can estimate. $N_0\alpha = 0.1246$ cm^3/mole [46], $\rho = 0.145$ g/cm^3[50] and $M = 4$ g/mole. We find that $\gamma_e = 0.057$ and that the SBS gain factor for liquid helium-4 at 1 K is about:

$$g_0 = 1.3 \text{ m/GW}$$

for an excitation laser wavelength of $\lambda_1 = 1064$ nm.

To estimate the value of G_{th}, we proceed as follows. In a paper written in 1990[52], Boyd shows that G_{th} is given by solving the equation $R_{th}G_{th}^{3/2} = Y(\omega_1)g_0\frac{T}{c_s}e^{G_{th}}$ where $R_{th} = 1$ % is the arbitrary definition of the value of the reflectivity at the threshold, T the temperature of the sample, c_s the sound velocity and Y a function which depends on the laser frequency ω_1. For SBS in CS_2 (carbon disulfide) at room temperature ($T = 300$ K, $c_s \sim 1200$ m/s) using $\lambda_1 = 1064$ nm light ($g_0 = 1.5$ m/GW), he founds that G_{th} is about 24. Using this number and computing G_{th} for liquid helium ($T = 1$ K, $c_s \sim 240$ m/s, $g_0 = 1.3$ m/GW), one finds G_{th} is about 28.

Now, if the excitation laser is gaussian, the optical power at optical focus (within the Rayleigh range) is $P_{th} = I_{th}/(\pi w_0^2)$ where w_0 is the optical waist. Assuming that the interaction length L for generating SBS is twice the Rayleigh range $L = 2z_R = 2\frac{\pi w_0^2}{\lambda_1}$, the transient condition for the SBS threshold is given in terms of optical power by $P_{th} = \dfrac{\lambda_1}{2g_0}(G_{th}/2 + \Gamma_B T)^2/2\Gamma_B T$. Pulsed lasers are usually characterized by the time width of the pulse t and the energy of the pulse $E_{th} = P_{th}t$. We finally find that relation for the SBS energy threshold must be given by:

$$E_{th} = \frac{\lambda_1}{4g_0\Gamma_B}(G_{th}/2 + \Gamma_B t)^2 \tag{III.4}$$

This function is plotted in figure III.3a with the values $\lambda_1 = 1064$ nm, $g_0 = 1.3$ m/GW, $G_{th} = 28$ and $\Gamma_B = 8.5$ MHz. As it can be seen on this graph, for t between 2 ns and 30 ns (typical time width of Q-switch laser), E_{th} is relatively independent of t and is about 5 mJ.

It is interesting for us to have the biggest possible pulse length. Indeed, as we plan to measure optical beating in the GHz range, the more beatings we have the best the signal to noise ratio will be.

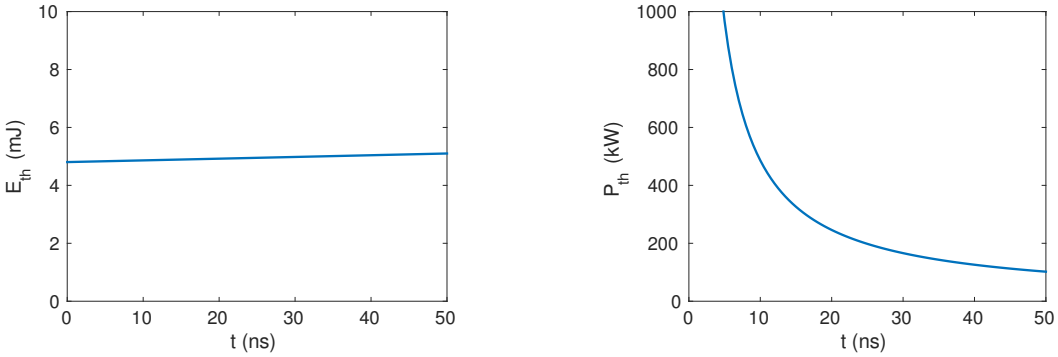

(a) (b)

Fig.III.3: a) The energy threshold estimation for SBS in liquid helium-4 as given by equation (III.4) as a function of the laser pulse duration t for $\lambda_1 = 1064$ nm. b) The corresponding power threshold.

III.2.2 Previous experimental results by other groups

SBS in liquid and solid helium-4 was an active topic in the late 60's. To my knowledge, the first experiment is due to Winterling *et al.* in 1968[53]. They made the first demonstration that SBS can occur in liquid helium-4 and were able to measure sound velocities in the liquid by measuring the Brillouin shift using a Fabry Perot interferometer. They also say in that paper that the threshold power for SBS in liquid helium-4 is comparable to that of quartz at the same temperature. If one refers to the numbers given for quartz by the same authors at 5 K[54], the power threshold for liquid helium using a ruby laser ($\lambda_r = 694$ nm) of duration 15 ns is about 3.2 MW, that is a pulse energy of about 45 mJ. This is much bigger than 5 mJ of figure III.3a. A possible and likely explanation for this discrepancy is that the estimated energy relation III.4 is done for a perfect Gaussian beam, namely with a so called propagation factor $M^2 = 1$. If the laser is not ideally gaussian, then $M^2 \neq 1$ and the propagation factor can affect the energy threshold. Paul Leiderer's group has also achieved SBS in both liquid and solid helium-4 [51] using also a ruby laser. They used a two laser configuration to measure the lifetime of 0.7 GHz SBS-induced acoustic phonons in both liquid and solid helium-4. No power threshold for SBS stimulation is indicated in their papers. Finally, Abrikosova and Skrypnik from Moscow university also observed SBS in liquid helium-4 in 1967 [55] but also no number is given for the power threshold. In this paper is also mentioned the observation of laser induced optical breakdown in liquid helium-4. Since these different works of the late 60's, I didn't find any attempts of generating SBS in liquid or solid helium-4 in the literature. However, these different papers clearly show that it is possible to achieve Stimulated Brillouin Scattering in condensed helium-4.

III.3 Working plan and preliminary tests

III.3.1 Working plan

We will start with liquid ^{4}He. I will in the following part name the acoustic wave creating the metastable states of solid or liquid helium the "The PZT acoustic wave". This wave has nothing to do with the Brillouin stimulated phonons.

The working plan is the following:

1. Get a SBS signal in stable liquid ^{4}He (No PZT acoustic wave).

   As I shall expose in the preliminary results section, this point is not so simple. However the results of the late 60's show that it is indeed possible to generate SBS in liquid helium.

2. Measurement of the beating signal $\omega_1 - \omega_2$ and determination of the sound velocity using equation (III.3) in the stable liquid (No PZT acoustic wave).

   This measurement will be done at different temperatures and pressures of the stable liquid where the sound velocity is accurately known and tabulated[50].

3. Sound velocity measurement in the positive swings of the acoustic focused wave (PZT acoustic wave On).

   This step will be the starting point of the measurement of the sound velocity in the metastable domain. But, before attempting at measuring an unknown equation of state, we will first check one which is known, in order to validate our experimental procedure. Indeed, at the PZT focus, the density of helium is modulated as shown for instance on figure II.9 for the solid case. During the negative swings of the PZT wave the sample explores its metastable state, but during the positive swings the sample explores its stable state but simply at higher density. We will then measure the sound velocity in the high density state and check if our measurement fits with the known values of the density dependent velocity of sound in the stable state[2]. A real difficulty here will be to precisely align the optical focus and the PZT acoustic focus.

4. Sound velocity measurement in the negative swings of the acoustic focused wave (PZT acoustic wave On).

[2]In the case of liquid helium, the maximal positive swing of refractive index shown in figureI.8b of chapter I of about $\delta_{n_{max}} = +4 \cdot 10^{-3}$. This corresponds to relative density variation of $\delta\rho_{max}/\rho_0$ of about 15% resulting in a change of the sound velocity of about 40% between this high density state and the corresponding static state.

This will be the real experiment which will only consist in accumulating data as from an experimental point of view, there are a priori no supplementary difficulties compared to the previous point.

Then following the same procedure will give access to the equation of state of the metastable solid.

III.3.2 Preliminary tests

In fact, phase 1 of the project has started. I have tried to trigger SBS in liquid helium-4 using a laser we bought from the Lithuanian company Ekspla with the following specifications: $\lambda_1 = 1064$ nm, $t = 25$ ns and $E_{max} = 60$ mJ. The manufacturer has also ensured us that the laser should be single longitudinal mode with a linewidth of about 0.003 cm^{-1}.

The set up used is shown on figure III.4 a). The Ekspla laser was focused in the middle of the experimental cell from outside the optical cryostat using an optical arrangement made of a diverging (focal length f_1) and a converging lens (focal length f_2). The acoustic focus of the PZT wave being of about 100 μm width, the laser must be focused at the center of the experimental cell so that its Rayleigh range is less than $z_{2_{max}} = 50$ μm. This value imposes that the angular divergence θ_2 of the focusing beam must be superior to $\theta_{2_{min}} = \sqrt{\frac{\lambda}{\pi z_{2_{max}}}} \sim 5^\circ$ for $\lambda = 1.064$ μm. The angular acceptance of the cryostat $\theta_{2_{max}} \sim 12.5^\circ$ is thus not a very limiting factor. However, as the distance between the center the cell and the outside window of the cryostat is $d \sim 145$ mm and the initial beam divergence is about 0.5 mrad for a beam initial diameter of about 2 mm, a single converging lens can not be used in order to fulfill the condition $\theta_2 > \theta_{2_{min}}$. That is the reason why the laser beam is first expanded using the diverging f_1 lens. For $f_1 = -100$ mm and $f_2 = +150$ mm spaced by 775 mm, one finds that a perfect gaussian laser of initial with previously mentioned divergence and radius must focus at distance $s_2' = 181$ mm from lens f_2 with a waist $w_2 = 3.3$ μm corresponding to a Rayleigh range $z_2 = 28$ μm. Any retro-reflected Brillouin signal coming back from the experimental cell can be collected using the polarization arrangement shown in figure III.4 b).

Using this set up, we unfortunately didn't manage for now to measure any clear retro-reflected signal in stable liquid ^{4}He at saturated vapor pressure. But interestingly, we have seen optical breakdown and plasma creation as shown on figure III.5. The fact that we obtain optical breakdown and no Brillouin signal does not depend on the temperature and especially whether the liquid is superfluid or not as we have performed this experiment between 1 K and 4 K with always the same conclusion.

Getting optical breakdown prior to any Brillouin reflected signal was kind of a surprise to me. I was then suspecting that the spatial profile of the Ekspla

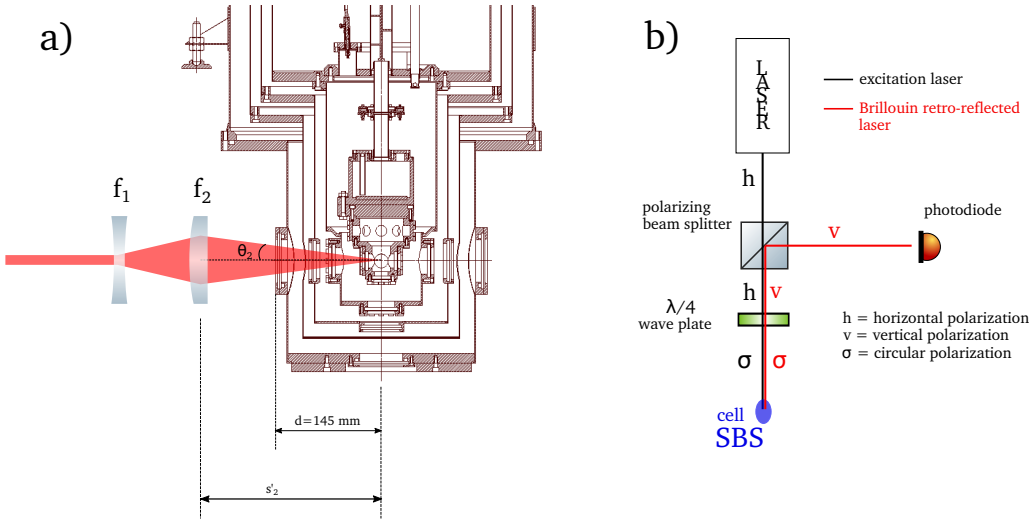

Fig.III.4: Experimental set up used for generating SBS inside our experimental cell. a) A two lenses arrangement is used to obtain the desired optical waist $w_2 = \lambda/(\pi\theta_2)$ at the center of the cell. b) Polarization arrangement used to separate the excitation beam from the expected retro-reflected Brillouin signal. After passing two times in a $\lambda/4$ retardation wave plate, the initially linearly horizontally polarized beam is turned to be vertically polarized and escapes the polarizing beam splitter at 90° from the initial direction of propagation.

laser at acoustic focus might be bad, possibly with local hot intensity spots that may trigger the optical breakdown phenomenon. I then decided to try this SBS experiment with another available laser in our lab, namely a frequency double Nd-Yag laser ($\lambda = 532$ nm) with a pulse width of 8 ns and a maximal peak power of about 8 MW. This laser has a good quasi gaussian spatial profile in the far field (as measured by the manufacturer Quantel) and is then expected not to have hot intensity spots when focused. It was though not a longitudinal single mode laser. This experiment was the topic of the Master-2 internship of Lionel Djadaodjee between April and June 2018. Lionel used the same two lenses set up and first tried to get SBS in acetone at room temperature (Brillouin gain of 0.2 m/GW not too far from our estimation of equation III.2.1 for liquid helium). He managed to get a SBS signal in acetone only for particular values of focal lengths f_1 and f_2, that is for particular values of the waist w_2. However, when we used exactly the same lenses configuration to trigger SBS in liquid ^{4}He, the only thing we got was again optical breakdown. Laser induced optical breakdown in liquid helium-4 was seen by others. A very recent experimental paper of H. Maris deals with this topic[56]. And back in the late 60's, the same Winterling which has succeeded in generating SBS in liquid ^{4}He also published a paper where he

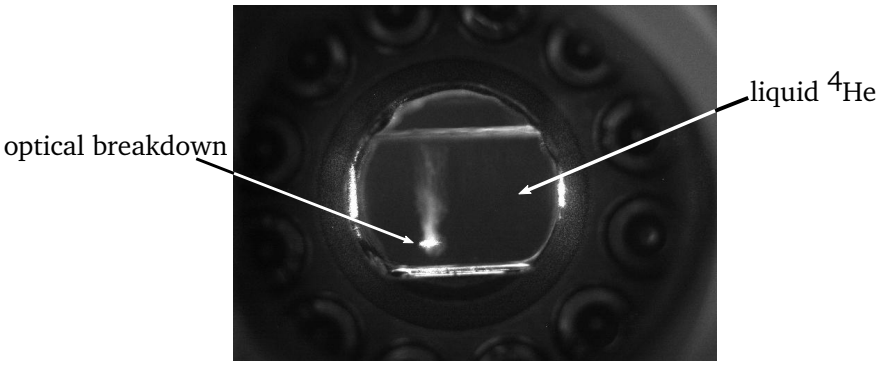

Fig.III.5: Laser induced optical breakdown in liquid ^{4}He at $T = 4$ K.

measured the laser intensity needed to generate optical breakdown in liquid ^{4}He and found it to be in the range $10^{10} - 10^{11}$ W/cm^2[57]. We find the same order of magnitude for the optical breakdown intensity. Work needs to be done to understand why we don't get SBS in our configuration. An important difference between Leiderer's and Winterling's successful SBS experiments and ours is that they had a single focus lens of short focal length (typically 50 mm) directly immersed in a Deware filled with the liquid. In our case, optical aberrations due to the crossing of the 4 windows of the cryostat by the converging laser could play an important role in loosely shaping the spatial profile of the laser at acoustic focus thus triggering the breakdown of the liquid. Whether focusing the laser from outside the cryostat is a limiting factor can be tested by focusing the laser using a single (short focal length) lens directly placed in one of the optical port of the experimental cell.

The good news though of these preliminary results is that the optical breakdown signal will be of great help in the certainly difficult alignment of the laser optical waist with the acoustic focus of the PZT wave.

Conclusion

In this manuscript, I described my research work achieved in the group "Quantum solids and fluids" of Laboratoire Kastler Brossel since 2009. These experiments deal with the production and characterization of metastable states of liquid and solid ^{4}He.

The metastable states are produced by using a well shaped piezo electric transducer that focuses a pressure/density wave in the bulk of the sample. The particularity of our experimental set-up is that we measure the local density of the metastable states.

In the case of metastable liquid ^{4}He, we have been able to measure the density at which cavitation occurs at temperature of about 1 K. This measurement is important because experiments by other groups in the late 90's have measured the pressure at which liquid ^{4}He cavitates. It turns out that our density measurement and these pressure measurements are not compatible when they are linked by a theoretical equation of state. While doing this density measurement on metastable liquid ^{4}He, we discovered that the lifetime of cavitation bubbles dramatically depends on whether the liquid is superfluid or not. We have explained this behavior by the radically different heat conduction properties of the two fluids.

Regarding solid ^{4}He, we have been the first group to successfully produce and observe a metastable state of hcp solid ^{4}He. Metastable hcp solid ^{4}He is of interest because it is a potential candidate for a supersolid state of matter. In trying to increase the metastability of the solid, we encountered an unexpected instability. A determination of the time of birth of the instability has shown that the instability always starts in the negative swings of the acoustic wave that is when the solid is indeed in its metastable sate. Recordings of the exact positions of the initial defect show that the instability nucleates at acoustic focus where the density variations are important and shear constrains vanish. This instability is density induced and can be linked to some limits of the metastability which solid ^{4}He can eventually reach.

To better understand the observed destabilization of both metastable solid and liquid ^{4}He, the future of this experiment consists in building an experimental set-up capable of measuring the equation of state of the metastable states. In the case of metastable liquid ^{4}He, measuring the equation of state is necessary

to check the validity of the theoretical one which is questioned by our cavitation density measurement. In the case of metastable solid ^{4}He, the measurement of the compressibility (and hence of the equation of state) in the vicinity of the instability must be done to check for any potential anomalous behavior. I propose to measure these equations of state using Stimulated Brillouin Scattering of an intense laser pulse. Primarily results show that care must be taken in the laser choice and lens configuration in order to indeed trigger Stimulated Brillouin Scattering in liquid ^{4}He.

Bibliography

[1] A. Qu, "Experimental study of metastable solid and liquid helium-4," PhD Thesis, Université Pierre et Marie Curie, Paris, France (2017). URL: https://tel.archives-ouvertes.fr/tel-01591897. I

[2] J. A. Nissen, E. Bodegom, L. C. Brodie, and J. S. Semura, "Tensile strength of liquid ^{4}He," Phys. Rev. B **40**, 6617–6624 (1989). URL: https://link.aps.org/doi/10.1103/PhysRevB.40.6617. I.1.1, 2

[3] F. Caupin, S. Balibar, and H. J. Maris, "Limits of metastability of liquid helium," Physica B: Condensed Matter **329**, 356–359 (2003). URL: https://www.sciencedirect.com/science/article/pii/S0921452602021038. I.1.2

[4] F. Souris, "L'hélium solide méstastable en sous-pression (french)," PhD Thesis, Université Pierre et Marie Curie, Paris, France (2013). URL: https://tel.archives-ouvertes.fr/tel-00942738. I.2, II.1, II.1.3, II.2.3

[5] F. Souris, J. Grucker, J. Dupont-Roc, P. Jacquier, A. Arvengas, and F. Caupin, "Time-resolved multiphase interferometric of a highly focused ultrasound pulse," Applied Optics **49**, 6127. URL: https://www.osapublishing.org/ao/abstract.cfm?uri=ao-49-31-6127. I.2

[6] M. Deutsch and I. Beniamy, "Inversion of abel's integral equation for experimental data," J. Appl. Phys. **54**, 137 (1983). URL: http://aip.scitation.org/doi/abs/10.1063/1.331739. I.2

[7] A. Arvengas, K. Davitt, and F. Caupin, "Fiber optic probe hydrophone for the study of acoustic cavitation in water," Review of Scientific Instruments **82**, 034904 (2011). URL: https://doi.org/10.1063/1.3557420. I.2

[8] A. Qu, A. Trimeche, J. Dupont-Roc, J. Grucker, and P. Jacquier, "Cavitation density of superfluid helium-4 around 1 K," Physical Review B **91**, 214115 (2015). URL: https://journals.aps.org/prb/abstract/10.1103/PhysRevB.91.214115. I.3.1

[9] F. Caupin and S. Balibar, "Cavitation pressure in liquid helium," Phys. Rev. B **64**, 064507 (2001). URL: http://link.aps.org/doi/10.1103/PhysRevB.64.064507. I.3.1, I.3.2

[10] H. Maris, "Theory of quantum nucleation of bubbles in liquid helium," Journal of Low Temperature Physics **98**, 403–424 (1995). URL: http://dx.doi.org/10.1007/BF00752276. I.3.2

[11] G. H. Bauer, D. M. Ceperley, and N. Goldenfeld, "Path-integral monte carlo simulation of helium at negative pressures," Phys. Rev. B **61**, 9055–9060 (2000). URL: http://link.aps.org/doi/10.1103/PhysRevB.61.9055. I.3.2

[12] F. Dalfovo, A. Lastri, L. Pricaupenko, S. Stringari, and J. Treiner, "Structural and dynamical properties of superfluid helium: A density-functional approach," Phys. Rev. B **52**, 1193–1209 (1995). URL: http://link.aps.org/doi/10.1103/PhysRevB.52.1193. I.3.2

[13] J. Boronat, J. Casulleras, and J. Navarro, "Monte carlo calculations for liquid ^{4}He at negative pressure," Phys. Rev. B **50**, 3427–3430 (1994). URL: http://link.aps.org/doi/10.1103/PhysRevB.50.3427. I.3.2

[14] H. J. Maris and D. O. Edwards, "Thermodynamic properties of superfluid ^{4}He at negative pressure," J. Low Temp. Phys. **129**, 1 (2002). URL: https://link.springer.com/article/10.1023/A:1020060700534. I.3.2

[15] Q. Xiong and H. J. Maris, "Study of cavitation in superfluid helium-4 at low temperatures," J. Low Temp. Phys. **82**, 105 (1991). URL: https://link.springer.com/article/10.1007/BF00681524. I.3.2

[16] Appert, C., Tenaud, C., Chavanne, X., Balibar, S., Caupin, F., and d'Humières, D., "Nonlinear effects and shock formation in the focusing of a spherical acoustic wave," Eur. Phys. J. B **35**, 531–549 (2003). URL: http://dx.doi.org/10.1140/epjb/e2003-00307-0. I.3.2

[17] A. Qu, A. Trimeche, P. Jacquier, and J. Grucker, "Dramatic effect of superfluidity on the collapse of ^{4}He vapor bubbles," Physical Review B **93**, 174521 (2016). URL: https://journals.aps.org/prb/abstract/10.1103/PhysRevB.93.174521. I.4

[18] Rayleigh, "On the pressure developed in a liquid during the collapse of a spherical cavity," The London, Edinburgh, and Dublin Philosophical Magazine and Journal of Science **34**, 94–98 (1917). URL: https://doi.org/10.1080/14786440808635681. I.4.2

[19] M. S. Plesset and A. Prosperetti, "Bubble dynamics and cavitation," Annual review of fluid mechanics **9**, 145–185 (1977). URL: https://doi.org/10.1146/annurev.fl.09.010177.001045. I.4.4

[20] J. Wilks, *The properties of liquid and solid helium* (Oxford University Press, 1967). I.4.4

[21] N. Yadav, V. Vadakkumbatt, H. J. Maris, and A. Ghosh, "Exploding and imaging of electron bubbles in liquid helium," Journal of Low Temperature Physics **187**, 618–626 (2017). URL: https://doi.org/10.1007/s10909-016-1713-7. I.4.4

[22] D. Duda, P. Švančara, M. La Mantia, M. Rotter, D. Schmoranzer, O. Kolosov, and L. Skrbek, "Cavitation bubbles generated by vibrating quartz tuning fork in liquid ^{4}He close to the λ-transition," Journal of Low Temperature Physics **187**, 376–382 (2017). URL: https://doi.org/10.1007/s10909-016-1684-8. I.4.4

[23] A. F. Andreev and I. M. Lifshitz, "Quantum theory of defects in crystals," Sov. Phys-JETP **29**, 1107–1113 (1969). URL: http://www.jetp.ac.ru/cgi-bin/e/index/e/29/6/p1107?a=list. II.1.1

[24] G. V. Chester, "Speculations on bose-einstein condensation and quantum crystals," Phys. Rev. A **2**, 256–258 (1970). URL: https://journals.aps.org/pra/abstract/10.1103/PhysRevA.2.256. II.1.1

[25] E. Kim and M. H. Chan, "Observation of superflow in solid helium," Science **305**, 1941–1944 (2004). URL: http://science.sciencemag.org/content/305/5692/1941. II.1.1

[26] E. Kim and M. Chan, "Probable observation of a supersolid helium phase," Nature **427**, 225–227 (2004). URL: https://www.nature.com/articles/nature02220. II.1.1

[27] A. S. C. Rittner and J. D. Reppy, "Observation of classical rotational inertia and nonclassical supersolid signals in solid ^{4}He below 250 mk," Phys. Rev. Lett. **97**, 165301 (2006). URL: https://link.aps.org/doi/10.1103/PhysRevLett.97.165301. II.1.1

[28] S. T. Motoshi Kondo and S. Shirahama, "Observation of non-classical rotational inertia in bulk solid ^{4}He," J. Low Temp. Phys. **148**, 695 (2007). URL: https://link.springer.com/article/10.1007/s10909-007-9471-1. II.1.1

[29] Y. Aoki, J. C. Graves, and H. Kojima, "Oscillation frequency dependence of nonclassical rotation inertia of solid ^{4}He," Phys. Rev. Lett. **99**,

015301 (2007). URL: https://link.aps.org/doi/10.1103/PhysRevLett.99.015301. II.1.1

[30] A. Penzev, Y. Yasuta, and M. Kubota, "ac vortex-dependent torsional oscillation response and onset temperature T_0 in solid ^{4}He," Phys. Rev. Lett. **101**, 065301 (2008). URL: https://link.aps.org/doi/10.1103/PhysRevLett.101.065301. II.1.1

[31] J. Day and J. Beamish, "Low-temperature shear modulus changes in solid 4he and connection to supersolidity," Nature **450**, 853–856 (2007). URL: https://www.nature.com/articles/nature06383. II.1.1

[32] S. Balibar, "The enigma of supersolidity," Nature **464**, 176–182 (2010). URL: https://www.nature.com/articles/nature08913. II.1.1

[33] J. R. Beamish, A. D. Fefferman, A. Haziot, X. Rojas, and S. Balibar, "Elastic effects in torsional oscillators containing solid helium," Phys. Rev. B **85**, 180501 (2012). URL: https://link.aps.org/doi/10.1103/PhysRevB.85.180501. II.1.1

[34] D. Y. Kim and M. H. W. Chan, "Absence of supersolidity in solid helium in porous vycor glass," Phys. Rev. Lett. **109**, 155301 (2012). URL: http://link.aps.org/doi/10.1103/PhysRevLett.109.155301. II.1.1

[35] M. W. Ray and R. B. Hallock, "Observation of unusual mass transport in solid hcp ^{4}He," Phys. Rev. Lett. **100**, 235301 (2008). URL: https://link.aps.org/doi/10.1103/PhysRevLett.100.235301. 1

[36] Z. G. Cheng, J. Beamish, A. D. Fefferman, F. Souris, S. Balibar, and V. Dauvois, "Helium mass flow through a solid-superfluid-solid junction," Phys. Rev. Lett. **114**, 165301 (2015). URL: https://link.aps.org/doi/10.1103/PhysRevLett.114.165301. 1

[37] A. Eyal, X. Mi, A. V. Talanov, and J. D. Reppy, "Search for supersolidity in solid ^{4}He using multiple-mode torsional oscillators," Proceedings of the National Academy of Sciences **113**, E3203–E3212 (2016). URL: http://www.pnas.org/content/113/23/E3203. 1

[38] B. Chaudhuri, F. Pederiva, and G. V. Chester, "Monte carlo study of vacancies in the bcc and hcp phases of ^{4}He," Phys. Rev. B **60**, 3271–3278 (1999). URL: https://link.aps.org/doi/10.1103/PhysRevB.60.3271. II.1.1

[39] B. A. Fraass, P. R. Granfors, and R. O. Simmons, "X-ray measurements of thermal vacancies in hcp ^{4}He," Phys. Rev. B **39**, 124–131 (1989). URL: http://link.aps.org/doi/10.1103/PhysRevB.39.124. II.1.1, II.1.1, II.1

[40] "On the propagation of elastic waves in aeolotropic media ii. media of hexagonal symmetry," Proceedings of the Royal Society of London A: Mathematical, Physical and Engineering Sciences **226**, 356–366 (1954). URL: http://rspa.royalsocietypublishing.org/content/226/1166/356. II.1.3

[41] R. Crepeau and D. Lee, "Consequences of anisotropic sound velocities in hcp solid helium," Phys. Rev. A **6**, 516. URL: https://link.aps.org/doi/10.1103/PhysRevA.6.516. II.1.3, II.4a, II.4b

[42] F. Souris, J. Grucker, N. Garroum, A. Leclercq, J.-M. Isac, J. Dupont-Roc, and P. Jacquier, "Design, fabrication and characterization of a monolithic focusing piezoceramic transducer for an anisotropic material," Review of Scientific Instruments **85**, 064902 (2014). URL: https://doi.org/10.1063/1.4881535. II.1.3.1

[43] K. Keshishev, A. Parshin, and A. Babkin, "Crystallization waves in ^{4}He," Journal of Experimental and Theoretical Physics **53**, 362 (1981). URL: http://www.jetp.ac.ru/cgi-bin/e/index/e/53/2/p362?a=list. II.2.1

[44] S. Balibar, H. Alles, and A. Y. Parshin, "The surface of helium crystals," Rev. Mod. Phys. **77**, 317–370 (2005). URL: https://link.aps.org/doi/10.1103/RevModPhys.77.317. II.2.1

[45] E. R. Grilly, "Pressure-volume-temperature relations in liquid and solid4he," Journal of Low Temperature Physics **11**, 33–52 (1973). URL: https://doi.org/10.1007/BF00655035. II.2.2

[46] M. H. Edwards, "Refractive index of ^{4}He: Saturated vapor," Phys. Rev. **108**, 1243–1245 (1957). URL: https://link.aps.org/doi/10.1103/PhysRev.108.1243. II.2.2, III.2.1

[47] H. J. Maris, "Properties of mestastable solid helium below the normal melting pressure," Journal of Low Temperature Physics **155**, 290–302 (2009). URL: https://doi.org/10.1007/s10909-009-9881-3. II.2.3

[48] K. Davitt, E. Rolley, F. Caupin, A. Arvengas, and S. Balibar, "Equation of state of water under negative pressure," J. Chem. Phys. **133**, 174507. URL: https://doi.org/10.1063/1.3495971. III.1

[49] R. W. Boyd, *Nonlinear Optics, Third Edition* (Academic Press, Inc., Orlando, FL, USA, 2008), 3rd ed. III.2.1, III.2

[50] R. J. Donnelly and C. F. Barenghi, "The observed properties of liquid helium at the saturated vapor pressure," Journal of Physical and Chemical Reference Data **27**, 1217–1274 (1998). URL: https://doi.org/10.1063/1.556028. III.2.1, 2

[51] P. Berberich, P. Leiderer, and S. Hunklinger, "Investigation of the lifetime of longitudinal phonons at ghz frequencies in liquid and solid ^{4}He," Journal of Low Temperature Physics **22**, 61–84 (1976). URL: https://doi.org/10.1007/BF00655215. III.2.1, III.2.2

[52] R. W. Boyd, K. Rzążewski, and P. Narum, "Noise initiation of stimulated brillouin scattering," Phys. Rev. A **42**, 5514–5521 (1990). URL: https://link.aps.org/doi/10.1103/PhysRevA.42.5514. III.2.1

[53] G. Winterling, G. Walda, and W. Heinicke, "Stimulated brillouin scattering in liquid helium," Physics Letters A **26**, 301 – 302 (1968). URL: http://www.sciencedirect.com/science/article/pii/0375960168906622. III.2.2

[54] W. Heinicke and G. Winterling, "The temperature dependence of stimulated brillouin scattering in quartz," Applied Physics Letters **11**, 231–233 (1967). URL: https://doi.org/10.1063/1.1755112. III.2.2

[55] I. Abrikosova and N. Skrypnik, "Laser-beam-induced breakdown and stimulated mandel'shtam-brillouin scattering in liquid ^{4}He," Journal of Experimental and Theoretical Physics **32**, 34 (1967). URL: http://www.jetp.ac.ru/cgi-bin/e/index/e/32/1/p34?a=list. III.2.2

[56] S. Sirisky, Y. Yang, W. Wei, and H. J. Maris, "Laser-induced breakdown in liquid helium," Journal of Low Temperature Physics **189**, 53–59 (2017). URL: https://doi.org/10.1007/s10909-017-1786-y. III.3.2

[57] G. Winterling, W. Heinicke, and K. Dransfeld, "Laser-induced breakdown in liquid ^{4}He," Phys. Rev. **185**, 285–287 (1969). URL: https://link.aps.org/doi/10.1103/PhysRev.185.285. III.3.2

Curriculum vitae

Jules GRUCKER

Born in Strasbourg (France) 26/05/1981

Professional address: Laboratoire Kastler Brossel, 24 rue Lhomond, 75321 Paris

Phone : +33 1 44 32 25 09 (office), +33 1 44 32 34 29 (lab)

Email : grucker@lkb.ens.fr

2 kids

Academics

1999 - 2002	**Bachelor in physics**, Université Louis Pasteur, Strasbourg (France).
2002 - 2003	**Master 1**, Niels Bohr Institute, University of Copenhagen, Danemark.
2003 - 2004	**Master 2 "Experimental Physics of Atoms and Molecules"**, Université Pierre et Marie Curie (now Sorbonne Université), Paris (France).
2004 - 2007	**Phd : "Expériences d'optique atomique cohérente ou non avec un jet superfin d'atomes métastables de gaz rares (french)"** ("Atom optic experiments with an ultra narrow beam of metastable rare gas atoms"), Laboratoire de Physique des Lasers (LPL), Université Paris 13, Villetaneuse (France). PhD supervisor: Francisco Perales. Defense committee: Jacques Baudon, Philippe Jacquier (referee), Michèle Leduc (president), Francisco Perales, Jacques Robert, John Weiner (referee).

Jobs and positions

2004 - 2007	**PhD**, Laboratoire de Physique des Lasers (LPL), Université Paris 13.
2007 - 2008	**Attaché Temporaire Enseignement Recherche** (Post doc with research and teaching assignments), Laboratoire de Physique des Lasers, Université Paris 13.
2008 - 2009	**Post-doc**, Cretan matter waves group, Institute of Electronic Structure and Laser (IESL), Heraklion, Greece. Supervisor: Wolf von Klitzing.
Sept 2009 - ...	**Assistant Professor**, Sorbonne Université, Laboratoire Kastler Brossel (LKB), Paris.

Thematic and geographical mobility

During my PhD thesis, I conducted atomic optics experiments with a jet of metastable atoms that allowed me to study the atom-surface interactions in various situations. The general framework of this work was therefore that of atomic physics in a diluted medium with "thermal" atomic jets, that is to say with a mean squared velocity of the order of a hundred m/s. In my post-doc in Greece, I went to the physics of ultra-cold atoms but still in the gaseous phase by working on the implementation of a Bose-Einstein condensation experiment of rubbidium atoms. Finally, since September 2009, I am working on solid or liquid ^{4}He, that is to say condensed matter physics at cryogenic temperature.

As for geography, I worked in 3 different laboratories, LPL (Paris 13 University,Villetaneuse, France), IESL (Heraklion, Greece) and LKB (Sorbonne Université, Paris).

Teaching activities

A very important part of my work is to teach at Sorbonne Université. Since 2009, I teach 192h/year of tutorials and lab courses at the Bachelor level (L1=first year, L2, L3).

- *L1, First year of medicine school: 2009→2017.* Basis for different fields of classical physics (mechanics, fluid mechanics, thermodynamics, electromagnetism ...)
- *L1, Thermodynamics for biophysicists : 2009→2012.*
- *L1, Calculation methods and statistics: 2011→2012.* Maths and statistics for physicists.

- *L1, Concepts and methods for physics: 2014.* Introduction to mechanics mainly.

- *L1, Energy and entropy: 2014→2016.* Introduction to thermodynamics for physicists.

- *L2, Electromagnetism : 2013,2017→2018.* Electro-static, magneto-static, induction, electromagnetic waves in vacuum.

- *L2, Quanta and relativity: 2015→2018.* Introduction to quantum mechanics and special relativity. For this course, I sat-up a new lab course which consists in measuring the shot noise of a flash light with a simple photodiode, a bit of electronics and an oscilloscope.

- *L3, Thermodynamics et thermo-statistics : 2016→2018.* Advanced thermodynamics and introduction to statistical physics.

Co-supervision of young researchers

PhD students

- Vassiliki Bolpasi, 1 year of co-supervision. During my post doc in Crete (2008 - 2009), Vassiliki was the PhD working on the experiment which we started to build together. She defended her PhD on May 12 2014 "An Ultra-High Flux Matter-Wave Laser from a Highly Flexible Ioffe-Pritchard Trap" University of Crete, Heraklion, Greece. Since, Vassiliki is a post-doc in the same research group.

- Fabien Souris (2009 → 2013), supervision 20%. (Jacques Dupont-Roc 40%, Philippe Jacquier 40%). When I arrived at LKB in September 2009, Fabien Souris began his thesis. It was the beginning of the metastable solid experiment. In addition to build-up, run and discuss the experiment, Fabien and I had a lot of discussions about the course of his thesis and also of the course of the post-thesis. He defended his thesis entitled "Solid Metastable Helium Under Pressure" on January 17, 2013. He then went for a post doc in the group of Sébastien Balibar (Laboratoire de Physique Statistique, ENS, Paris) working on dislocation mobility and mass flow in (stable) solid ^{4}He between 2013 and 2015. In 2015, he joined as a post-doc the group of John Davis at the University of Alberta (Canada) where he was interested in superfluid ^{4}He as a micromechanical resonator. Since 2018, he is a post-doc in the group of Pierre-Etienne Wolf at the Institut Néel in Grenoble (France) where he is working on cavitation in porous media.

- Qu An (2013 → 2017), supervision 50%. (Philippe Jacquier 50%). After Jacques Dupont-Roc retired, I became the main permanent member present in the lab. It was therefore with me that Qu An learned to make this experience run. It was with me that Qu An first discussed his results and experimental problems. I encouraged him to write parts of our articles and to go to conferences. I read and correct his PhD manuscript in parallel with Ph. Jacquier. I also actively participated in the constitution of his thesis defense committee. Qu An defended his thesis entitled "Experimental study of metastable solid and superfluid helium-4" on January 20, 2017. Since then, his is a post-doc in the group of Jean Dalibar and Fabrice Gerbier at the Collège de France where he working on an experiment of sodium spinor condensates (Bose Einstein condensates with a spin internal degree of freedom).

Post doc

- Between October 2013 and September 2015, Azer Trimèche was post-doc (CNRS) in our team. This post-doc corresponding to the period of the thesis of Qu An, it is me who mainly supervised Azer in the day to day work in the lab. After his stay in our lab, he went for a post doc in the team of Franck Perreira Dos Santos (Laboratoire SYRTE, observatoire de Paris) working on cold atom interferometers. He was there for 2 years. Since February 2018, he is post doc in the group of Daniel Comparat at Laboratoire Aimé Cotton (Orsay University, France) working on the realization of cold ion and electron beams.

Master 2 students

- Qu An (3 months in 2013) supervision 50%. (Philippe Jacquier 50%). Before his PhD, Qu An made his master 2 internship in our lab. His topic was "Time of birth of the instability recently observed in hcp solid ^{4}He".

- Lionel Djadaodjee (3 months in 2018) supervision 100%. The topic of Lionel's master 2 internship was "Attempts in Stimulated Brillouin Scattering in liquid ^{4}He". In 2018/2019, Lionel is preparing the difficult exam of french agrégation.

Miscellaneous

- Referee for The Journal of Chemical Physics.

- Member of the lab council of LKB sonce 2010.

Publication list

Peer reviewed publications

1. An Qu, A. Trimeche, Ph. Jacquier and J. Grucker " Dramatic effect of superfluidity on the collapse of Helium-4 vapor bubbles", *Phys. Rev. B* **93**, 174521 (2016).

2. An Qu, A. Trimeche, J. Dupont-Roc, J. Grucker and Ph. Jacquier "Cavitation Density of Superfluid Helium-4 around 1 K", *Phys. Rev. B* **91**, 214115 (2015).

3. Souris F., Qu A., Dupont-Roc J., Grucker J. and Jacquier Ph. "On the Destabilization of Mestastable Solid ^{4}He", *J. Low Temp. Phys* **179**, 390 (2015).

4. Souris F., Grucker J., Garroum N., Leclerc A., Isac J.-M., Dupont-Roc J. and Jacquier Ph. "Design, fabrication and characterization of a monolithic focusing piezoceramic transducer for an anisotropic material", *Review of Scientific Instruments* **85**, 064902 (2014).

5. Bolpasi V., Grucker J., Morrissey M.J. and von Klitzing W. "A gradient and offset compensated Ioffe-Pritchard trap for Bose-Einstein condensation experiments", *J. Phys B At. Mol. Opt. Phys.* **45**, 235301 (2012).

6. Souris F., Grucker J., Dupont-Roc J. and Jacquier Ph. "Observation of metastable hcp solid helium", *Eur. Phys. Lett.* **95**, 66001 (2011).

7. Souris F., Grucker J., Dupont-Roc J. and Jacquier Ph. "Investigating Metastable hcp solid helium Below Its Melting Pressure", *J. Low Temp. Phys* **162**, 412 (2011).

8. Souris F., Grucker J., Dupont-Roc J., Jacquier Ph., Arvengas A. and Caupin F. "Time-resolved quantitative multiphase interferometric imaging of a highly focused ultrasound pulse", *Applied Optics* **49**, 6127 (2010).

9. Baudon J., Hamamda M., Grucker J., Perales F., Dutier G., Ducloy M and Bocvarski V. "Scattering of Slow Mestastable Atoms by Dielectrics Nanospheres", *J. Chem. Phys. A* **113**, 15188 (2009).

10. Baudon J., Hamamda M., Grucker J., Boustimi M., Perales F., Dutier G. and Ducloy M. "Negative-Index Media for Matter-Wave Optics", *Phys. Rev. Lett.* **102**, 140403 (2009).

11. Grucker J., Baudon J., Perales F., Dutier G., Bocvarski V., Karam J.-C., Vassilev G. and Ducloy M. "Schlieren imaging of nano-sacle inelastic transitions using a Fresnel biprism atom interferometer", *Eur. Phys. J. D* **102**, 140403 (2008).

12. Mainos C., Dutier G., Grucker J., Perales F., Baudon J. and Ducloy M. "Entanglement of molecular-orientation, rotational and orbital degrees of freedom in multiphoton wave packets", *J. Phys B At. Mol. Opt. Phys.* **41**, 035603 (2008).

13. Grucker J., Baudon J., Perales F., Dutier G., Vassilev G., Bocvarski V. and Ducloy M. "Study of low-energy resonant metastability exchange in argon by a pulsed merging beam technique", *J. Phys B At. Mol. Opt. Phys.* **41**, 021001 (2008).

14. Grucker J., Karam J.-C., Correira F., Perales F., Vassilev G., Bocvarski V., Cherif S.M., Baudon J. and Ducloy M. "Diffraction of fast metastable atoms by micrometric reflection gratings", *Eur. Phys. J. D* **41**, 467 (2007).

15. Karam J.-C., Grucker J., Boustimi M., Vassilev G., Reinhardt J., Mainos C., Bocvarski V., Robert J., Baudon J. and Perales F. "Surface-induced vibrational excitation of metastable nitrogen molecules traversing a micro-slit copper grating: a probe of surface profiles", *J. Phys B At. Mol. Opt. Phys.* **39**, 1837 (2006).

16. Karam J.-C., Grucker J., Boustimi M., Perales F., Bocvarski V., Baudon J., Vassilev G., Robert J. and Ducloy M. "van der Waals-Zeeman transitions of metastable neon atoms passing through a micro-slit copper grating", *Eur. Phys. Lett.* **74**, 36 (2006).

17. Milosavljevic A.R., Bocvarski V., Jureta J., Marinkovic B.P., Karam J.-C., Grucker J., Perales F., Vassilev G., Reinhardt J., Robert J. and Baudon J. "High resolution electron imaging system for sub-micron sized metastable atom beams produced by Stern-Gerlach interferometry", *Measurement science and technology* **16**, 1997 (2005).

18. Karam J.-C., Wipf N., Grucker J., Perales F., Boustimi M., Vassilev G., Bocvarski V., Mainos C., Baudon J. and Robert J. "Atom diffraction with a 'natural' metastable atom nozzle beam", *J. Phys B At. Mol. Opt. Phys.* **38**, 2691 (2005).

Conference proceedings

1. Souris F., Grucker J., Dupont-Roc J. and Jacquier Ph. "Imaging focused ultrasound pulses in superfluid helium4", in IOP (Eds), *Journal of Physics Conference Series*, 26th international conference on low temperature physics (LT26), Beijing China 10-17 August 2011, vol. **400**, article number 012069 (2012)

2. Perales F., Bocvarski V., Baudon J., Hamamda M., Grucker J., Dutier G., Mainos C., Boustimi M. and Ducloy M. "Negative-index media for matter

waves", in Katori H., Yoneda H., Nakagawa K., Shimizu F. (Eds), *Laser spectroscopy*, 19th international conference on laser spectroscopy, Kussharo Japan 07-12 June 2009, pp. 51-62 (2010)

3. Hamamda M., Dutier G., Boustimi M., Bocvarski V., Grucker J., Perales F., Baudon J. and Ducloy M. "Atom 'Meta-Optics' ; Negative-index media for matter waves in the nm range", in IEEE (Eds), *CLEO/QELS 2009, VOLS 1-5*, CLEO/QELS 2009, Baltimore USA 02-04 June 2009, pages 2448-2449 (2009)

4. Hamamda M., Grucker J., Dutier G., Perales F., Bocvarski V., Baudon J. and Ducloy M. "Nanoscopy of surface-induced van der Walls-Zeeman transitions", in Gigosos M.A., Gonzales M.A. (Eds), *Spectral line shapes vol 15, AIP conference proceedings*, 19th international conference on spectral line shapes, Valladolid Spain 15-20 June 2008, vol. **1058** pp. 246-256 (2009)

5. Grucker J., Baudon J., Karam J.-C., Perales F., Bocvarski V. and Ducloy M. "Coherent atom optics with fast metastable beams: Metastable helium diffraction by 1D and 2D magnetized reflection gratings", in Cetin S.A., Hikmet I. (Eds), *Six international conference of the Balkan-Physical-Union, AIP conference proceedings*, 6th international conference of the Balkan-Physical-Union, Istanbul Turkey 22-26 August 2006, vol. **899** pp. 34-36 (2007)

6. Grucker J., Baudon J., Karam J.-C., Perales F., Bocvarski V., Vassilev G. and Ducloy M. "Coherent atom optics with fast metastable rare gas atoms", in Hadzievski L., Marinkovic B.P., Simonovic N.S. (Eds), *Physics of Ionized Gases, AIP conference proceedings*, 23rd Summer School and International Symposium on Physics of Ionized Gases, Kopaonik Serbia Aug 28 - Sep 01 2006, vol. **876** pp. 28-40 (2006)

7. Karam J.-C., Grucker J., Boustimi M., Bocvarski V., Vassilev G., Reinhardt J., Mainos C., Perales F., Baudon J., Robert J. and Ducloy M. "Production of a 'natural' metastable nozzle beam: Van der Waals-Zeeman atomic levels near a metal surface", in Weiner J., Feenstra L., Schmiedmayer J. (Eds), *Conference on atoms and molecules near surfaces, Journal of Physics Conference series*, International conference on atoms and molecules near surfaces, Heidelberg Germany April 04-08 2005, vol. **19** pp. 40-43 (2005)

8. Baudon J., Karam J.-C., Boustimi M., Perales F., Bocvarski V., Vassilev G., Reinhardt J., Mainos C., Grucker J., Wipf N. and Robert J. "Transverse coherence of a natural metastable atom nozzle beam: Scattering and van der Waals-Zeeman transitions", in Hadzievski L. (Eds), *Physics of Ionized*

Gases, AIP conference proceedings, 22nd Summer School and International Symposium on Physics of Ionized Gases, Tara Nat Pk Serbia August 23-27 2004, vol. **740** pp. 67-73 (2004)

Conferences

- Low Temperature 28 (LT 28), Göteborg (Sweden) August 2017, poster «Acoustic cavitation in liquid helium-4 : density measurement and bubble lifetime »
- Congrès général de la Société Française de Physique, Marseille (France) July 2013, poster «Metastable solid ^{4}He»
- Low Temperature 26 (LT 26), Beijing (China) August 2011, poster «Observation of metastable hcp solid ^{4}He below its melting»
- Quantum Fluids and Solids 2010, Grenoble (France) August 2010, poster: «Investigating metastable solid helium below its melting pressure»
- Colloque de la Division de Physique Atomique, Moléculaire et Optique de la SFP et Journées de la Spectroscopie Moleculaire, Lille – Villeneuve d'Ascq (France), July 2008, oral(french) : « Diffraction d'atomes métastables par des réseaux en transmission et en réflexion ».
- International School of Optics and Optic Materials (ISCOM 2007), Belgrade (Serbia) Septembre 2007, oral: « Atomic Nanoscope ».
- 23rd International Symposium on the Physics of Ionized Gases, Kopaonik (Serbia) August 2006, oral: « Fast metastable atom diffraction by 1D and 2D magnetized reflection gratings ».
- 4ème Colloque de la Division de Physique Atomique, Moléculaire et Optique de la SFP, Dijon (France) July 2006, oral(french): « Un nouveau type de séparatrice atomique modulable: transitions van der Waals-Zeeman d'atomes de Néon métastables ».
- 38th European Group for Atomic Spectroscopy (EGAS), Ischia (Italy) June 2006, oral("Hot topics") : « A novel type of tunable atomic Beam Splitter : van der Waals – Zeeman transitions of metastable Neon atoms. »
- Gravitation et Expérience (GREX), Paris (France) October 2005, oral(french): « Transitions van der Waals – Zeeman induites par une surface dans des atomes de Néon métastables. »
- Quantum Electro Dynamics 2005, Les Houches (France) June 2005, poster : « Diffraction élastique et inélastique d'atomes métastables par des surfaces micro ou nano structurées ».

- 11th Young Atom Opticians Conference, Hanover (Germany) February 2005, poster : « Elastic and inelastic diffraction of metastable atoms passing through a nanoslit grating »

Joined articles

Applied Optics 2010

Time-resolved quantitative multiphase interferometric imaging of a highly focused ultrasound pulse

Fabien Souris,[1,*] Jules Grucker,[1] Jacques Dupont-Roc,[1] Philippe Jacquier,[1] Arnaud Arvengas,[2] and Frédéric Caupin[2]

[1]Laboratoire Kastler Brossel, ENS, UPMC-Paris 6, CNRS, 24 rue Lhomond, 75005 Paris, France

[2]Laboratoire de Physique Statistique, ENS, UPMC-Paris 6, Université Paris Diderot, CNRS, 24 rue Lhomond, 75005 Paris, France

*Corresponding author: fabien.souris@lkb.ens.fr

Received 13 May 2010; revised 25 September 2010; accepted 27 September 2010; posted 29 September 2010 (Doc. ID 128415); published 28 October 2010

Interferometric imaging is a well-established method to image phase objects by mixing the image wavefront with a reference one on a CCD camera. It has also been applied to fast transient phenomena, mostly through the analysis of single interferograms. It is shown that, for repetitive phenomena, multiphase acquisition brings significant advantages. A 1 MHz focused sound field emitted by a hemispherical piezotransducer in water is imaged as an example. Quantitative image analysis provides high resolution sound field profiles. Pressure at focus determined by this method agrees with measurements from a fiber-optic probe hydrophone. This confirms that multiphase interferometric imaging can indeed provide quantitative measurements.

OCIS codes: 100.3175, 110.4155, 120.5050, 110.5086, 100.3190, 120.5475.

1. Introduction

Interferometric imaging is a common method for investigating phase objects (see, for instance [1–3] and references therein). Sound waves are examples of such objects. Compared to other imaging methods, such as Schlieren imaging (see, for instance [4]), or stress-induced birefringence imaging [5], interferometric imaging has the advantage of providing directly quantitative measurements. Refractive index maps can be computed from those measurements, and, in the case of a sound wave, acoustic pressure can be determined. There are two methods of reconstructing phase maps from recorded interferograms. Fringe analysis [2,6] has the advantage of requiring only one image (or two, if fringe shift is used), but it implies a reduced spatial resolution and phase ambiguities. In multiphase (or phase shifting) interferometry, the map of the optical phase is extracted from several images taken while changing the phase of the reference beam. Applying this method to time-dependent phenomena requires special adaptations to circumvent the slow acquisition rate of common cameras. When the phenomenon is a steady sinusoidal oscillation with sufficient amplitude, information can be extracted from time-averaged images [7]. This is the case for the popular TV holography method [8]. For fast transient phenomena, a time sampling is to be made by using pulsed light sources to get images of the object at particular times. These quasi-instantaneous images registered by the CCD camera are read on much longer times. Recording the complete evolution is possible for repetitive transient phenomena by varying the delay between the laser pulse and the triggered phenomenon. Depending on the time scale of the phenomenon under study, pulsed light sources, such as pulsed LED [9,10], Q-switched lasers [11,12], or even femtosecond lasers [13–16] have been used.

Regarding multiphase interferometric imaging for fast transient phenomena, the literature provides very few examples. Fringe analysis with tilted reference wavefronts seems to be the widely used method,

0003-6935/10/316127-07$15.00/0

with the drawbacks mentioned previously. It is thus of interest to investigate whether pulsed multiphase interferometry can provide phase maps, or phase shift maps, for fast transient phase objects. In this article, it is shown that this method can indeed be used in such cases, and that it provides accurate images with little sensitivity to optical defects. The price to be paid is a longer acquisition process. As an example, a 1 MHz ultrasound pulse produced in water by an hemispherical transducer is imaged. In Section 2, the experimental arrangement is described, as well as the procedure to record several images with different reference phases, at various time delays. In Section 3, the corresponding data processing is detailed. The phase maps are extracted and unwrapped if phase shifts exceed $\pm\pi$. Then an inverse Abel transformation is applied to recover the local index of refraction and, hence, the sound pressure. The result is shown in Section 5 and discussed in Section 6.

2. Experimental Setup and Procedure

The experimental setup is sketched in Fig. 1. It is based on a Jamin interferometer [17] with a frequency-doubled pulsed Nd:YAG laser as a light source. The Jamin interferometer was chosen because of its simplicity and intrinsic stability. When separated, the two interfering beams are close to each other and undergo similar disturbances from air turbulence and encountered windows [18]. In the sample region, the two beams are 6 mm apart and are 6 mm high. Lens L_1 images the entrance rectangular diaphragm A on the sample, while L_2 makes an image of the sample onto the CCD camera. The laser (Big Sky Laser CFR200) delivers 120 mJ, 8 ns long pulses with a repetition rate of 20 Hz, from which only about 1 μJ pulses are derived by four vitreous reflections, and a $d = 2$ gray filter. The optical wavelength used is $\lambda_o = 532$ nm. The laser is transversally highly multimode with a flat-top profile. Its effective coherence length, as measured with the interferometer by the fringe contrast versus the optical path difference, was found to be 4 mm at half-contrast. Hence the optical path difference between the two beams was kept well below this value to get a good contrast. The imaging camera (Andor LUCA R) is triggered synchronously with the pulsed laser. Used with a 2×2 binning, it provides 280×502 pixel images of the 6 mm $\times$ 10.5 mm observed region. Image resolution is discussed at the end of this section and is of about 20 μm.

For scanning the interferometer, two 4 mm thick parallel plates S_1 are introduced in the reference beam, with symmetrical tilts to avoid beam displacement (see Fig. 1). They are allowed to rotate around a horizontal axis so that their tilt angle can be precisely controlled around 5°. This is achieved by moving a separator along the vertical axis. When changing its height h by $\delta h = 1$ mm, the tilt angle is changed by 0.05°, and the optical path by 0.14 μm. Because of their thickness, the plates S_1 also introduce a difference of about 4 mm in the optical length of the two interferometer paths. To keep the optical path difference smaller than the laser coherence length, a second pair of similar plates S_2 is introduced in the signal beam. Those are kept fixed. The phase shift between the two beams introduced by these devices is approximated as

$$\psi = \psi_0 + 2\pi \frac{h}{a}\left(1 + s\frac{h}{a}\right), \tag{1}$$

where $a \simeq 3.7$ mm and $s \simeq 0.04$, as determined by simple geometrical optics. In fact, the two parameters a and s depend somewhat on the incidence angle of the beams on the plates, which cannot be

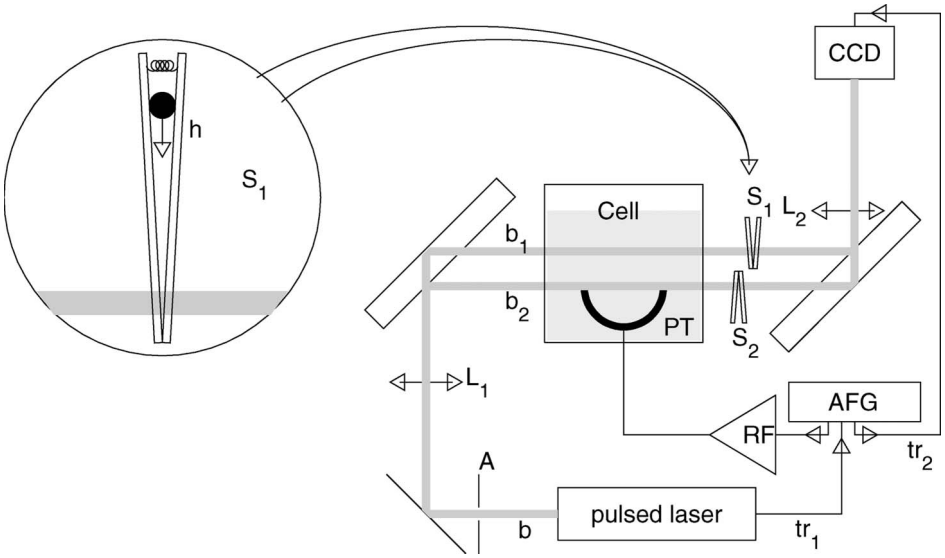

Fig. 1. Experimental setup: b, attenuated laser beam; tr1, trigger pulse sent by the laser 170 μs before the laser pulse; AFG, function generator; tr2, trigger pulse for the CCD camera; PT, piezo transducer driven by the amplifier RF; S_1, scanning plates for the interferometer; S_2, compensating plates. The inset shows how the optical path for the beam b_1 is changed by moving the separator of S_1 plates by h.

measured easily. So they are left as fitting parameters as explained in Section 3.

The phase object to be imaged is an ultrasound wave pulse (central frequency 1.06 MHz, duration 5 μs) emitted in water along the vertical axis by a piezoelectric hemisphere (inner diameter 12 mm, outer diameter 16 mm, provided by Channel Industries Inc.). Water used was filtered by reverse osmosis (Millipore Direct-Q ultrapure water system). The thickness vibration mode of the transducer is driven by an RF amplifier (RF in Fig. 1) fed with a function generator (Tektronix AFG3022) triggered from the laser command electronics with an adjustable delay. The same generator also triggers image acquisition by the camera. The sound velocity in water is 1480 m/s [19] at $T = 293$ K. The sound wavelength is $\lambda_s \simeq 1.4$ mm and the sound pulse length is about $L_s = 7$ mm. The sound pulse time of flight from the transducer inner surface to its center is about 4 μs. In the experiment, a trigger is given by the laser flash firing. The laser pulse takes place 170 μs later with a negligible jitter. The sound pulse is sent at time t varied from 157 to 169 μs by steps of 0.01 μs ($N_t = 1200$ time steps). For each time step, images are taken for $N_p = 25$ different values of h, labeled $h(1)\ldots h(p)\ldots h(N_p)$. The corresponding values of ψ, labeled $\psi(1)\ldots\psi(p)\ldots\psi(N_p)$, span an interval set to $\psi(N_p) - \psi(1) \simeq 3\pi$. Raw data are a set of $N_p \times N_t$ images labeled with their time delay and phase step. Their recording takes about 30 min. For each phase step, a reference image is first made by averaging $N_{\mathrm{av}} = 20$ images without exciting the transducer. These images of an undisturbed medium are later used as reference images for subtraction of a background phase field. The order in which h and t are varied is important to minimize interferometer drift effects. The sound pulse insertion time t is varied first at a fixed phase step along a complete time series, before changing h to the next phase step.

3. Phase Map Computation

During data processing, pixels are treated independently. Hence there is no spatial resolution loss due to image processing. Let $I(t,p)$ be the intensity recorded for a given pixel for the time index t and interferometer phase index p. It is expected that [1]

$$I(t,p) = I_0(t)[1 + C(t)\cos(\phi(t) - \psi(p))], \qquad (2)$$

where $I_0(t)$ is the average intensity, $C(t)$ is the fringe contrast, $\phi(t)$ is the optical phase to be measured for this particular pixel, and $\psi(p)$ is the interferometer phase given by Eq. (1) for each value of h. To extract $\phi(t)$, one needs to fit the N_p values $I(t,p)$ with Eq. (2) with five unknown parameters $I_0(t)$, $C(t)$, $\phi(t) - \psi_0$, a, and s. Because of the nonlinear term $(h/a)^2$ in Eq. (1), this involves a time-consuming nonlinear fitting procedure. Actually, the parameters ψ_0, a, and s do not depend much on time and position. Thus, they are only computed for pixels of the reference images for which $\phi(t)$ is zero. Actually, the variance of a is a few percent. Hence, only a mean value over space of those three parameters is computed and used in the next steps of the process. In the later images, only three parameters are to be determined for each pixel, namely, $I_0(t)$, $C(t)\cos(\phi(t))$, and $C(t)\sin(\phi(t))$. This can be done with a fast linear method [1,20] and takes about 1 s for the entire image of one time step.

The value $\phi(t)$ determined in this way is within the limits $-\pi$, π and undergoes possibly 2π phase jumps. The first time step is chosen so that the phase shift amplitude introduced by the sound field is less than π. The phase unwrapping is realized in time for each pixel by removing phase jumps $|\phi(t+1) - \phi(t)|$ larger than π. This is possible only if time steps verify the sampling condition, i.e., $|\phi(t+1) - \phi(t)| < \pi - 2\delta\phi$, where $\delta\phi$ is the phase noise. This condition actually sets the value of the time step and, consequently, the number of steps in the experiment. Usually, phase unwrapping is made spatially for each time on the two-dimensional maps, and then made continuous in time. Although many algorithms have been published on this topic [21], it is not a trivial problem. Unwrapping the phase in time for each pixel separately is much easier and faster. The continuity in space for the phase shift map $\phi(t,x,z) - \phi(0,x,z)$ is obtained automatically, because it starts from 0 everywhere and has no later phase jumps.

4. From Phase Map to Radial Sound Field

The phase ϕ is assumed to be related to the refractive index by a simple integration along the y axis parallel to the beam direction in the sample (see Fig. 2). More precisely, for each pixel (x,z), one takes into account the difference $\delta n(x,z,y)$ between the perturbed index $n(x,z,y)$ seen by the signal beam at point (x,y,z) and the refractive index n_0 of the unperturbed fluid seen by the reference beam on its parallel path. In our case, the sound field is rotationally invariant around the hemisphere axis z so that δn is a function of z and $r = \sqrt{x^2 + y^2}$ only. Then the phase map results from an integration of the refractive index variations over the path of the beam from the entrance window ($y = -l/2$), to the exit window ($y = l/2$):

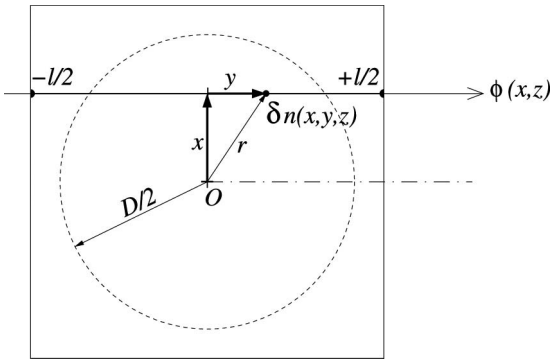

Fig. 2. Measured phase $\phi(x,z)$ results from the integration of the optical phase shift over the beam path in the cell. Dashed circle with diameter D, limit of the sound field.

$$\phi(x,z) = \frac{2\pi}{\lambda}\int_{-l/2}^{l/2} \mathrm{d}y \delta n\left(\sqrt{x^2+y^2}, z\right). \quad (3)$$

Note, however, that δn is identically 0 after some finite distance from the center (dashed circle on Fig. 2) because there is still no sound there. Hence, Eq. (3) can be rewritten as

$$\phi(x,z) = \frac{2\pi}{\lambda}\int_{-\infty}^{\infty} \mathrm{d}y \delta n\left(\sqrt{x^2+y^2}, z\right), \quad (4)$$

which is the Abel transform of the $\delta n(r,z)$ map. Conversely, radial refractive index profiles can be retrieved from phase maps via an inverse Abel tranform. To make that part easier, the camera lines and the signal light beam direction Oy have been carefully aligned parallel to the hemisphere basis. The abscissa x_0 of the hemisphere axis is determined as the symmetry axis of the projected sound field. Then the Abel inversion of the phase is performed for each line z on $\phi(z, x - x_0)$ using the algorithm proposed by [22]. The data are fitted with splines over successive sets of 20 pixels.

The Abel inversion procedure is justified provided that light rays do not suffer any significant deviation during their propagation through the studied sample. More precisely, the Raman–Nath condition should be fulfilled, i.e., deviation of a light beam from a straight line over the sample diameter D due to the refractive index gradient should be less than the optical resolution δx. Let λ_s be the sound wavelength, λ_o the laser light wavelength, and ϕ_m the maximum phase accumulated across the sample. Then the condition amounts to

$$\phi_m < \frac{\delta x \lambda_s}{D\lambda_o}. \quad (5)$$

With the values $\lambda_o = 0.5\ \mu$m, $\lambda_s = 1.4$ mm, and $\delta x \simeq \lambda_s/10$, the condition in Eq. (5) puts a rather large limit on ϕ_m, about 50. A second condition is that all rays collected by the imaging optics and originating from a given point of the object undergo the same ϕ retardation. Maximum transverse extension of such a ray bundle at the exit of the sample, i.e., at $D/2$, should be less than the characteristic length over which ϕ varies, typically λ_s. If θ is the aperture angle of the optics, this is true if $\theta D/2 < \lambda_s$. In our case, $D \simeq 16$ mm. This leads to the condition $\theta < 0.2$. The numerical aperture of the imaging lens is about $\theta = 0.03$ and fulfills the condition. In other respects, this numerical aperture should be large enough to ensure the desired optical resolution δx. The current aperture provides a resolution $\delta x = 1.2\lambda_o/\theta \simeq 20\ \mu$m.

The acoustic pressure field is proportional to δn and is computed from the relation

$$\delta P(x,z) = (n(x,z,y) - n_0)/(\partial n/\partial P), \quad (6)$$

where the water piezo-optic constant is $(\partial n/\partial P) \simeq 1.4 \times 10^{-4}$ MPa^{-1} [23,24].

5. Example of Ultrasound Pulse Image

In Figs. 3 and 4, three stages are shown from interference images to pressure map when the sound pressure is at its maximum at the focus. In Fig. 3(a), severe optical defects are clearly visible: dust particles; diffraction by the hemisphere rim. These defects are nearly completely washed out in the phase map [Fig. 3(b)]. In contrast, they could be seen obviously on the contrast map. This appears to be the main advantage of the multiphase method, the fitted phase being only weakly sensitive to intensity fluctuations. The signal to noise is good enough to yield an acceptable inverse Abel transform, from which the pressure is deduced using Eq. (6). Its radial profile is shown in Fig. 4(a), as well as its time variation at the focus when the sound pulse is going through [Fig. 4(b)]. While the transducer is excited at its resonance frequency by a constant amplitude sinusoidal burst of five periods, its response increases in time as expected from a driven damped harmonic oscillator. The oscillation is actively damped during the last oscillation. This explains the time profile of the sound pulse [Fig. 4(b)].

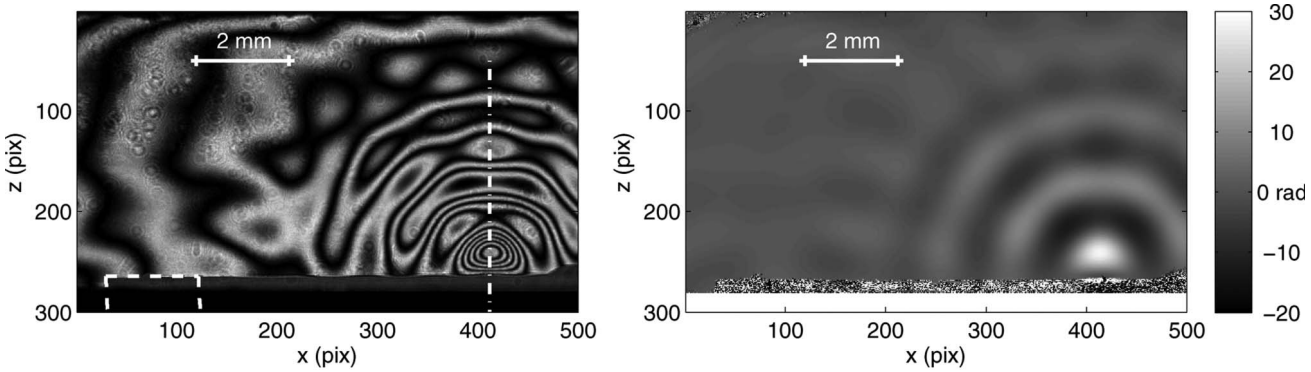

Fig. 3. (a) Image of the interference field above the piezo hemisphere. Dashed–dotted white line shows its axis and the dashed line outlines the profile of its meridian section. (b) Phase field determined from 25 similar images with stepped optical phase. Nontransparent regions of the field of view appear as random numbers.

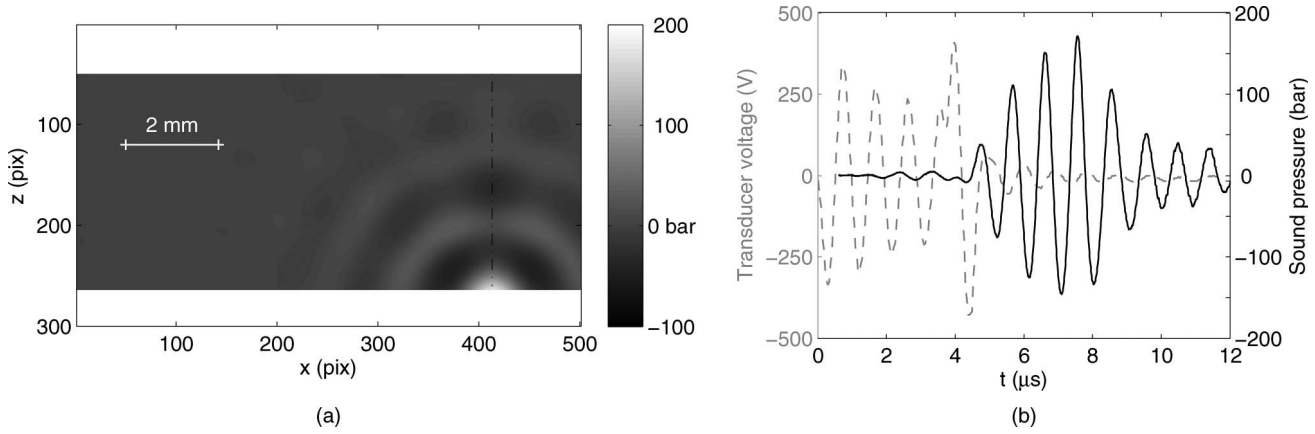

Fig. 4. (a) Pressure map computed from the phase map Fig. 3(b) by Abel inversion from pixel 1 to 414. Area from $x = 414$ to $x = 500$ are filled by symmetry. (b) Time variations of the computed pressure at the focus while the sound pulse goes through (solid curve). The transducer excitation voltage is also plotted (dashed curve), starting at $t = 0$.

This imaging method thus provides a way to investigate in detail the focusing properties of this type of transducer.

6. Discussion

Discussions of errors in multiphase interferometry may be found in [1,2,20,25]. Although written for static interferometric imaging, they apply equally well to the pulsed case. They show that the multiphase technique brings two benefits. The first one is to avoid systematic errors coming from imperfectly scanned phase ψ_p when predetermined schemes, such as $(-\pi/2, 0, \pi/2)$, $(-\pi/2, 0, \pi/2, \pi)$, or $(-\pi, -\pi/2, 0, \pi/2, \pi)$ are used [26]. Here, the phase is not scanned with an *a priori* scheme. Its value is extracted from the series of unperturbed images at $t = 0$. In Eq. (1), the slope $2\pi/a$ of the actual phase as a function of the scanning parameter h is left free, and a nonlinearity s is permitted by the fitting process. Hence, the only remaining errors may come from drifts in time of the interferometer. Because, in the experiment, changing the delay is 10 times faster than changing the phase, images are taken for a complete time series at a fixed reference phase. This takes about 60 s. Then the reference phase is changed to the next value. In this way, a possible drift in time of the interferometer geometry is in some way taken into account by the fitting process of a and s in formula (1). This scanning procedure, i.e., "time first, phase second," is thus to be preferred.

The second benefit from multiphase technique results simply from the larger number of data (here 25 images compared to a minimum of three to extract the phase, and compared to one for fringe analysis). This statistical improvement is thus $\sqrt{25/3}$ and $\sqrt{25}$, respectively. More quantitatively, let δI be the pixel noise for one image (including laser fluctuations and detection noise):

$$\delta\phi = \frac{\delta I/I_0}{\sqrt{CN_p}}. \tag{7}$$

Here, $\delta I/I_0 \simeq 0.1$, $C \simeq 1$, and $N_p = 25$. This gives $\delta\phi \simeq 0.02$, or $\lambda/300$ in a more commonly used unit.

Of course, the imaging technique has two well-known advantages compared to *in situ* point-by-point pressure measurement with a pressure probe. It provides parallel measurements at a large number of locations and times. This quality is reflected obviously by the large size of the generated data (gigabytes). It also provides this information in a noninvasive and nonperturbative way.

Nevertheless one may question the accuracy of the pressure field determined in this way. A quantitative analysis of the errors is not easy, in particular due to the lateral averaging brought by the diffraction on Eq. (3). Also, the phase field is not always determined up to a region where $\phi = 0$, inducing some error in the inverse Abel transform. Thus, to check the accuracy, a direct comparison was made with a fiber-optic probe hydrophone for the pressure at the focus. A fiber-optic probe hydrophone [23,27] determines the liquid refractive index modulation, by measuring the reflection coefficient R at the tip of an optical fiber. Reflection coefficient R is given by the Fresnel formula:

$$R = \left[\frac{n_f - (n_w + \delta n_w)}{n_f + (n_w + \delta n_w)}\right]^2, \tag{8}$$

where n_f and n_w are the optical fiber and water refractive indices. Water refractive index modulations δn_w due to sound waves are retrieved from those of R, after averaging over typically 100 bursts. Corrections due to the nonzero compressibility of the fiber core are taken into account by

$$\delta n_f = \delta n_w \frac{\partial n_f/\partial P}{\partial n_w/\partial P}. \tag{9}$$

The derivatives of refractive indices with respect to pressure are $\partial n_w/\partial P \simeq 1.4 \times 10^{-4}$ MPa^{-1} [28] and $\partial n_f/\partial P \simeq 1.5 \times 10^{-5}$ MPa^{-1} [29]. The correction amounts to about 7%.

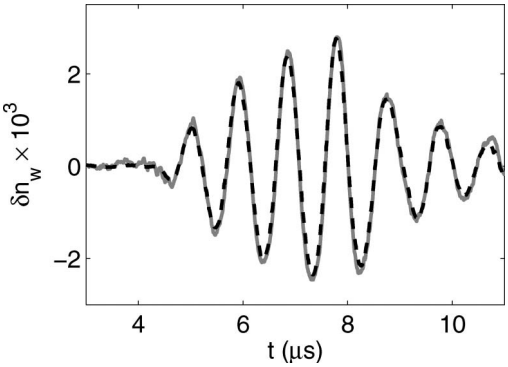

Fig. 5. Comparison of refractive index modulations obtained from the fiber-optic probe hydrophone (gray solid curve) and from inverse Abel transform of the phase map (dark dashed curve).

Because the physical quantity probed by the fiber-optic probe hydrophone and the interferometer are the same, a direct comparison can be made [30]. The fiber tip was set 0.12 mm above the piezo hemisphere center. This position was determined accurately by the images acquired during the measurement. Refractive index variations at the same point were also computed from interferometric measurements, taken with the hydrophone removed. Results are presented in Fig. 5. Both measurements are compatible within 5%. This is to be compared to the reproducibility of the hydrophone measurements (typically 10%), and the uncertainties in the inverse Abel transform due to the incomplete phase maps (which can amount to 5%). Hence, the agreement is satisfactory.

7. Conclusion

It appears that multiphase interferometric imaging can be easily applied to repetitive fast transient phenomena for which optical phase is a good observable. It provides quickly extensive data compared to point-by-point measurements. We have shown, in the case of a sound wave, that these data are quantitatively reliable. The multiphase feature brings a better immunity to optical defects in the images and an improved signal-to-noise ratio. Phase unwrapping in time appears as a very simple and robust algorithm. The longer acquisition time was found acceptable. Hence, this method could be more widely used than it has been up to now to study fast transient phenomena.

This research has been funded by the European Research Council (ERC) under the European Community's FP7 grant agreement 240113 and by the Agence Nationale de la Recherche, contract 05-BLAN-0084-02 META.

References and Notes

1. K. Creath, "Phase-measurement interferometry techniques," in *Progress in Optics*, E. Wolf, ed. (Elsevier, 1988), Vol. 26, pp. 349–393.
2. J. Schwider, "Advanced evaluation techniques in interferometry," in *Progress in Optics*, E. Wolf, ed. (Elsevier, 1990), Vol. 28, pp. 271–359.
3. V. I. Vlad and D. Malacara, "Direct spatial reconstruction of optical phase from phase-modulated images," in *Progress in Optics*, E. Wolf, ed. (Elsevier, 1994), Vol. 33, pp. 261–317.
4. G. W. Willard, "Focusing ultrasonic radiators," J. Acoust. Soc. Am. **21**, 360–375 (1949).
5. C. F. Ying, "Photoelastic visualization and theoretical analysis of scatterings of ultrasound pulses in solids," in *Physical Acoustics*, R. N. Thurston, ed. (Academic, 1990), Vol. 19, pp. 291–343.
6. M. Takeda, H. Ina, and S. Kobayashi, "Fourier-transform method of fringe-pattern analysis for computer-based topography and interferometry," J. Opt. Soc. Am. **72**, 156–160 (1982).
7. T. Ezure, K. Mizutani, and H. Masuyama, "Optical measurement of sound fields estimated from multiple interference images using Mach–Zehnder interferometer," Electron. Commun. Jpn. Part 2 **87**, 20–27 (2004).
8. O. J. Løkberg, "Sound in flight: measurement of sound fields by use of TV holography," Appl. Opt. **33**, 2574–2584 (1994).
9. R. C. Gutierrez, K. V. Schcheglov, and T. Tang, "Interferometric system for precision imaging of vibrating structures," U.S. patent 6,219,145, B1 (17 April 2001), http://www.freepatentsonline.com/6219145.pdf.
10. J. A. Conway, J. V. Osborn, and J. D. Fowler, "Stroboscopic imaging interferometer for MEMS performance measurement," in Aerospace Report TR-2007,8555, http://www.dtic.mil/cgi-bin/GetTRDoc?Location=U2&doc=GetTRDoc.pdf&AD=ADA470710.
11. J. S. Harris, R. L. Fusek, and J. S. Marcheski, "Stroboscopic interferometer," Appl. Opt. **18**, 2368–2371 (1979).
12. O. Y. Kwon, D. M. Shough, and R. A. Williams, "Stroboscopic phase-shifting interferometry," Opt. Lett. **12**, 855–857 (1987).
13. E. Abraham, K. Minoshima, and H. Matsumoto, "Femtosecond laser-induced breakdown in water: time-resolved shadow imaging and two-color interferometric imaging," Opt. Commun. **176**, 441–452 (2000).
14. K. T. Gahagan, D. S. Moore, D. J. Funk, J. H. Reho, and R. L. Rabie, "Ultrafast interferometric microscopy for laser-driven shock-wave characterization," J. Appl. Phys. **92**, 3679–2682 (2002).
15. V. V. Temnov, K. Sokolowski-Tinten, P. Zhou, and D. von der Linde, "Femtosecond time-resolved interferometric microscopy," Appl. Phys. A **78**, 483–489 (2004).
16. D. J. Funk, D. S. Moore, S. D. McGrane, J. H. Reho, and R. L. Rabie, "Ultrafast spatial interferometry: a tool for characterizing material phase and hydrodynamic motion in laser-excited metals," Appl. Phys. A **81**, 295–302 (2005).
17. M. Born and E. Wolf, *Principles of Optics*, 7th ed. (Cambridge U. Press, 1999), pp. 309–310.
18. The apparatus is, in fact, designed for working with low temperature samples protected by four windows on each side.
19. R. A. Fine and F. J. Millero, "Compressibility of water as a function of temperature and pressure," J. Chem. Phys. **59**, 5529–5536 (1973).
20. C. J. Morgan, "Least-squares estimation in phase-measurement inteferometry," Opt. Lett. **7**, 368–370 (1982).
21. J. J. Chyou, S. J. Chen, and Y. K. Chen, "Two-dimensionnal phase unwrapping with a multichannel least-mean-square algorithm," Appl. Opt. **43**, 5655–5661 (2004).
22. M. Deutsch and I. Beniaminy, "Inversion of Abel's integral equation for experimental data," J. Appl. Phys. **54**, 137–143 (1983).
23. J. Staudenraus and W. Eisenmenger, "Fiber-optic probe hydrophone for ultrasonic and shock-wave measurements in water," Ultrasonics **31**, 267–273 (1993).
24. J. E. Parsons, C. A. Cain, and J. B. Fowlkes, "Cost-effective assembly of a basic fiber-optic hydrophone for measurements

of high-amplitude therapeutic ultrasound fields," J. Acoust. Soc. Am. **119**, 1432–1440 (2006).
25. J. Schwider, R. Burow, K. E. Elssner, J. Grzanna, R. Spolaczyk, and K. Merkel, "Digital wave-front measuring interferometry: some systematic error sources," Appl. Opt. **22**, 3421–3432 (1983).
26. P. Hariharan, B. F. Oreb, and T. Eiju, "Digital phase-shifting interferometry: a simple error-compensating phase calculation algorithm," Appl. Opt. **26**, 2504–2506 (1987).
27. K. Davitt, A. Arvengas, and F. Caupin, "Water at the cavitation limit: density of the metastable liquid and size of the critical bubble," Europhys. Lett. **90**, 16002 (2010).
28. "Release on the refractive index of ordinary water substance as a function of wavelength, temperature and pressure," http://www.iapws.org/relguide/rindex.pdf.
29. K. Davitt, E. Rolley, F. Caupin, A. Arvengas, and S. Balibar, "Equation of state of water under negative pressure," J. Chem. Phys. (to be published).
30. The fact that the lasers used in both methods have different wavelengths (532 nm and 808 nm) introduces a negligible correction.

Review of Scientific Instruments 2014

Design, fabrication and characterization of a monolithic focusing piezoceramic transducer for an anisotropic material

Fabien Souris,[1] Jules Grucker,[2] Nabil Garroum,[1] Arnaud Leclercq,[2] Jean-Michel Isac,[2] Jacques Dupont-Roc,[2] and Philippe Jacquier[2]
[1]*Laboratoire de Physique Statistique, ENS, Univ. Pierre et Marie Curie and Univ. Denis Diderot, CNRS, Paris, France*
[2]*Laboratoire Kastler Brossel, ENS, Univ. Pierre et Marie Curie, CNRS, Paris, France*

(Received 21 November 2013; accepted 22 May 2014; published online 10 June 2014)

Piezoceramic transducers shaped as spherical caps are widely used to focus ultrasound waves in isotropic materials. For anisotropic materials, the sound wave surface is not spherical and the transducer surface should be adjusted to reproduce a portion of this wave surface to focus the emitted sound properly. In this article, we show how to design such a transducer and how to fabricate it in lab on a standard machine from a rod of raw piezo ceramic material. The main features of its electrical impedance response are well reproduced by a numerical model, allowing the identification of most of its vibrational modes. We finally measured the sound field emitted by such a transducer and found its focusing efficiency similar to that of spherical caps in isotropic media.
 [http://dx.doi.org/10.1063/1.4881535]

I. INTRODUCTION

Piezoceramic transducers find applications in many scientific domains: oceanography, medicine, material science, mechanical devices. Manufacturers[1] propose standard shapes such as disks, cylinders, rods, hemispheres, and spherical caps. These last two shapes are used in particular to focus ultrasound waves in isotropic media by driving thickness or radius oscillations of the cap. Sonoluminescence and lithotripsy are well-known applications of such devices.

Recently we met the problem of focusing an ultrasound wave in an anisotropic media, namely, hcp solid helium.[2,3] In this uniaxial solid, sound velocity varies from 530 m/s along the symmetry axis to 460 m/s in the perpendicular direction. Surprisingly, we did not find in the literature any work solving experimentally a similar problem. This article describes the solution we adopted for the design and the fabrication of an appropriate transducer, and the results obtained. Although the problem we had to solve may appear very specific, we feel that application of similar solutions to more common anisotropic materials such as layered materials may be of wider interest.[4]

The article is organized as follows.

In Sec. I, the design of the transducer is discussed. A segmented phased array transducer is a possible design for a focusing device. However, it requires many electrical connections and each element of the array needs to be driven independently. Instead, we opted for a monolithic shaped transducer. Its simplicity gives it intrinsic stability and it is more appropriate to generate high amplitude waves. The emitting inner surface of the transducer must then reproduce a portion of the material sound wave surface. It is perhaps less obvious that the transducer thickness should not be constant all over the surface, but should be corrected for the local surface curvature in order the oscillation to have the same phase everywhere.

In Sec. II, the fabrication of the transducer is described in details. Although some manufacturers are able to provide custom shaped piezoceramic transducers, generally for a large number of items, we choose to machine our transducer from bulk ceramic material using a general purpose computer numerical control (CNC) machine of the laboratory workshop by replacing cutting tools by rotating grinding dies. We found it a fast, cheap, and flexible procedure.

In Sec. III, geometrical and electrical characterizations of the transducer are reported. Oscillation mode spectrum is measured. Because of the existence of edges, the main oscillation modes are not simple piston like motions of the transducer surface. For a more precise characterization, a numerical modeling of the transducer has been set up, providing both the mode spectrum to be compared to the experimental one and the mode oscillation amplitude maps.

Finally, an example of a focused sound pulse in solid helium is shown. It is compared with a numerical model assuming a geometrically perfect transducer oscillating with a piston like motion.

II. DESIGN OF THE TRANSDUCER

The transducer has a cylindrical symmetry around the z-axis. Its inner surface matches half the wave surface of the quasi-longitudinal pressure wave in solid helium. According to Crepeau and Lee,[5] it is given by the parametric equations in cylindrical coordinates

$$\frac{z}{R} = \frac{u}{2V\sqrt{\ }}[(2-2\alpha+\beta)\sqrt{\ } - (2\gamma^2-\alpha\beta-\beta^2)u^2 + (2\gamma^2-\alpha\beta)], \quad (1)$$

$$\frac{r}{R} = \frac{\sqrt{1-u^2}}{2V\sqrt{\ }}[(2-\alpha)\sqrt{\ }+\alpha^2+(2\gamma^2-\alpha\beta-\alpha^2)u^2],$$

where $0 \leq u \leq 1$ and

$$\sqrt{} = \sqrt{\alpha^2 + 2(2\gamma^2 - \alpha(\alpha+\beta))u^2 + ((\alpha+\beta)^2 - 4\gamma^2)u^4},$$

$$V^2 = \frac{1}{2}[2 - \alpha + (\beta - \alpha)u^2 + \sqrt{}].$$

The size parameter R, which represents the equatorial radius of the inner surface, is chosen as $R = 6$ mm, so that the transducer can fit the available room in the experimental cell. The numerical parameters α, β, and γ are related to the elastic moduli c_{ij} and are found to be

$$\begin{aligned} \alpha &= (c_{11} - c_{44})/c_{11} = 0.693, \\ \beta &= (c_{33} - c_{44})/c_{11} = 1.060, \\ \gamma &= (c_{13} + c_{44})/c_{11} = 0.567. \end{aligned} \tag{2}$$

In a first approximation, the outer surface is parallel to the inner one at a distance $e = 2$ mm, so that the fundamental thickness vibration mode of the emitter has a frequency around

$$f_0 = s/2e \simeq 1.15 \text{ MHz}. \tag{3}$$

Ceramics sound velocity is $s \simeq 4600$ m/s. However, thickness vibration mode frequencies of thick shells depend on their curvature. For instance, the frequency of the first thickness mode for a spherical cap is larger than that of a cylinder with the same thickness e and radius R, which is itself larger than those of disks with thickness e. More precisely, let us assume that the ceramic material has isotropic elastic properties, described by Lamé coefficients λ and μ, and a longitudinal sound velocity s. For an infinite plate with thickness e, the frequency of the first thickness oscillation mode is f_0 given by Eq. (3). To the lowest order in the parameter e/R, the frequencies f_s and f_c of the same mode for the sphere and the cylinder of radius R are given, respectively, by[6]

$$f_s = f_0[1 + 2(1 - \eta)(e/\pi R)^2], \tag{4}$$

$$f_c = f_0\left[1 + \left(\tfrac{7}{8} - \eta\right)(e/\pi R)^2\right], \tag{5}$$

with $\eta = \lambda/(\lambda + 2\mu)$. Hence it would be of interest to generalize these expressions for the resonance frequency f_q of a sheet with an arbitrary shape. While the expression of f_q can be derived from elastic wave equations (see a sketch of the derivation in the Appendix), it is possible to generalize the expressions (4) and (5) in a heuristic way. We consider here only the correction to f_0 to lowest order in $e/\pi R_1$ and $e/\pi R_2$, where R_1 and R_2 are the principal curvature radii of the inner surface. First, the expression cannot contain linear terms in $e/\pi R_{1,2}$ because this would make the frequency f_q to depend on the arbitrary orientation of the surface. Hence f_q is a linear function of $(e/\pi R_1)^2$, $(e/\pi R_2)^2$, and $e^2/\pi^2 R_1 R_2$. A first guess is to add two terms similar to those of formulae (5) using R_1 and R_2, respectively. Then to match formula (4) for $R_1 = R_2 = R$, one has just to add a term $e^2/4\pi^2 R_1 R_2$. Hence finally, one gets

$$f_q = f_0\left[1 + \left(\tfrac{7}{8} - \eta\right)\left(\frac{e^2}{\pi^2 R_1^2} + \frac{e^2}{\pi^2 R_2^2}\right) + \frac{e^2}{4\pi^2 R_1 R_2}\right]. \tag{6}$$

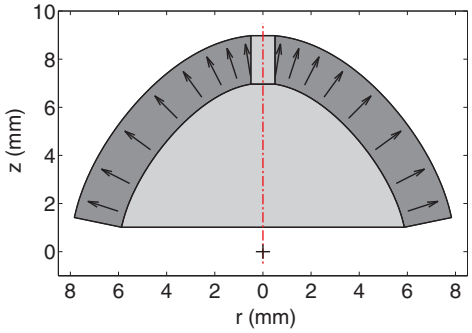

FIG. 1. Shape of the transducer profile shown as a radial cut. The inner surface of the transducer matches the wave surface of a hcp helium crystal. The local polarization axis is represented by the black arrows.

For the emitter shape discussed here, R_1 and R_2 increase from the top to the rim. To make f_q constant all over the surface, one varies the local thickness to compensate for the curvature effect on the frequency. Quantitatively this correction appears to be small, on the order of 3% of the thickness. This is on the same order of magnitude as the machining error. Hence a constant thickness is also an acceptable approximation in our particular case.

The final design is shown in Fig. 1. The sound wave emitted by the oscillating inner surface is focused at the coordinate origin. In our experiment, the origin should be in direct view without being screened by the emitter rim. The lower 1 mm of the half wave surface was then cut away, and in addition a hole, 1 mm in diameter, was introduced at the top of the emitter. The electrical excitation applied to the transducer should be coupled to the thickness vibration mode. To that aim, the polarization axis of the piezo ceramic is defined along its thickness and the voltage will be applied between the inner and the outer surface of the transducer. What precision is required for the fabrication of the transducer? We requested that the inner emitting surface should not differ from the expected one by more than about 10% of the sound wavelength in solid helium at frequency f_0, which is 0.4 mm in the radial direction. This means a 40 μm precision.

III. FABRICATION OF THE TRANSDUCER

In order to allow driving at high power, lead zirconate titanate ceramic (Navy I type)[7] was chosen for the transducer material. We started from cylinders 20 mm in diameter and 20 mm in length. To machine ceramics, specialized CNC grinding machines do exist, but are not often found in physics labs. Hence, a standard CNC lathe was used with the cutting tools replaced by a grinding spindle, equipped with diamond tools.[8] As a matter of fact, we simply used an existing pneumatic hand tool die grinder. Its speed is tunable from 3000 to 17 000 rpm by changing air pressure from 0.25 to 4 bar. The initial pieces were hold in the lathe main chuck rotating at 100 rpm. The tools used, their characteristics and their respective rotation speeds are listed in Table I. An important water lubrification was always provided.

The machining of the emitter was decomposed in five successive stages, all represented on Fig. 2. First, the

TABLE I. The grinding tools used. Machining steps are explained in Fig. 2.

Number	Tool type	Diameter (mm)	Length (mm)	Speed (rpm)	Step
1	Disintegrating core drill	6.5	25	8000	1, 2
2	Drill with half-spherical head	5	25	8000	3
3	Drill	1	25	10 000	3
4	Shank	63.5	6.4	4000	4, 5

diameter of the rod was partially reduced using tool 1. The same tool was used on step 2 for a rough machining of the inner surface of the emitter. On step 3, the inner surface was finished using tool 2, and the top hole was drilled with the tool 3. The tip radius of tool 2 (see Table I) was specifically chosen to be less than the minimum surface radius, which was found to be 3.2 mm at the top. The outer surface was partially machined during step 4, with tool 4. On the last step, for cutting the remaining tail and finishing the outer surface, the piece was hold with a previously prepared cage, tighten with a fine thread. For those two operations, tool 4 was used and its initial position was carefully adjusted on the previously grounded surface. Surface finishing quality was good enough requiring no additional polishing.

Finally, the inner and the outer surfaces had to be silvered to create the electrodes, and the piezo ceramic polarized by applying a high voltage between the electrodes above the material Curie temperature (330 °C). Although these operations could be performed in the lab, it was found easier to have them done by the piezo ceramic manufacturer.

IV. CHARACTERIZATION OF THE TRANSDUCER

For convenience, various tests were performed in air at room temperature although at the end the transducer is used at 1 K in solid helium. Some parameters undergo changes which will be indicated.

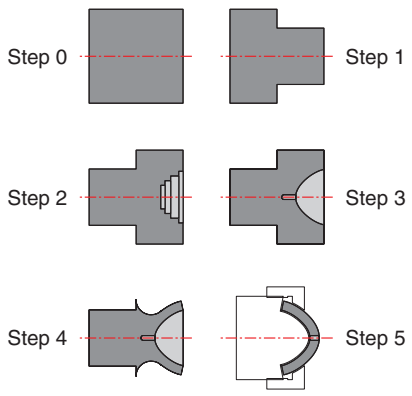

FIG. 2. Initial shape of the ceramic piece (step 0) and successive machining steps (1-5). For step 5, the piece is hold in a previously prepared metal holder. The holding lathe chuck is on the left side, but not shown.

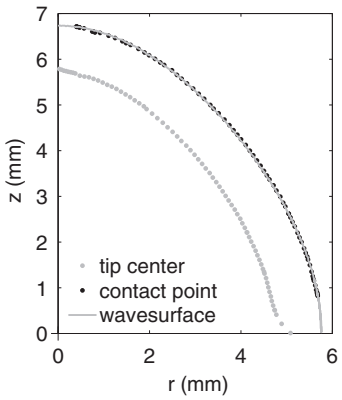

FIG. 3. Experimental profile measured using a dial test indicator compared with the designed one. The gray dots represent the trajectory of the ball tip center (ball radius 1 mm). The contact points with the inner surface deduced from them are represented by the black dots. The gray line is the fitted theoretical wave surface with $R = 5.83$ mm.

A. Inner surface checking

The inner surface quality is checked by using a dial test indicator mounted on a dual axis translation stage. The spherical tip (diameter $d = 2$ mm) of the dial test indicator is displaced along the surface by step of $\sim$100 μm in the radial plane. The coordinates (x_c, y_c) of the tip center C during this displacement, as well as the position of the symmetry axis, are measured using the micrometric screws of the translation stage while the dial test indication is kept constant within 10 μm. From the tip trajectory (Fig. 3), the coordinates (x_s, y_s) of the point S of the inner surface of the transducer are retrieved using the formula $\mathbf{OS} = \mathbf{OC} + \mathbf{n}\,d/2$, where $\mathbf{n}$ is the normal unit vector to the tip trajectory at point C, and O the coordinate origin. The result is presented on Fig. 3.

In order to appreciate the accuracy of the machined inner surface, a fit of the measured inner surface (x_s, y_s) is made with the theoretical wave surface given in Eq. (2). We used two degrees of freedom, the size parameter R, and a vertical offset. The experimental size parameter is found to be $R = 5.83$ mm, which deviates by 2.8% from the aimed $R = 6.0$ mm value. The theoretical wave surface for $R = 5.83$ mm is represented on Fig. 3 by the gray line. The disagreement between the two profiles as a function of the polar angle is at most 50 μm. This is slightly larger than the 40 μm expected precision, but nevertheless acceptable. Thus the machining technique described in Sec. II proved to satisfactorily meet the desired precision.

B. Electrical impedance spectrum

The electrical impedance spectrum depends on the dielectric part and on the piezoelectric part associated with the various mechanical vibration modes of the transducer. Each resonance mode gives rise to a resonance with an impedance minimum and an antiresonance with an impedance maximum. Then, measuring the electrical impedance $Z(f)$ as function of the frequency f is a direct way to find the frequencies of these oscillation modes. The measurement of $Z(f)$ is achieved

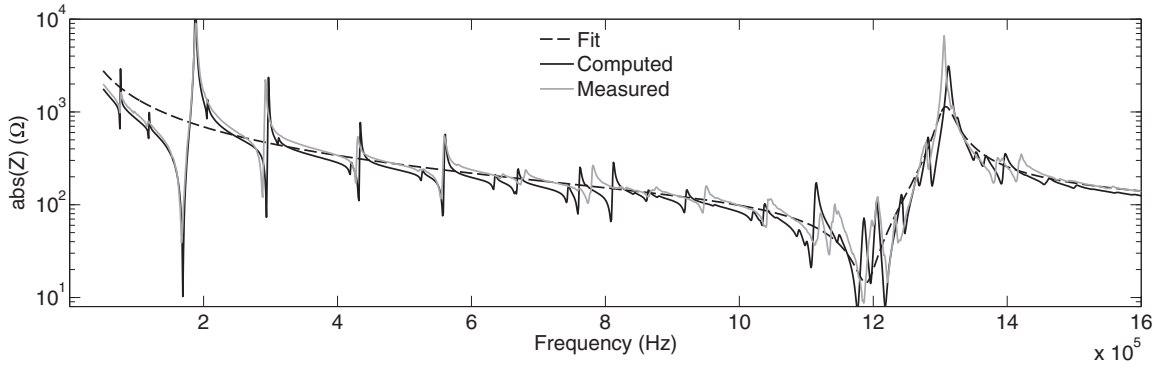

FIG. 4. Transducer impedance around the thickness resonance frequency found around 1.2 MHz. The light gray line is the measured impedance. The computed curve is extracted from the numerical model described in Sec. IV B. The dashed line is a fit of the thickness resonance by a resonant circuit model.

by feeding the transducer through a large resistor R from a voltage source $V_0(f)$ and monitoring the voltage $V(f)$ across the transducer. $V_0(f)$ and $V(f)$ are complex amplitudes derived from the sinusoidal signals measured on a digital oscilloscope. Then $Z(f) = R\,V(f)/[V_0(f) - V(f)]$. In Figure 4, $|Z|$ is shown in the frequency range $0.05 - 1.6$ MHz.

Although many resonances are visible, one resonance dominates the measured spectrum. This resonance can be modeled with an equivalent circuit composed from a pure capacitance C_0 in parallel with a series RLC circuit, representing the mechanical oscillation mode of the transducer. The impedance of this equivalent circuit is adjusted to the measured impedance by varying the four free parameters of the equivalent circuit. The result is shown in Figure 4, and the set of parameters obtained are summarized in Table II. The resonance frequency f_r of this vibration mode is found to be 1.19 MHz, close to the 1.15 MHz expected for the thickness vibration mode (*cf.* II), with an antiresonance frequency $f_a = 1.31$ MHz. The effective electromechanical coupling factor defined as $k_{eff}^2 = 1 - (f_r/f_a)^2$ is around 0.4. This strong coupling indicates that the piezoelectric transducer has been machined and polarized correctly, and that the electrical excitation is effectively coupled to the thickness vibration mode.

However, numerous additional resonances appear, corresponding to standing Lamb waves generated at the lower rim and extending to the cap. These Lamb waves are mixed with the piston like motion assumed for the thickness vibrational mode. This was mentioned by Cathignol[9] for concave spherical caps, and investigated extensively in piezoelectric disks using finite element modeling[10,11] and impedance spectra[12] analysis. For disks, the piston-like motion is found to be a good approximation for diameter to thickness ratio D/T greater than 20. Assuming that our transducer is simply a curved disk, its D/T ratio is around 10. Hence ripples from the Lamb waves are expected to modify the thickness resonance mode. Given the transducer complex geometry, a numerical modeling of the resonance modes was undertaken.

TABLE II. Set of parameters obtained by adjusting the resonant circuit model impedance to the measured impedance. f_r and f_a are the resonance and antiresonance frequencies. The quality factor of the resonance and the coupling factor are, respectively, defined as $Q = 2\pi f_r L/R$ and $k_{eff}^2 = 1 - (f_r/f_a)^2$.

C_0 (pF)	R (Ω)	L (μH)	C (pF)	f_r (MHz)	f_a (MHz)	Q	k_{eff}
950	14.6	91.2	196	1.19	1.31	44.3	0.414

C. Numerical modeling

A finite element model of the transducer is created using COMSOL[13] software. Due to the axial symmetry, the problem can be reduced to a 2D model. The geometry of the transducer is defined using two parametric curves for the inner and outer surface, according to the design defined in Sec. II. The physical properties of the piezo ceramic material are extracted from technical datasheets.[14] The main properties are the compliance matrix at constant electric field $\mathbf{s_E}$, the coupling matrix $\mathbf{d}$, the relative permittivity $\boldsymbol{\epsilon}$, and the density ρ. To create the polarization system along the thickness of the transducer (see Fig. 1), we use the result obtained from a preliminar static study. The polarization system is oriented along the electrical field inside the ceramic, when a constant voltage is applied between the inner and outer electrodes.

The electrical impedance spectrum $Z_s(f)$ of the model is computed for the frequency range $0.05 - 1.6$ MHz. The impedance is calculated by integrating the current density J over the electrode surface, and dividing it by the voltage U applied to the transducer. This simulated response is compared to the experimental impedance spectrum $Z_m(f)$, shown in Fig. 4. In order to fit Z_s to Z_m, some parameters of the model are adjusted in the following way. The internal radius is set to be the measured internal radius (see Sec. IV A). The coefficients of the coupling matrix $\mathbf{d}$ determine the spacing Δf between the resonance and the anti-resonance frequencies. The adjustment is made by scaling the coupling matrix $\mathbf{d}$, to match the values of the simulated and the experimental values of Δf. The thickness of the transducer e is modified to adjust the resonance frequency of the main thickness vibration mode[12] found around 1.2 MHz. Finally, the angular aperture of the emitter is corrected to adjust the resonance frequencies of the

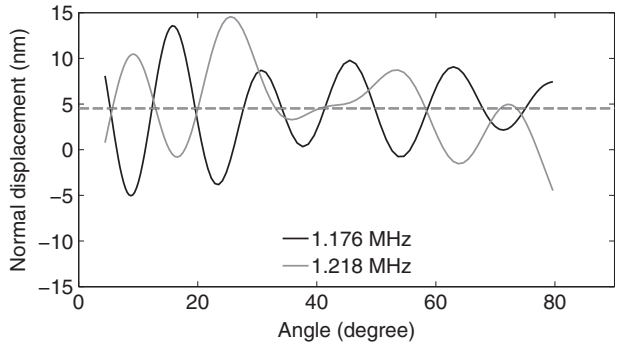

FIG. 5. Normal displacement found in the numerical simulation for the inner surface for a 1 V electrical excitation represented along the aperture angle for two vibration modes: 1.176 MHz (black) and 1.218 MHz (gray). The mean displacements obtained by averaging the true displacements over the emitter surface are the same for the two modes and are represented by the dashed line.

first vibration modes, in particular the radial vibration mode[11] at 0.16 MHz.

D. Numerical results

The result of this numerical modeling is shown in Figure 4. Up to 0.6 MHz the agreement with the measured impedance is satisfactory since many features of the spectrum are correctly reproduced. Above that frequency some discrepancies can be found and the small resonances are sometimes shifted.

However, the overall shape of the dominant thickness vibration mode is very well reproduced by the numerical model, and the simulated spectrum also shows the existence of two impedance minima, located around 1.2 MHz, more precisely 1.176 MHz and 1.218 MHz. As mentioned before, those two minima originate from the mixing of the thickness mode with the surface waves. In order to understand the differences between those two modes, we investigate the displacement profile of the inner surface for each of them. Figure 5 represents the normal displacement of the inner surface as a function of the aperture angle, when the mean value of the displacement is maximum. For both vibration modes, the surface is distorted by large amplitude ripples with a complicated pattern. However, in both case those ripples are superimposed with nonzero mean displacement, as expected for the thickness vibrational mode. For a 1 V electrical excitation, the amplitude of this mean displacement is found to be 4.5 nm for both 1.176 MHz and 1.218 MHz modes.

E. Changes at low temperature

When the transducer is cooled down to 1 K, the frequency of the thickness mode increases by about 5%. This results from an increase of the frequency constant of the ceramic material. The Q-factor of the resonance decreases by about a factor 2. More precisely, the impedance at resonance is found to be 26 Ω instead of 10 Ω. In the same temperature range, according to the manufacturer,[14] the ceramic quality factor decreases also by a factor 2. A further decrease of the Q-factor should be associated with the sound emission in solid helium instead of air. However, the acoustic impedance ratio between the ceramic material and solid helium is about 400. Hence the radiative damping of the transducer is negligible compared to the dissipation in the material.

V. EXPERIMENTAL FOCUSING EFFICIENCY

Eventually, the transducer efficiency was demonstrated by focusing strong ultrasound pulses in solid helium. Using an interferometric imaging technique, we imaged the propagation of density waves through the acoustic focus.[15] As a matter of fact, the method gives refractive index modulation maps δn_{exp}, proportional to the relative density modulation $\delta\rho/\rho = \delta n/(n-1) = \delta n/0.037$ for solid helium on the melting line at 1 K. The theoretical propagation of the ultrasound pulses in solid helium is calculated with a finite difference simulation.[3] It gives simulated maps of the refractive index variation δn_{sim}. The sound pulse is produced by exciting the transducer at resonance with a 4 period pulse. The sound amplitude grows during the first 4 oscillations and then decays with the transducer damping time given by the quality factor. Only the piston like motion is electrically excited and 4 periods are not long enough to give time to the Lamb waves to grow. Thus, in the simulation, the source is set to have the same amplitude behavior with a piston like motion.

In Figure 6, a comparison of those refractive index maps is shown along with radial profiles. More precisely, the maximum wave amplitude recorded during the sound pulse travel is mapped at each point and normalized by the peak value at focus. The similarity between experimental and simulated profiles is striking and illustrates clearly the focusing efficiency. The intense peak at the focal point is easily distinguishable from other secondary maxima. The focus radius, defined as the distance of the first minimum, is about a wavelength λ_s along the transducer axis and $\lambda_s/2$ in the radial direction. This is similar to what is known for focused wave produced by hemispherical transducer in isotropic media[16] for which the radii are, respectively, λ_s and $0.61\lambda_s$. The contrast in the amplitude modulation is somewhat smaller for the experimental result. Typical differences are however less than 10% of the maximum amplitude. These differences may originate from nonlinear effects in the wave propagation (pressure amplitudes are typically several bar), not taken into account in the simulation. It could also come from the finite spatial resolution of the optical method used (30 μm). From the simulation, the focusing efficiency, given as the ratio of the sound amplitude at the focus to that at the transducer surface, is found to be 86. For a spherical cap of similar aperture $\Theta \simeq 80^\circ$ in an isotropic media, the focusing efficiency would be $2\pi(1-\cos\Theta)R/\lambda_s \simeq 85$ taking for λ_s the value in the radial direction $\lambda_s = 0.37$ mm.

The main conclusion is that the fabricated transducer is able to focus an intense sound wave in the studied anisotropic crystal with an efficiency very similar to a spherical cap in an isotropic media.

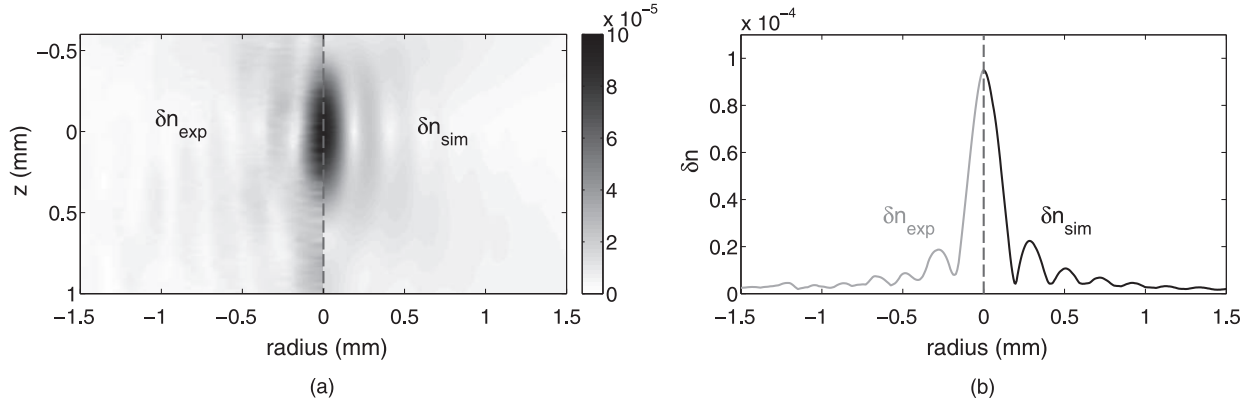

FIG. 6. Comparison of local maximum sound amplitudes measured by the refractive index modulation δn. For each figure, the left panel is the experimental result, and the right panel is a numerical result from a simulation adjusted to give the same maximum at the focus. The similarity is striking, although the contrast in the amplitude modulation is somewhat smaller for the experimental result. Typical differences are less than 10% of the maximum amplitude.

VI. CONCLUSION

We have shown that focusing piezoceramic transducers can be adapted to anisotropic elastic materials to produce focused sound waves. The inner transducer surface follows the shape of the sound wave surface. Its thickness can be corrected for the local surface curvature. Because of the mixing between the thickness modes and the Lamb surface resonances, it is preferable to choose large diameter to thickness ratio in order to achieve wave amplitudes constant over the entire emitting surface. However, the fact that the sound wave is not exactly longitudinal cannot be taken into account, and a weak parasitic shear wave is also emitted. Although the wave surface is not as simple as a spherical cap, we have shown that machining with CNC machines found in most labs is possible with the desired precision. While the application shown pertains to low temperature physics, application to other anisotropic materials such as layered material may be of interest. In that case, the material will have to be shaped to match the inner volume of the transducer, and the interval between the transducer and the material filled with an appropriate liquid to transmit efficiently the sound vibration.

APPENDIX: OSCILLATION FREQUENCY OF CURVED THICK SHELLS

We consider a shell of thickness e, limited by two parallel curved surfaces. A point on the inner surface S_i is described by orthogonal curvilinear coordinates ξ_1 and ξ_2, and local unit vectors $\mathbf{a}_1(\xi_1, \xi_2)$ and $\mathbf{a}_2(\xi_1, \xi_2)$. The third coordinate for a point M in the material bulk is the height h from S_i along the normal vector $\mathbf{a}_3 = \mathbf{a}_1 \times \mathbf{a}_2$.

The elastic wave equation for the isotropic material is[17]

$$\rho \ddot{\mathbf{u}} = (\lambda + 2\mu)\nabla(\nabla \cdot \mathbf{u}) - \mu \nabla \times (\nabla \times \mathbf{u}) \tag{A1}$$

with the border conditions that the stress tensor flux across both inner and outer surfaces are zero

$$0 = \sigma^{3j}, \ j = 1, 2, 3 \ \text{for } h = 0 \text{ and } h = e. \tag{A2}$$

Let U, V, and W be the components of $\mathbf{u}$ on the $\mathbf{a}_1$, $\mathbf{a}_2$, $\mathbf{a}_3$ local axis. We use the expressions of Ref. 17 for the normalization factors h_1, h_2, h_3, the contravariant component expressions, and the differential operators. We consider harmonic oscillations at frequency f_q having components only along $\mathbf{a}_3 : U = V = 0$. The derivatives $\partial W/\partial \xi_1$ and $\partial W/\partial \xi_2$ are neglected in comparison to $\partial W/\partial h = W'$. With those approximations, one finds that $(\nabla \times \mathbf{u}) = 0$ and

$$\begin{aligned} \nabla \cdot \mathbf{u} &= \frac{1}{h_1 h_2 h_3} \frac{\partial}{\partial \xi_3}(h_1 h_2 W) \\ &= W' + \left(\frac{1}{h_1} \frac{\partial h_1}{\partial \xi_3} + \frac{1}{h_2} \frac{\partial h_2}{\partial \xi_3} \right) W. \end{aligned} \tag{A3}$$

The coefficient of W is the total curvature of the surface $h =$ constant. It can be written in terms of the principal curvatures $C_1(\xi_1, \xi_2, h)$ and $C_2(\xi_1, \xi_2, h)$ as $C_1 + C_2$. If R_1 and R_2 are the principal curvature radii of the inner surface ($h = 0$) at point ξ_1, ξ_2, the curvatures can be written as $C_1 = 1/(R_1 + h)$ and $C_2 = 1/(R_2 + h)$. Then Eqs. (A1) and (A2) reduce to

$$0 = W'' + (C_1 + C_2)W' + (k^2 - C_1^2 - C_2^2)W, \tag{A4}$$

$$0 = W' + \eta(C_1 + C_2)W \ \text{for } h = 0 \text{ and } h = e, \tag{A5}$$

with $k = 2\pi f_q/s$. The solution of (A4) is known only for $R_1 = R_2$ (sphere), and for R_1 or $R_2 = \infty$ (cylinder). In the general case, only an approximate solution can be found, for instance, to second order in $1/kR_1$ and $1/kR_2$. The coefficients of W' and W are developed to that order. Taking $x = kh$ as the dimensionless variable, the approximate equation for $W(h) = w(x)$ reads

$$w'' + (c - d\,x)w' + (1 - d)w = 0, \tag{A6}$$

where $c = 1/kR_1 + 1/kR_2$ and $d = 1/(kR_1)^2 + 1/(kR_2)^2$ are, respectively, first order and second order constants. Border condition (A5) becomes

$$w' + \eta(c - d\,x)w = 0 \ \text{for } x = 0 \text{ and } ke. \tag{A7}$$

Solution of Eq. (A6) is searched for as

$$W(h) = w(x) = (a_0 + a_1 x + a_2 x^2)\exp(ix) + \text{c.c.}, \tag{A8}$$

where a_1/a_0 and a_2/a_1 are at least first order in curvature. It is easily found that

$$a_1 = -(a_0/8)[4c + i(c^2 + 2d) + \cdots], \tag{A9}$$

$$a_2 = (a_0/8)[c^2 + 2d + \cdots]. \tag{A10}$$

Then the border conditions (A7) are applied to find a_0/a_0^* and ke. Eliminating a_0/a_0^* between the two equations gives the eigenfrequency equation for the thickness modes. Keeping only second order term in c, it reads

$$\exp(2ike) = 1 + 2ike\left[\left(\tfrac{3}{4} - \eta\right)d + c^2/8\right]. \tag{A11}$$

One looks for solutions that are approximately antisymmetric with respect to $x = ke/2$. The first one corresponds to $ke = \pi$, at zeroth order in c. At second order, ke becomes $ke = \pi[1 + (\frac{3}{4} - \eta)d + c^2/8]$. This gives formula (6) for the mode frequency.

[1] See for instance Channel Industries, SensorTech, Morgan Electroceramics, Ferroperm Piezoceramics.

[2] F. Souris, J. Grucker, J. Dupont-Roc, and Ph. Jacquier, EPL **95**, 66001 (2011).

[3] F. Souris, A. Qu, J. Grucker, J. Dupont-Roc, and Ph. Jacquier, "On the destabilization of metastable solid 4He," J. Low Temp. Phys. (published online).

[4] See for instance : C. Boller, S. Pudikov, and A. Bulavinov, AIP Conf. Proc. **1430**, 881 (2012).

[5] R. Crepeau and D. Lee, Phys. Rev. A **6**, 516 (1972).

[6] C. Chree, Trans. Cambridge Philos. Soc. **14**, 250 (1887), see formula 65 (p. 321) in the limit $(a - a')/a \ll 1$ and $k\alpha(a - a') \simeq \pi$ for a spherical shell. For the cylinder, formula 42 (p. 356) is used, taking an asymptotic form for the Bessel functions and the same approximations than for the sphere, http://www.archive.org/details/transactions14camb/.

[7] PZT401 from Morgan Electroceramics, http://www.morganelectroceramics.com

[8] From Chicago diamond Tools, http://www.cdtusa.net.

[9] D. Cathignol, O. A. Sapozhnikov, and J. Zhang, "Lamb waves in piezoelectric focused radiator as a reason for discrepancy between O'Neil's formula and experiment," J. Acoust. Soc. Am. **101**(3), 1286 (1997).

[10] J. Kocbach, "Finite element modeling of ultrasonic piezoelectric transducers," Ph.D. thesis (University of Bergen, 2000).

[11] N. Guo, P. Cawley, and D. Hitchings, "The finite element analysis of the vibration characteristics of piezoelectric discs," J. Sound Vibration **159**(1), 115–138 (1992).

[12] S. Ikegami, I. Ueda, and S. Kobayashi, J. Acoust. Soc. Am. **55**, 339 (1974).

[13] COMSOL software, Licence number 8072866.

[14] The s_{13}^E coefficient must be set negative instead of positive, http://www.morganelectroceramics.com/resources/datasheets-msds/.

[15] F. Souris, J. Grucker, J. Dupont-Roc, Ph. Jacquier, A. Arvengas, and F. Caupin, Appl. Opt. **49**, 6127 (2010).

[16] H. T. O'Neil, J. Acoust. Soc. Am. **21**, 516 (1949).

[17] P. Morse and H. Feshbach, *Methods of Theoretical Physics* (McGraw Hill, New York, 1953), Vol. I.

Jules Grucker **November 30, 2018**

Sujet : L'hélium-4 liquide et solide en phase métastable

Résumé : Ce manuscrit décrit mes travaux de recherche effectués depuis 2009 au sein l'équipe "Solide et Fluide Quantiques" du Laboratoire Kastler Brossel. J'y décris les expériences que nous avons menées concernant la production et la caractérisation d'états métastables de l'hélium-4 liquide et solide. Ces états sont produits en focalisant une onde acoustique (pression/densité) dans la masse de l'échantillon.

Nous avons pu mesurer la densité à laquelle l'hélium-4 liquide cavite à une température de ~ 1 K. Cette mesure de densité de cavitation n'est pas compatible avec des mesures de la pression de cavitation lorsque les deux quantités sont liées par une équation d'état théorique du liquide métastable. Nous avons aussi étudié en fonction de la température le temps de vie des bulles de cavitation que nous produisons. Nous trouvons que celui-ci subit une transition spectaculaire au point λ que nous expliquons par les différences radicales des propriétés de conduction de la chaleur dans le liquide superfluide et dans le liquide normal.

En ce qui concerne l'hélium-4 solide métastable, nous avons été le premier groupe à en produire et en observer. En essayant d'augmenter son degré de métastabilité, nous avons rencontré une instabilité inattendue. Cette instabilité est bien déclenchée lorsque le solide explore sa phase métastable et est liée aux variations du volume molaire induites par l'onde acoustique et non aux contraintes de cisaillement.

Pour mieux comprendre les déstabilisations observées de l'hélium-4 liquide et solide en phases métastables, je propose de mesurer leurs équations d'état. Cela peut être fait en mettant en place une expérience de diffusion Brillouin stimulée.

Mots clés : ^{4}He liquide et solide, États métastables, Instabilités, Temps de vie des bulles de cavitation, Équations d'état

Subject : Metastable Solid and Liquid Helium-4

Abstract:

This manuscript describes my research carried out since 2009 within the team "Quantum solids and fluids" of Laboratoire Kastler Brossel. I describe the experiments we have conducted on the production and characterization of metastable

states of liquid and solid helium-4. These states are produced by focusing an acoustic wave (pressure / density) in the bulk of the sample.

We have been able to measure the density at which liquid helium-4 cavitates at a temperature of $\sim$ 1 K. This cavitation density measurement is not compatible with cavitation pressure measurements when the two quantities are linked by a theoretical equation of state of the metastable liquid. We also studied as a function of temperature the lifetime of the cavitation bubbles that we produce. We find that it undergoes a spectacular transition at the λ point which we explain by the radically different heat conduction properties between the superfluid liquid and in the normal liquid.

For metastable solid helium-4, we were the first group to produce and observe it. In trying to increase its degree of metastability, we encountered an unexpected instability. We have demonstrated that this instability is triggered when the solid explores its metastable phase and is related to the variations of the molar volume induced by the acoustic wave and not to the shear constraints.

To better understand the observed destabilizations of liquid and solid helium-4 in metastable phases, I propose to measure their equations of state. This can be done by setting up a Stimulated Brillouin Scattering experiment.

Keywords : Liquid and solid ^{4}He, metastable states, Instabilities, Cavitation bubble lifetime, Equations of State